Università di Cagliari
Facoltà di Biologia e Farmacia
Dipartimento di Scienze Biomediche
Sezione di Microbiologia e Virologia

Dottorato di ricerca in
"Sviluppo e Spermentazione dei Farmaci Antivirali"
XXVI Ciclo

Titolo Tesi

Innovative approaches for rapid *antemortem* diagnosis of prion disorders and to predict synergistic effects of drug combinations

Settore scientifico-disciplinare
BIO/19 – Microbiologia generale

Coordinatore Dottorato
Prof.ssa Alessandra Pani

Relatore (Cagliari)
Prof.ssa Alessandra Pani

Relatore (estero)
Dott. Byron Caughey

Candidato
Dott. Matteo Manca

Anno Accademico
2012-2013

Foreword

The following thesis is divided into chapters One and Two. Chapter One and first part of chapter Two will focus on research activities conducted at the University of Cagliari during the first eighteen months of my Ph.D. program. This research led to three published articles and another one in progress that will soon be submitted for peer review (data not discussed). From the end of May 2012 until November 2013 I was involved in a graduate partnership program as supplemental visiting fellow at the Rocky Mountains Laboratories, a National Institutes of Health (NIH) facility located in Hamilton (Montana, USA); research conducted during this experience led to the article discussed in second part of chapter Two.

Table of contents

Chapter 1
Development of a novel approach to predict and quantify the synergism of anti-cancer drugs using experimental design and artificial neural networks

Introduction and rationale

The treatment of cancer is mostly based on a multidrug strategy. The administration of more than one drug at the same time aims to avoid the increase of drug resistant cells and reduce the dose of each drug of the combination, exploiting the synergistic effect. At the moment the evaluation of the synergistic effect is mainly performed using the Combination Index (CI) method and also Isobolograms (IB). The CI method is based on the assumption that the effect of the drugs is due only to the inhibition of enzyme kinetics (Chou et al. 1981). This assumption is not valid for any kind of drug in use; it is well known and studied that also other mechanisms can be involved. Cisplatin (CDDP) is one example of anticancer drug that has a different mechanism of action than direct effect on enzymes. Moreover, both CI and IB methods can only establish the effectiveness of the drug combination experimentally tested. We tried to overcome the limits of the classical approach using the Experimental Design (ED) and Artificial Neural Networks (ANNs); this approach, in fact, could not only allow to better quantify the degree of drug synergism of the tested combinations, but also to predict the effect of all possible drug doses, leading to the identification of the combination with the most powerful synergistic effect.

An ANN is a powerful mathematical tool in the form of a computer software that recreates the structure and the functions of a biological brain. It is composed by logic units called "neurons" organized in 3 layers: input, hidden and output. After an appropriate "learning" process the ANN is able to predict the response for values of inputs never used before. The learning process is performed with a limited number of experiments that produce input data for the network called "training set".

A previous study (published by *Journal of Inorganic Biochemistry*) allowed us to evaluate anti-cancer activity of new copper(II)-phenantroline complexes (Pivetta et al. 2011) versus human hematologic (CCRF-CEM and CCRF-SB) and solid tumor-derived cell lines (K-MES-1 and DU-145); afterwards, ANN method was applied to binary mixtures of these new copper(II) complexes with CDDP tested against CCRF-CEM.

The latter study was performed thanks to the joined efforts with a group of chemists of the University of Cagliari and from the Masaryk University (Brno, Czech Republic). The results obtained confirmed our hypothesis and were recently published by *Talanta* (see following articles).

Journal of Inorganic Biochemistry 114 (2012) 28–37

Contents lists available at SciVerse ScienceDirect

Journal of Inorganic Biochemistry

journal homepage: www.elsevier.com/locate/jinorgbio

Mixed-1,10-phenanthroline–Cu(II) complexes: Synthesis, cytotoxic activity versus hematological and solid tumor cells and complex formation equilibria with glutathione

Tiziana Pivetta [a,*], Francesco Isaia [a], Gaetano Verani [a], Carla Cannas [a], Laura Serra [a], Carlo Castellano [c], Francesco Demartin [c], Federica Pilla [b], Matteo Manca [b], Alessandra Pani [b]

[a] Dipartimento di Scienze Chimiche e Geologiche, Università degli Studi di Cagliari, 09042 Monserrato (CA), Italy
[b] Dipartimento di Scienze Biomediche, Università degli Studi di Cagliari, 09042 Monserrato (CA), Italy
[c] Dipartimento di Chimica Strutturale e Stereochimica Inorganica, Università degli Studi di Milano, Via G. Venezian, 21-20133 Milano, Italy

ARTICLE INFO

Article history:
Received 8 January 2012
Received in revised form 25 April 2012
Accepted 26 April 2012
Available online 4 May 2012

Keywords:
Copper(II)
Glutathione
Phenanthroline
Cytotoxicity
Hematologic tumor
Solid tumor

ABSTRACT

Cu(II) complexes with 1,10-orthophenanthroline (phen) show cytotoxic and antitumoral effects. To enhance and exploit these features, we studied complexes containing one or two phen units together with N,N′-substituted-imidazolidine-2-thione (**L**). We synthesized and structurally characterized the precursor molecule $Cu(phen)(OH_2)_2(OClO_3)_2$, and determined the complex formation constants of $[Cu(phen)(\mathbf{L})]^{2+}$. We studied the cytotoxic activity of $[Cu(phen)_2(\mathbf{L})](ClO_4)_2$ versus human hematologic (CCRF-CEM and CCRF-SB) and solid tumor-derived cell lines (K-MES-1, DU-145). The cytotoxic activities, in the 1–3 μM range, show that our Cu(II)–complexes possess comparable inhibitory activities against both leukemia and carcinoma cells, unlike the majority of antineoplastic agents, usually more potent against hematologic cancer cells than against solid tumor cells. Because the free Cu(II) ion is reduced by glutathione (GSH), we studied the reactivity of our complexes with GSH, providing evidence that no redox reaction occurred under the chosen experimental conditions. Complex formation equilibria were present, studied by spectrophotometric titrations. The redox properties of the prepared compounds were also investigated by cyclic voltammetry, confirming that the mixed Cu(II) complexes were resistant to reduction.

1. Introduction

Copper(II) is involved in several biological processes, in particular in redox reactions [1,2], catalyzing the generation of reactive oxygen species. Complexes of copper(II) with 1,10-ortho-phenanthroline (phen) are capable of cleaving DNA [3,4] and improve nuclease activity [3,5–7] showing cytotoxic [8], genotoxic [9] and antitumoral effects[10], both in vitro and in vivo.

The couple Cu(II)/Cu(I) is also involved in the reactions with glutathione. In living systems, glutathione exists in two forms, reduced (GSH) and oxidized glutathione disulfide (GSSG). GSH prevents damage to important cellular components by forming complexes with several metal ions [11–14] and by reducing the Cu(II) ion [15]. As a consequence, the cytotoxicity of Cu(II) complexes may be strongly modified by reactions with GSH, inside or outside the cells. The reduced Cu(I)-complexes could lead to unexpected reactions and interfere with different molecular processes, all generating potential side effects.

Recently, we prepared a series of new copper(II) complexes, containing two phenanthrolinic units and N,N′-substituted-imidazolidine-2-thione (**L1**–**L4**, Fig. 1) as auxiliary ligands [16]; these compounds are characterized by a high chemical stability coupled with high cytotoxic activity against mouse neuroblastoma N2a cell lines. In the light of these results and with the aim of obtaining a molecule with improved cytotoxic or antiproliferative activity, it seemed very interesting to prepare new mixed compounds by varying the number of chelating units and auxiliary ligands. In addition, we deemed that it is fundamental to study the reactivity of these complexes in the presence of glutathione in order to verify their stability, and eventually to identify the possible by-reactions. We applied a multidisciplinary approach, covering many fields: bio-, analytical, inorganic and physic-chemistry. We synthesized and structurally characterized the Cu(II) complex $Cu(phen)_2(OH_2)_2(OClO_3)_2$, **1**; determined the complex formation constants of $[Cu(phen)]^{2+}$ with **L1**–**L4** and studied the reactivity of the chelate complexes $[Cu(phen)_x]^{2+}$ (where x = 1, 2, 3) and $[Cu(phen)_2\mathbf{L1}]^{2+}$ with GSH at pH 7.4 in 0.1 M phosphate buffer. Moreover we extended the study in vitro of the cytotoxic activity of **C1**–**C4** $[Cu(phen)_2\mathbf{L}]^{2+}$ complexes (**L** = **L1**–**L4**) to human hematologic tumor-derived cell lines, i.e. human acute T-lymphoblastic leukemia (CCRF-CEM) and acute B-lymphoblastic leukemia (CCRF-SB), and to

* Corresponding author at: Dipartimento di Scienze Chimiche e Geologiche, Università degli Studi di Cagliari, 09042 Monserrato (CA), Italy. Tel.: +39 0706754473; fax: +39 070584597.
E-mail address: tpivetta@unica.it (T. Pivetta).

0162-0134/$ – see front matter © 2012 Elsevier Inc. All rights reserved.
doi:10.1016/j.jinorgbio.2012.04.017

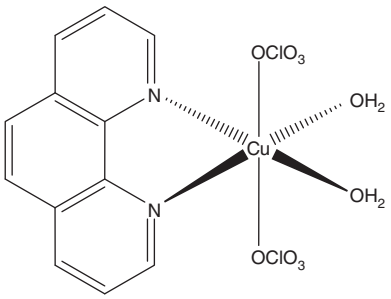

1
$Cu(phen)(OH_2)_2(OClO_3)_2$

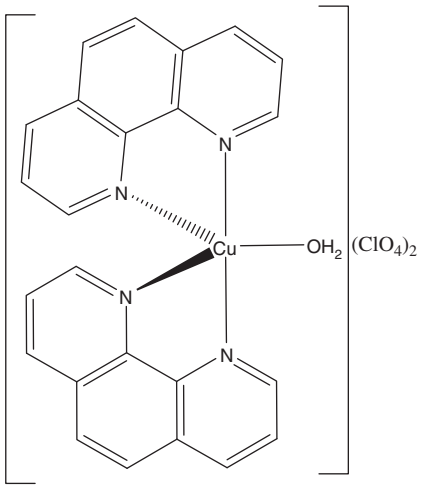

2
$[Cu(phen)_2(OH_2)](ClO_4)_2$

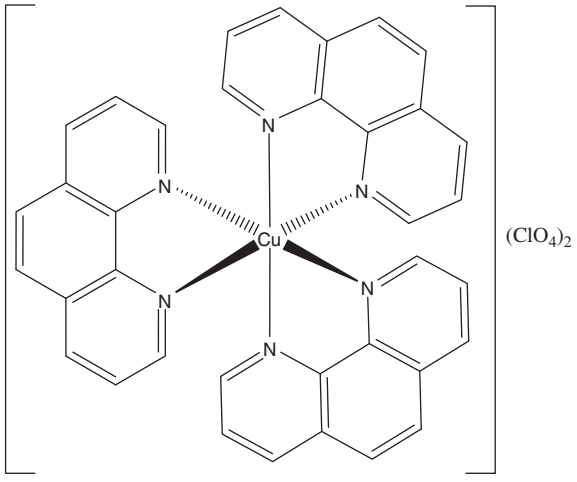

3
$[Cu(phen)_3](ClO_4)_2$

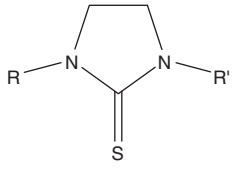

L1: R = R' = -H

L2: R = -H, R' = $-CH_3$

L3: R = R' = $-CH_3$

L4: R = -H, R' = $-CH_2CH_3$

Fig. 1. Acronyms and pictograms of the studied compounds.

solid tumor-derived cell lines, i.e. lung squamous carcinoma (K-MES-1) and prostate carcinoma (DU-145). The synthesized and studied complexes are shown in Fig. 1.

2. Experimental section

2.1. Materials and methods

2.1.1. Reagents

$Cu_2(CO_3)(OH)_2$, 1,10-phenanthroline monohydrate, glutathione, glutathione disulfide, perchloric acid, ethanol, ethylic ether, orthophosphoric acid, potassium hydroxide, dimethyl sulfoxide (DMSO), ethylenediaminetetraacetic acid (EDTA), and ligand **L1** were purchased from Sigma-Aldrich and used without any further purification. The stock solutions of Cu(II) compounds were prepared by dissolving the proper amount of sample in 0.1 M phosphate buffer of pH 7.4. The analytical concentration of Cu(II) was measured by spectrophotometric titration with EDTA. GSH purity was evaluated by elemental analysis. *CAUTION: Perchlorate complexes are potentially explosive, handle these compounds even in small amounts with care.*

2.1.2. UV–visible (UV–vis) spectrophotometric measurements

The UV–vis measurements were carried out with a Varian Cary 50 spectrometer equipped with an optical fiber dip probe with a 1 cm optical path length.

2.1.3. Conductometric measurements

The conductometric measurements were carried out with a AMEL 2131 - conductivity meter in aqueous solution at 20 °C.

2.1.4. Spectrophotometric titrations and constants definition

The complex formation equilibria were studied by a spectrophotometric titration, at 25 °C at pH 7.4 in a 0.1 M phosphate buffer, following the spectral variations due to the addition of the titrant. This method was applicable because the species formed at different titrant/titrand molar ratios were characterized by absorption peaks dissimilar for position and intensity [17,18]. Being the absorbance correlated to the species concentration, a complexation model was proposed and the experimental data were fitted minimizing the difference between the calculated and experimental absorbance. The equilibrium constants were expressed taking into account the following considerations and conventions.

The general equation for the equilibria of complex formation is shown by eq. 1 in Scheme 1, and the thermodynamic definition of the global formation constant (or overall association constant) is defined as $\beta_{p,q}$ (eq. 2), where the symbol {i} indicates the activity of the i-th species. It is straightforward that for the inverse equilibrium (eq. 3), the instability constant (or dissociation constant) of the complex M_pL_q is given by eq. 4. When a constant ionic medium is used, formal concentration terms are used in place of activities according to the definition of Schwarzenbach's side reaction coefficients (ξ_i) [19] as shown by eq. 5. It is clear that for systems where several equilibria take place, a set of equilibrium equations has to be considered. The overall formation constants of the type $\beta_{i,j}$ can be written as the product of the stepwise constants (Kj). For example, the overall formation constant for the species ML_n may be expressed as in eqs. 6 and 7.

The constants presented in the work were obtained by using the Hyperquad program [20], which uses the convention that all equilibrium constants are expressed as overall association constants.

2.1.5. I.R. spectrophotometric measurements

Infrared spectra were recorded in a Bruker Vector 22 spectrophotometer, preparing the samples as KBr pellets.

2.1.6. XPRD spectrophotometric measurements

X-ray powder diffraction patterns were recorded using a J–J diffractometer (Seifert X3000) with Bragg–Brentano geometry and CuKα radiation. Before the measurements, the samples were ground with an agate mortar and the obtained fine powders were dispersed in ethanol, sonicated, deposited drop by drop on a silicon zero background sample holder, and dried in air. The samples in the form of powders were observed in electron micrographs obtained using a transmission electron microscope (JEOL 200CX) operating at 200 kV. Finely ground samples were dispersed in n-octane and subjected to an ultrasonic bath. The suspensions were then dropped on carbon-coated copper grids for observation.

2.1.7. Cyclic voltammetry experiments

Cyclic voltammetry experiments were carried out on an Autolab PGSTAT12 potentiostat/galvanostat, equipped with a working-counter double-Pt electrode, an Ag/AgCl reference electrode, under an Ar atmosphere at 25 °C at pH 7.4 in 0.1 M phosphate buffer. The electrodes were rinsed with a 1:1 solution of HNO_3/H_2O_2 and washed with distilled water after each experiment. The solutions (5 mL) were degassed with Ar for 10 min before the measurements.

$$pM + qL \leftrightharpoons M_pL_q \quad (1)$$

$$\beta_{p,q} = \frac{\{M_pL_q\}}{\{M\}^p\{L\}^q} \quad (2)$$

$$M_pL_q \leftrightharpoons pM + qL \quad (3)$$

$$\beta^{inst}_{p,q} = \frac{1}{\beta_{p,q}} \quad (4)$$

$$\beta'_{p,q} = \frac{[M_pL_q]'}{[M]'^p[L]'^q} = \frac{\xi_{M_pL_q}}{\xi_M\xi_L} * \beta_{p,q} \quad (5)$$

$$\beta_n = K_1K_2K_3..K_n \text{ or } \log\beta_n = \log K_1 + \log K_2 + \log K_3 + \ldots + \log K_n \quad (6)$$

$$K_1 = \frac{[ML]}{[M][L]};\ K_2 = \frac{[ML_2]}{[M][L]^2};\ K_n = \frac{[ML_n]}{[M][L]^n} \quad (7)$$

Scheme 1. Equations used in the definition of the complex formation constants.

2.2. Synthesis

1: Concentrated perchloric acid (0.5 mL, 4.6 mmol) was slowly added to an ethanol suspension of $Cu_2(CO_3)(OH)_2$ (0.2 g, 1.8 mmol of Cu(II), 20 mL), stirring and warming until complete solubilization. The resulting deep blue solution was cooled and an ethanol solution of phen (0.09 g, 0.45 mmol, 20 mL) was added. The solution was filtered in order to remove any trace of the insoluble by-product **2**. The solution was concentrated under vacuum at approx. 5 mL of volume, and allowed to crystallize for 2 days. The deep blue crystals were filtered off and dried at room temperature. Percentage yield 43%; anal. calcd. for $Cu(phen)(OH_2)_2(ClO_4)_2$: C 30.11, H 2.53, N 5.85, found: C 29.78, H 2.49, N 5.78. IR (KBr cm^{-1}) selected bands ν(O–H) 3407, ν (phen group) 3079, 3052, 1585, 1520, 1424, 1347, 853, 722, 627; ν (perchlorate group) 1145, 1110, 1086. Blue crystals suitable for X-ray analysis were obtained and the crystal structure was solved. The powder X-ray diffraction (PXRD) spectrum was collected and indexed using the corresponding CIF file with the Mercury program [21] (Supplementary information (S.I.), Fig. S1a).

2: This compound was prepared as previously reported [16]. The PXRD spectrum was collected and indexed using the corresponding CIF file with the Mercury program [21] (S.I., Fig. S1b).

3: This compound was prepared by the reaction between **2** (0.3 g, 0.47 mmol) and phen (0.094 g, 0.47 mmol) in 40 mL of ethanol. The blue precipitate was filtered, washed with ethanol and dried at room temperature. Percentage yield 95%, anal. calcd. For **3**: C 53.84, H 3.01, N 10.46, found C 53.95, H 3.55, N 10.55.

C1–**C4**: The mixed compounds **C1**–**C4** $[Cu(phen)_2\mathbf{L}](ClO_4)_2$ (**L** = **L1**–**L4**) were prepared as previously reported [16]. Any attempt to obtain $[Cu(phen)L](ClO_4)_2$ in a solid state from water or water/CH_3CN solution led to the corresponding $[Cu(phen)_2L](ClO_4)_2$ compound. The PXRD spectrum of **C1** was collected and indexed using the corresponding CIF file with the Mercury program [21] (S.I., Fig. S1c).

3-GSH and **2**-GSH systems: 0.12 g of GSH (0.37 mmol, 10 mL) was added to a water suspension containing 0.30 g of **3** (0.37 mmol, 25 mL). A blue–violet precipitate was isolated, washed with water, and dried at room temperature (yield 68%); from the filtered solution, crystals of phen were recovered. 0.14 g of GSH (0.47 mmol, 10 mL) was added to a water suspension containing 0.30 g of **2** (0.47 mmol, 25 mL). A blue–violet precipitate was isolated, washed with water, and dried at room temperature (yield 75%). Both products were analyzed by I.R. and UV–vis spectroscopy, showing that they were identical. By adding HCl to a water suspension of the blue–violet compound, we observed the precipitation of GSH and **3** or **2**, then by adding NaOH, the blue–violet compound was reversibly regenerated. A portion of ≈0.08 g was treated with H_2O_2/HNO_3 to oxidize the possibly present Cu(I) to Cu(II) and titrated with EDTA, another portion was titrated as such; both titrations gave the same Cu(II) content (9.94%), showing that only Cu(II) ion was present in the sample. The blue–violet compound is stable even if exposed to air for several months.

2.3. Cell lines

The following human cell lines were purchased from the American Type Culture Collection (ATCC, USA): CCRF-CEM (acute T-lymphoblastic leukemia), CCRF-SB (acute B-lymphoblastic leukemia), K-MES-1 (lung squamous carcinoma), and DU-145 (prostate carcinoma). All cell lines were grown at 37 °C in a 5% CO_2 atmosphere in their specific media and according to ATCC instructions in the presence of 10% fetal calf serum (FCS), 100 U/mL penicillin, and 100 μg/mL streptomycin. All cell lines were maintained in exponential growth by periodically splitting high density suspension cultures (i.e. 10^6/mL) of CCRF-CEM and CCRF-SB, or when K-MES-1 and DU-145 cell monolayers reached sub-confluence. Cell cultures were periodically tested for the absence of mycoplasma contamination.

2.4. Cytotoxic assay

The cytotoxic effect of test compounds was evaluated in exponentially growing cell cultures. Stock solutions of test compounds were made at 1 mM in DMSO and stored at 4 °C in the dark. For the evaluation of cytotoxicity, each compound was serially diluted in specific growth medium for the different cell lines so that the concentration of DMSO was never higher than 0.1%. Leukemia and solid tumor cells were seeded at an initial density of 2×10^5 cells/mL in a flat-bottom 96-well plate in their specific media supplemented with 10% FCS and antibiotics as described above, and incubated overnight before the addition of 2× serial dilutions of test compounds. Cell growth in the absence and in the presence of test compounds was determined after 96 h of incubation, corresponding to three duplication rounds of untreated cells, by the 3-(4,5-dimethylthiazol-2-yl)-2,5-diphenyl-tetrazolium bromide (MTT) method [22]. Numbers of viable cells were also determined by the trypan blue dye exclusion method. Cell growth at each drug concentration was expressed as the percentage of untreated controls. The 50% cytotoxic concentration (CC_{50}) was determined from the dose–response curves by linear regression. Values are reported as the mean ± standard deviation of quadruplicate determinations for each drug concentration. Each compound was tested in at least three independent assays. Statistical analysis was performed with Student's *t*-test, and significance was set at $p \le 0.05$. The antitumor agent 6-mercaptopurine (6MP) was used as a reference compound.

2.5. Crystallographic data of **1**

$C_{12}H_{12}Cl_2CuN_2O_{10}$, $M = 478.68$, triclinic, $a = 7.840(2)$, $b = 10.591(2)$, $c = 10.905(2)$ Å, $\alpha = 76.06(3)$, $\beta = 75.80(3)$, $\gamma = 78.35(3)°$, $U = 842.0(3)$ Å^3, $T = 294(2)$ K, space group *P*-1 (no. 2), $Z = 2$, μ(Mo-Kα) 1.674 mm^{-1}. 9806 reflections (5126 unique; $R_{int} = 0.021$) were collected at room temperature in the range $3.94° < 2\theta < 62.76°$, employing a $0.13\times0.04\times0.03$ mm crystal mounted on a Bruker APEX II CCD diffractometer and using graphite-monochromatized Mo-Kα radiation (λ = 0.71073 Å). Final *R*1 [*wR*2] values were 0.0376 [0.1216] on $I > 2\sigma(I)$ [all data]. Datasets were corrected for Lorentz polarization effects and for absorption with the Siemens Area Detector Absorption (SADABS) correction program [23]. The structure was solved by direct methods (SIR-97) [24] and was completed by iterative cycles of full-matrix least squares refinement on F_o^2 and ΔF synthesis using the SHELXL-97 [25] program (WinGX suite) [26]. Hydrogen atoms located on the ΔF maps were allowed to ride on the carbon atoms for the phenanthroline ligand, whereas those of the water molecules were refined. Crystallographic data for compound **1** (excluding structure factors) have been deposited with the Cambridge Crystallographic Data Centre as supplementary publication no. CCDC-848420. These data can be obtained free of charge at www.ccdc.cam.ac.uk/conts/retrieving.html (or from the CCDC, 12 Union Road, Cambridge CB2 1EZ, UK; fax: +44 1223 336033; e-mail: deposit@ccdc.cam.ac.uk).

3. Results and discussion

3.1. Synthesis and crystal structure of **1**

The synthesis of **1** was carried out with a stoichiometric deficiency of phen in order to avoid the formation of the most stable complex **2**. The X-ray crystal structure of **1** has also been recently reported by Kaabi et al. [27]. It contains $[Cu(phen)(H_2O)_2]^{2+}$ cations with the copper atoms in octahedral coordination and perchlorate anions. The latter interact with the copper ion at the two apical positions of the coordination sphere, with Cu–O distances of 2.419(3) and 2.577(3) Å, respectively, and with one of the two water molecules through two intramolecular hydrogen bonds [O4…H3w-Ow2 140(5)°, O4…Ow2 2.807(7) Å; O6…H4w-Ow2 166(5)°, O6…Ow2 2.866(4) Å]. The phenanthroline ligand and the two water molecules occupy the equatorial positions of the octahedron. Intermolecular hydrogen bonds between the coordinated water molecules and the perchlorate anions are present: O6…H1w-Ow1 (1-x,1-y,1-z) 160(4)°, O6…Ow1 2.794(3) Å; O2…H2w-Ow1 (1 + x,y,z) 173(4)°, O2…Ow1 2.743(4) Å; O4…H3w-Ow2 (−x,1-y,1-z) 108(4)°, O4…Ow2 2.790(4) Å. In addition the phenanthroline units of adjacent complex molecules, are associated by π–π stacking interactions at a distance of about 3.54 Å, a value significantly lower than the limit value for π–π interaction of 3.8 Å [28].

The structure of the present complex is similar to that of Cu(2,2′-bipyridine)$(OH_2)_2(OClO_3)_2$ [29], also in this compound copper ion is coordinated by the perchlorate groups. Cu–N and Cu–O distances are longer in **1** (average Cu–N 1.988 Å vs. 1.977 Å; average Cu–O 2.498 Å vs 2.417 Å), while Cu–Ow distances are quite similar (1.964 Å vs. 1.967). The elongating effect of Cu–N and Cu–O distances might be due to the sterical hindrance of the phen, bigger than that of the 2,2′-bipyridine.

A comparison of the structure of **1** with that of $[Cu(phen)_2(H_2O)](ClO_4)_2$ [30], where the coordination of the copper ion is trigonal bipyramidal and no perchlorate anions interact with the metal ion, shows that the Cu–Ow distances are definitely shorter in our case (average 1.964(2) Å vs. 2.245(4) Å) whereas the Cu–N distances are almost comparable (1.993(2) Å vs. 2.007(3) Å). This shortening effect is in agreement with the different coordination number of the copper ion which in the present case displays a 4 + 2 coordination geometry instead of 5. Some views of the structure are reported in Fig. 2.

3.2. Conductometric measurements

In order to establish the kind of electrolyte of the studied copper compounds, the molar conductivity of their aqueous solution was measured. The values obtained, in the range 228–260 S cm^2 mol^{-1} (237 for **1**, 245 for **2**, 228 for **3**, 237 for **C1**, 260 for **C2** and **C3**, 235 for **C4**), show that all the complexes have electrolyte nature. Moreover, being the molar conductivity of the complexes comparable with that of $[Cu(phen)_3](ClO_4)_2$ which is definitely a 1:2 electrolyte, all the studied copper compounds have the same 1:2 electrolyte nature. This also means that in solution both the perchlorate anions are outside the copper coordination sphere.

3.3. Cytotoxic activity

We exploited the ability of Cu(II) complexes to inhibit the growth of tumor cells in vitro as a measure of their potential anticancer pharmacological effect. For each compound, we determined its CC_{50}, i.e. the drug concentration that inhibits cell growth by 50%. We employed four human cancer-derived cell lines: two from hematological cancers (CCRF-CEM acute T-lymphoblastic leukemia and CCRF-SB acute B-lymphoblastic leukemia) and two from carcinomas (K-MES-1 lung squamous carcinoma and DU-145 prostate carcinoma). The results are summarized in Table 1. Complexes **1** and **C1**–**C4** showed antiproliferative activity in the micromolar or submicromolar range, while ligands **L1**–**L4** were totally devoid of any inhibitory effect even at the maximum concentration tested (100 μM). Complex **2** appeared more cytotoxic than **1** due to the presence of two phen units. The insertion of the thionic ligands **L** on the core of **2** produced different effects on the corresponding cytotoxic activity towards the four tumor cell lines, most probably because of the different hydrophilicity/lipophilicity of the resulting molecules.

Lipophilicity/hydrophilicity of a molecule is correlated to the octanol/water partition coefficient P or more properly to the logP [31]. This property indicates the extent of diffusion of a molecule in the target organs. Log *p* value gives useful information for neutral molecules such as the organic ligands, but it is not adequate for the charged molecule and for strong electrolytes. Our complexes are strong electrolytes and are almost insoluble in octanol (no spectral variation occurred for the water solution of copper complexes before and after the contact with n-octanol). To distinguish the lipophilicity/hydrophilicity of our complexes we think it is useful to compare their calculated dipole moments, in fact the higher

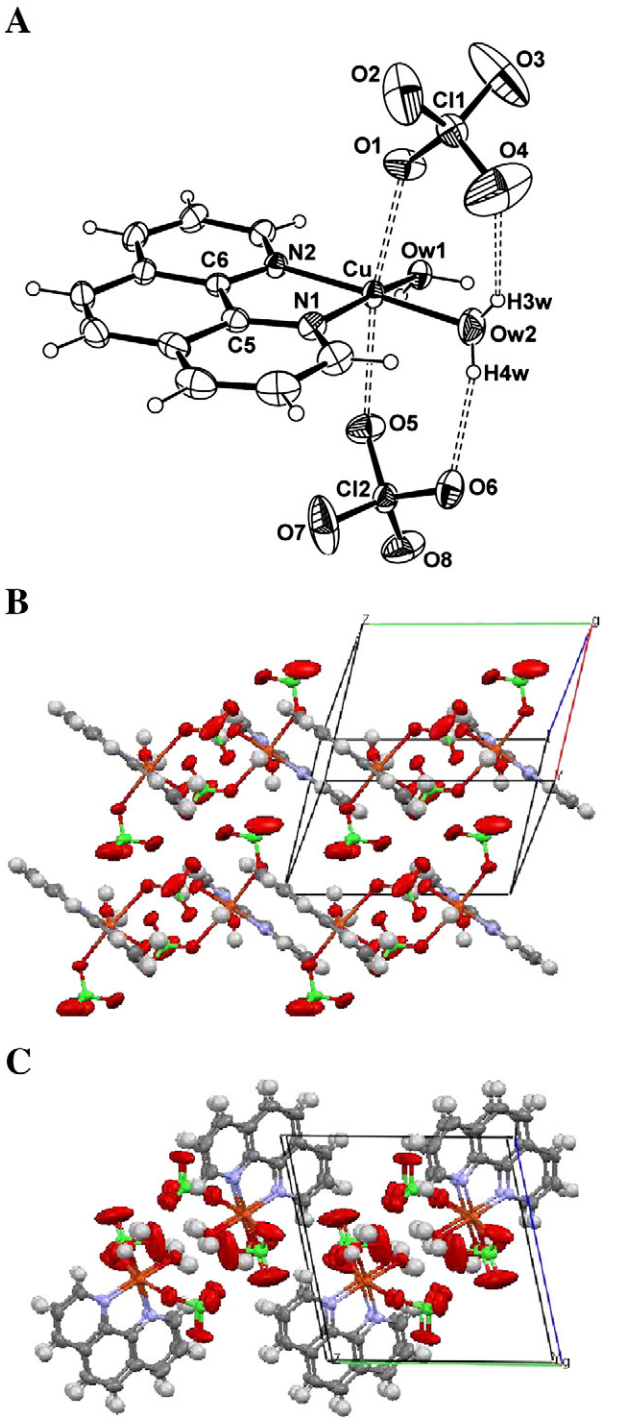

Fig. 2. ORTEP (A) and views of the crystal packing (B, C) of **1**.

the dipole moment, the higher the hydrophilicity. The dipole moment of our mixed complexes is in the order **C1** > **C2** > **C4** > **C3** (3.13, 2.06, 1.05 and 0.95 debye respectively). **C3** and **C4** derivatives with the thionic ligands featuring two methyl and one ethyl group respectively, present the lower dipole moment values and are more active with solid cancer than with leukemia, while **C1** and **C2** derivatives, the first unsubstituted and the second with only one methyl group, present the higher dipole moment values and are more active with hematological cancer cells. The correspondence of the dipole moment and the kind of activity, i.e. versus solid or liquid cancer cells, suggest that the choice of the substituents, which vary the lipophilicity/hydrophilicity, may play an important role in the selection of the proper drug in the treatment of the cancer cells.

Table 1
Cytotoxicity activity of the studied compounds reported as CC_{50}; the standard deviations of three independent experiments are reported in parentheses.

Comp.	CC_{50}[μM][a]			
	CCRF-CEM[b]	CCRF-SB[c]	SKMES-1[d]	DU145[e]
1	3.2 (1)	1.4 (1)	1.9 (1)	2.6 (3)
2	1.25 (2)	0.50 (5)	0.93 (6)	1.6 (2)
C1	0.80 (8)	0.70 (7)	0.85 (4)	1.6 (2)
C2	0.80 (8)	0.60 (5)	0.97 (7)	3.6 (4)
C3	0.90 (9)	0.80 (7)	0.7 (1)	1.50 (5)
C4	1.1 (1)	1.3 (1)	0.9 (1)	1.5 (2)
L1–L4	>100	>100	>100	>100
6MP[f]	2.0 (2)	0.70 (8)	>100	2.0 (1)

[a] CC_{50}, compound concentration required to reduce cell proliferation by 50%, as determined by the MTT method, under conditions allowing untreated controls to undergo at least three consecutive rounds of multiplication.
[b] CCRF-CEM CD4+, human acute T-lymphoblastic leukemia.
[c] CCRF-SB, human acute B-lymphoblastic leukemia.
[d] SKMES-1, human lung squamous carcinoma.
[e] DU145, human prostate carcinoma.
[f] 6MP, 6-mercaptopurine, usually used in combination with other drugs for maintenance therapy of acute lymphoblastic leukemia.

Unlike the majority of antineoplastic agents, which are usually markedly more potent against hematologic cancer cells than against solid tumor cells, all the studied Cu(II) complexes showed comparable inhibitory activities against both leukemic and carcinoma cells. The cytotoxic activity of our complexes result very interesting if compared with the activity of other metal complexes, in fact the most of the metal complexes and many drugs have a CC_{50} values in the range 10–20 μM. Cisplatinum for example has a 15 μM CC_{50} value for A-498 cell line and

Table 2
Complex formation constants for the system Cu(II)–phen-L.

System	$\log\beta_1$	$\log\beta_2$	$\log K_1$	$\log K_2$
Cu(II) + phen	8.14 (1)[a]	12.23(1)[a]	8.14	4.09
1 + **L1**	11.56 (1)[b]	15.16 (1)[b]	4.72	3.60
1 + **L2**	10.71 (1)[b]	13.48 (2)[b]	3.87	2.77
1 + **L3**	10.61 (2)[b]	13.26 (1)[b]	3.77	2.65
1 + **L4**	11.02 (1)[b]	13.54 (1)[b]	4.18	2.52

[a] 25°C, 0.1 M phosphate buffer, pH 7.4, aqueous solution.
[b] 25°C, 0.1 M $NaClO_4$, CH_3CN solution; the standard deviations to the last significant figure are reported in parentheses.

$$Cu^{II} + 2GS^{\cdot} \rightleftharpoons Cu^{II}(GS)_2 \quad \text{(i)}^*$$

$$Cu^{II}(GS)2 \rightharpoonup Cu^{I}(GS) + GS^{\cdot} \quad \text{(ii)}$$

$$2GS^{\cdot} \rightharpoonup GS\text{-}SG \quad \text{(iii)}$$

$$Cu^{II} + GS\text{-}SG \rightleftharpoons Cu^{II}(GS\text{-}SG) \quad \text{(iv)}$$

$$Cu^{II}(GS\text{-}SG) + Cu^{II} \rightleftharpoons Cu^{II}{}_2(GS\text{-}SG) \quad \text{(v)}$$

$$Cu^{I}\text{-complex} + O_2 \rightleftharpoons Cu^{II}\text{-complex} + O_2^{-\cdot} \quad \text{(vi)}$$

*The superscripts I and II are intended to emphasize the oxidation state of the metal ion.

Scheme 2. Reaction scheme for the system Cu(II) ion and glutathione; i–iii from Ref. [41], iv from Ref. [45] and vi from Ref. [46].

Table 3
Complex formation constants for the system Cu(II)–phen-**L1**-GSH; the standard deviations to the last significant figure are reported in parentheses (25 °C, 0.1 M phosphate buffer, pH 7.4, water solution).

Reaction[a]	log β	pK
$[Cu(phen)]^{2+} + L^{3-} \rightleftharpoons [Cu(phen)(L)]^{-}$	14.49 (1)	6.35[b]
$[Cu(phen)]^{2+} + 2L^{3-} \rightleftharpoons [Cu(phen)(L)_2]^{4-}$	18.93 (1)	4.44
$[Cu(phen)]^{2+} + 3L^{3-} \rightleftharpoons [Cu(phen)(L)_3]^{7-}$	23.06 (1)	4.13
$[Cu(phen)_2]^{2+} + L^{3-} \rightleftharpoons [Cu(phen)_2(L)]^{-}$	17.61 (1)	5.38[c]
$[Cu(phen)_2]^{2+} + 2L^{3-} \rightleftharpoons [Cu(phen)_2(L)_2]^{4-}$	22.68 (3)	5.07
$[Cu(phen)_2(\mathbf{L1})]^{2+} + L^{3-} \rightleftharpoons [Cu(phen)_2(\mathbf{L1})(L)]^{-}$	25.40 (2)	9.65[d]

[a] The values are expressed as association constants, glutathione is reported as L^{3-} (the real coordinating species) and not as HL^{2-}, because the proton is not involved in the reaction.
[b] Referred to the $[Cu(phen)]^{2+}$ species.
[c] Referred to the $[Cu(phen)_2]^{2+}$ species.
[d] Referred to the $[Cu(phen)_2(\mathbf{L1})]^{2+}$ species.

15 μM CC_{50} value for the Hep-G2 cell line; compounds with phen usually are more cytotoxic, in fact $[Cu(phen)_2(malonate)](ClO_4)_2$ presents 3.8 and 0.8 μM CC_{50} values for the same cell lines, respectively [32].

3.4. Complex formation constants of Cu(II)–phen-L systems

The complex formation constants for the Cu(II)–phen and **1**-**L** systems were determined by spectrophotometric titration in the 400–1100 nm region.

3.4.1. Cu(II)–phen system

In water solution at pH 7.4, 0.1 M phosphate buffer, only the species $[Cu(phen)]^{2+}$ and$[Cu(phen)_2]^{2+}$ could be spectrally studied, due to the low solubility of the $[Cu(phen)_3]^{2+}$, species observed in CH_3CN solution [16]. The complex formation constants for the $[Cu(phen)]^{2+}$ and $[Cu(phen)_2]^{2+}$ species are shown in Table 2.

3.4.2. **1**-**L** *systems*

The UV–vis spectrophotometric titrations of **1** with the thionic ligands **L1**–**L4** were carried out in CH_3CN solution in 0.1 M $NaClO_4$, due to the low solubility of **L1**–**L4** in water solution. The spectrum of the blue **1** compound in CH_3CN shows a peak at 670 nm, and, in analogy with the blue complex $[Cu(phen)_3]^{2+}$ which shows a similar spectrum with a peak at 675 nm, an octahedral coordination around the metal

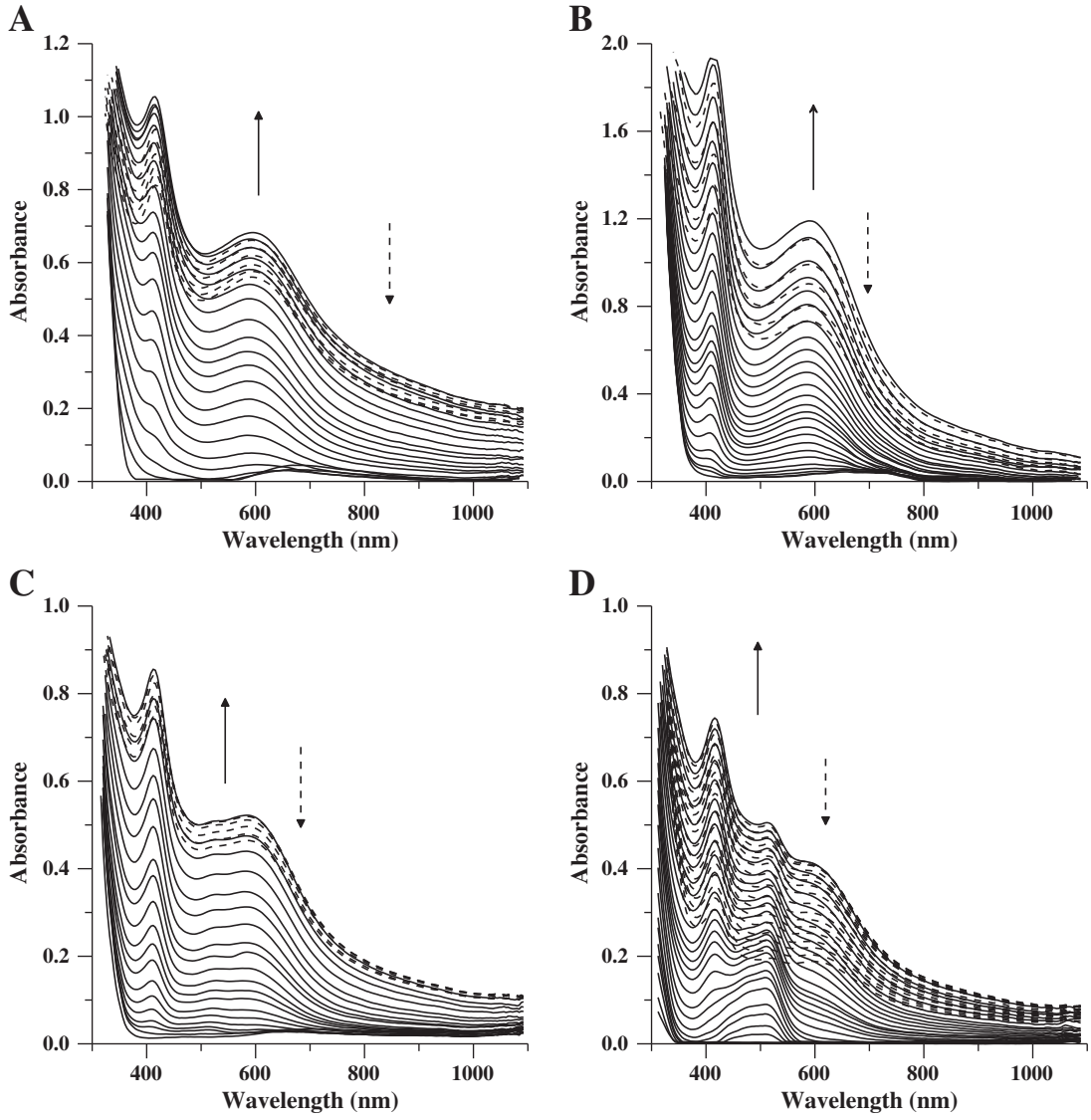

Fig. 3. Some spectra recorded during the titration of (A) 5.04×10^{-3} mmol of **1** (5.00 mL) with GSH, [GSH] = 1.20×10^{-3} M, (B) 3.94×10^{-3} mmol of **2** (4.99 mL) with GSH, [GSH] = 1.05×10^{-3} M, (C) 9.96×10^{-4} mmol of **C1** (6.00 mL) with GSH [GSH] = 1.11×10^{-3} M, (D) 5.69×10^{-3} mmol of GSH (5.00 mL) with **2**, [**2**] = 3.25×10^{-4} M; l = 1 cm, T = 25 °C, pH 7.4, 0.1 M phosphate buffer.

ion may be hypothesized, such $[Cu(phen)(CH_3CN)_4]^{2+}$. By adding 1 equivalent of the thionic ligands, the peak at 670 nm and its shoulder increases in intensity; with the further addition of 1 equivalent of **L**, the maximum shifts to higher wavelength and, at the end of the titration, a peak appears at ≈760 nm with a shoulder at higher wavelengths. The final solution is green colored. The same behavior is observed for all the ligands, due to the formation of two complexes with 1:1 and 1:2 Cu(II)/**L** molar ratios. The formation of these complexes and the corresponding stoichiometry were also checked by the Job's method [33]. In these two species, the penta-coordination around the metal ion could be established by their spectra [16,34–37] and the formula $[Cu(phen)\mathbf{L}(CH_3CN)_2]^{2+}$ and $[Cu(phen)\mathbf{L}_2(CH_3CN)]^{2+}$ may be hypothesized. The complex formation constants for the **1**-**L** systems are reported in Table 2. The $\log K_1$ for the $[Cu(phen)(\mathbf{L})(solv)_2]^{2+}$ species follows the substituent order: **L1** > **L4** > **L2** > **L3**, while the $\log K_2$ for the $[Cu(phen)(\mathbf{L})_2(solv)]^{2+}$ species follows the substituent order: **L1** > **L2** > **L3** > **L4**.

3.5. Reactivity with GSH

The chemistry of the copper–glutathione system appears to be controversial. In fact, some authors have studied the reactivity of Cu(II) ions with GSH without considering or observing the reduction of the metal ion [38,39], while some others have detected the reduction to Cu(I) and the formation of GSSG [40]. In most studies, the reduction of Cu(II) to Cu(I) and the oxidation of GSH to GSSG were observed by a direct reaction between Cu(II) salts and GSH; EPR measurements have provided evidence that the first step of the overall process is the formation of a transient complex between GSH and Cu(II), with $Cu^{II}(GS)_2$ stoichiometry (Scheme 2, eq. i). The lifetimes of these species, together with their colors, varying from violet to red [41], are strongly dependent on the pH of the medium [42,43]. In some cases, the violet compound was attributed to a reversible reaction of a Cu(I) complex with oxygen from the air [44]. With all these considerations, it is clear that the system is particularly intricate, and that the involved reactions depend on many experimental variables. Summarizing the literature data, the reactions reported in Scheme 2 have been proposed [41,45,46].

In contrast with most of the studies, in which free Cu(II) ion plays the lead role, we studied the reactivity of GSH with the Cu(II)-complexes **1**, **2**, and **C1**. In these species, the copper(II) oxidation state is stabilized by the phen unit(s), as shown by the complex formation between **1** and **2** with **L1**–**L4**, which are able to reduce free Cu(II) ions in a very fast reaction (this work and Ref. [16]).

Adding GSH to a buffered solution of complexes **1**, **2**, and **C1** (10^{-3} M), the initial light blue solution readily turned a stable dark blue–violet color with the formation of bands at ≈410 and 600 nm. These bands can be ascribed to the formation of one or more Cu(II) complexes with GSH and not to the reduction of Cu(II) to Cu(I). In fact, $[Cu^{I}(phen)]^{+}$ does not absorb in the visible region [47,48] and $[Cu^{I}(phen)_2]^{+}$ is characterized by a peak at 435 nm and a broad band at 530 nm. Moreover, under the chosen experimental conditions, no visible spectral changes occurred in the reaction of $[Cu^{I}(phen)_x]^{+}$ and GSH or GSSG, nor with $[Cu^{II}(phen)_x]^{2+}$ and GSSG. To test the possibility that the blue–violet species could be due to the reaction of some Cu(I) complex with oxygen, as in eq. vi, we performed the experiments under an Ar atmosphere, and we found that the formation of the blue–violet species was even faster in absence of oxygen (S. I., Table S1). The different results reported by other authors, as for example Gilbert [49], who observed the formation of the Cu(I) complexes $[Cu^{I}(phen)_2]^{+}$ and $Cu^{I}(phen)(GS)$ in the reaction of $[Cu^{II}(phen)_2]^{2+}$ with GSH, might be explained considering the different experimental conditions such as the concentration of the buffer and/or reactants, which are particularly critical in radical-involving reactions. Once verified that the redox reaction of our systems with GSH under the chosen experimental conditions was not observed, we studied the involved equilibria by spectrophotometric titrations.

3.5.1. Complex formation constants for the systems 1, 2, and C1 with GSH

Our studies were carried out in water solution at pH 7.4 in 0.1 M phosphate buffer; at this pH, GSH is present almost as a bis-deprotonated species being the log of the dissociation constants 9.07 (cysteine -SH), 3.48 (glycine –COOH) and 2.3 (glutamyl –COOH) [11].

All the calculated complex formation constants for the studied systems are shown in Table 3.

*3.5.1.1. **1**-GSH system.* 5.04×10^{-3} mmol of **1** (5.00 mL) was titrated with GSH (1.20×10^{-3} M). The solution spectrum of **1** (Fig. 3A) presents a peak at 670 nm. With the addition of 1 equivalent of GSH, a band at 420 nm appears; with the addition of further 1 equivalent, two peaks at 585 and 416 nm appear; and with the addition of the third equivalent, the intensity of the spectra starts decreasing but with a different profile showing that at least three equilibria were present. The titration data suggest the formation of three complexes with the proposed stoichiometry $[Cu(phen)(GS)]^{-}$, $[Cu(phen)(GS)_2]^{4-}$ and $[Cu(phen)(GS)_3]^{7-}$ as reported in Scheme 3.

*3.5.1.2. **2**-GSH system.* 3.94×10^{-3} mmol of **2** (4.00 mL) was titrated with GSH (1.05×10^{-3} M). The solution spectrum of **2** (Fig. 3B) presents two peaks at 720 and 950 nm with a shape typical of an octahedral coordinated metal ion [16,34–37]. By adding 1 equivalent of the GSH solution, two bands appear at 414 and 584 nm with an intensity ratio of 1.7; with the addition of the second equivalent of GSH, the band intensities start decreasing with a different intensity ratio and profile. On the contrary, adding 1 equivalent of **2** to the GSH solution (5.69×10^{-3} mmol, 5.00 mL, Fig. 3D), a convoluted band appears at 516 nm, and with the addition of the second equivalent of **2**, two more peaks appear at 416 and 604 nm. Increasing the amount of **2** the three bands decrease in intensity with the dilution but without profile changes. Although different species seemed to be formed in these two titrations, by decomposition of the experimental bands into Gaussian primitives, all the spectra could be fitted with the same parameters (four bands at 409, 502, 606,

1-GSH**

$$[Cu(phen)]^{2+} + HGS^{2-} \rightleftharpoons [Cu(phen)(GS)]^{-} + H^{+}$$

$$[Cu(phen)(GS)]^{-} + HGS^{2-} \rightleftharpoons [Cu(phen)(GS)_2]^{4-} + H^{+}$$

$$[Cu(phen)(GS)_2]^{4-} + HGS^{2-} \rightleftharpoons [Cu(phen)(GS)_3]^{7-} + H^{+}$$

2-GSH**

$$[Cu(phen)_2]^{2+} + HGS^{2-} \rightleftharpoons [Cu(phen)_2(GS)]^{-} + H^{+}$$

$$[Cu(phen)_2(GS)]^{-} + HGS^{2-} \rightleftharpoons [Cu(phen)_2(GS)_2]^{4-} + H^{+}$$

C1-GSH**

$$[Cu(phen)_2(\mathbf{L1})]^{2+} + HGS^{2-} \rightleftharpoons [Cu(phen)_2(\mathbf{L1})(GS)]^{-} + H^{+}$$

$$[Cu(phen)_2(\mathbf{L1})(GS)]^{-} + HGS^{2-} \rightleftharpoons [Cu(phen)_2(GS)_2]^{4-} + \mathbf{L1} + H^{+}$$

$$[Cu(phen)_2(GS)_2]^{4-} + HGS^{2-}{}_{(exc)} \rightleftharpoons [Cu(phen)(GS)_3]^{7-} + phen + H^{+}$$

* GSH is intended as triprotic molecule (H_3GS)
** The studies were carried out in water solution at pH 7.4 in 0.1 M phosphate buffer; at this pH, GSH is present almost as a bis-deprotonated species HGS^{2-}.

Scheme 3. Reaction scheme for the systems **1**, **2** and **C1** with GSH*.

and 833 nm), showing that the same species are present but in different concentrations. Therefore, the experimental data of both the titrations were fitted simultaneously, confirming the formation of two complexes, $[Cu(phen)_2(GS)]^-$ and $[Cu(phen)_2(GS)_2]^{4-}$ (Scheme 3). These two species are characterized by similar spectra but with different absorptivity values.

3.5.1.3. **C1-GSH** *system.* 9.96×10^{-4} mmol of **C1** (6.00 mL) was titrated with GSH (1.11×10^{-3} M). By adding 1 equivalent of GSH to the **C1** solution (Fig. 3C), a $[Cu(phen)_2(\mathbf{L1})(GS)]^-$ complex is formed; by the addition of an excess of GSH, further spectral changes are evident due to the formation of two complexes identified by their absorptivity as $[Cu(phen)_2(GS)_2]^{4-}$ and $[Cu(phen)(GS)_3]^{7-}$, indicating that the thionic ligand and a phen unit were removed from the coordination sphere, (Scheme 3).

Complexes formed by **1**, **2**, or **C1** with GSH present absorptivity values typical of a charge-transfer transition (S.I., Table S2), while the Cu(II)-GSSG species presents an absorptivity value ($60\ M^{-1}\,cm^{-1}$)

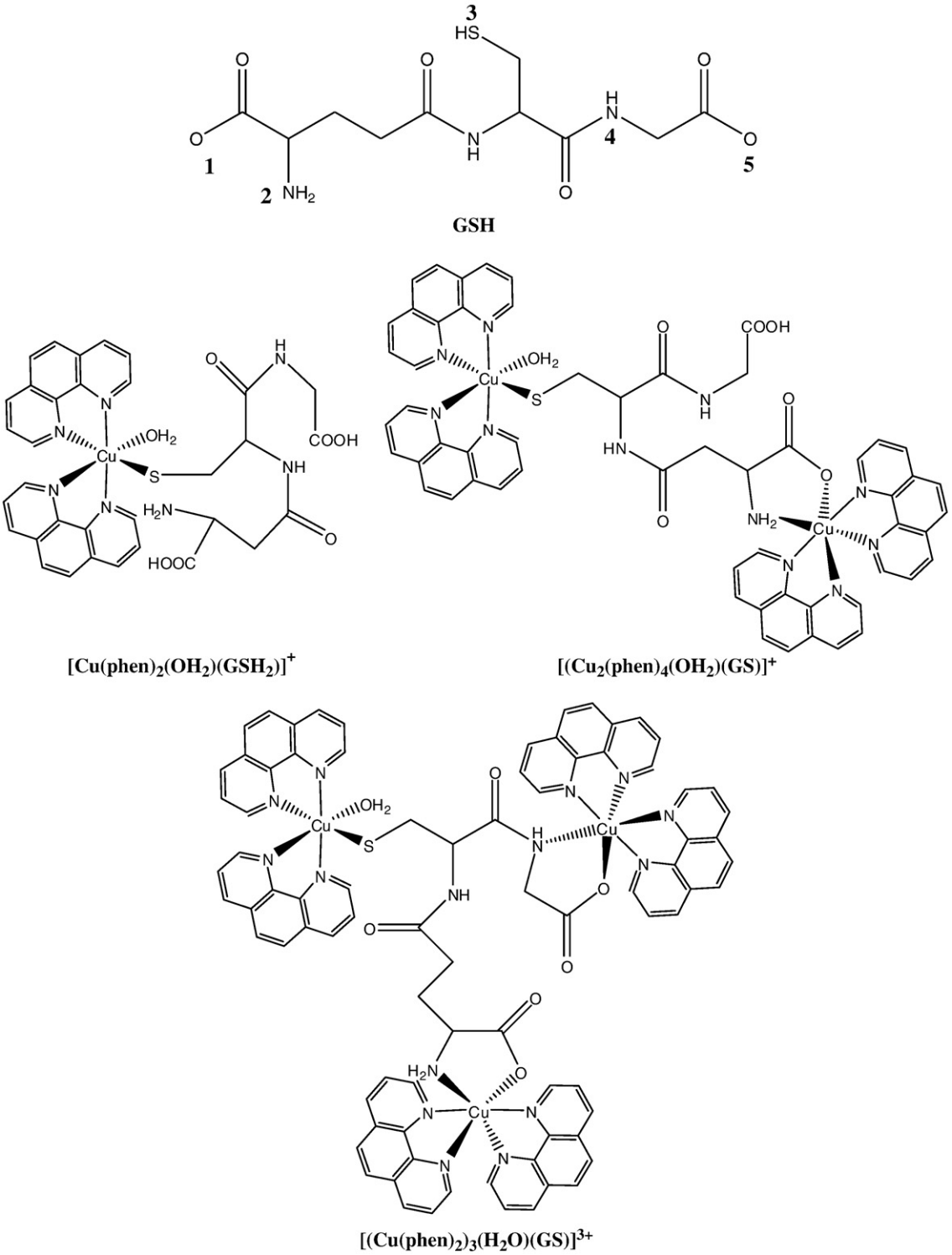

Scheme 4. Numbering sequence of GSH donor atoms and hypothesized coordination of GSH with **2**.

characteristic of a d–d electronic transition [45]. In particular, the band at ≈414 nm, present in all the spectra, has an absorptivity value typical of a ligand-to-metal charge transfer transition (LMCT) and was assigned using extended Huckel-type molecular orbital calculation, related to the unpaired electron of Cu(II) ion [50]. The position of this band arises from the ligand characteristics and allows the identification of the type of coordination, particularly for the sulfur-containing ligands; in fact, a band in the 454–384 nm range is typical of a coordinating thiolate RS^- ligand [51]. The hypothesis that GSH could substitute a phen unit, as in **C1**, was also proved by studying the reaction of **2** and **3** with GSH in pure water. In fact, the same blue–violet compound was isolated in both cases, and, from the filtered solution of **3**-GSH, white crystals of phen were recovered. The elemental analysis of the obtained compound gave the following percentages: C 53.27%, H 3.47%, and N 10.13%. The copper content (9.95%) was determined by titration with EDTA. The IR spectrum presents a well-resolved peak at 1100 cm^{-1} of the perchlorate anion and peaks at 630, 710, 850, 1450, and 1530 cm^{-1} due to the phen ligands. No signal of the –SH group is present. This product was also studied by transmission electronic microscopy (TEM) and PXRD. From the TEM measurements (S.I., Fig. S2), information on the morphology and average size of the crystals was obtained, pointing out the presence of a great number of crystallites with rod shapes. Any attempt to isolate a single crystal suitable for X-ray analysis was unsuccessful, and for this reason we tested the crystalline nature of the particles by PXRD (S.I., Fig. S3), verifying in particular the absence of the pattern profile of $[Cu^I(phen)_x]^+$, Cu^I/Cu^{II} oxide, Cu^0, or uncoordinated GSH (GSSG is amorphous). On the basis of the tests and the elemental analysis, an unequivocal formula could not be proposed, but at least three different hypotheses have to be taken into account, i.e. the formation of the mononuclear complex i) $[Cu(phen)_2(OH_2)(GSH_2)](ClO_4)$, or the polynuclear complexes ii) $[(Cu(phen)_2)_2(H_2O)(GS)](ClO_4)$, or iii) $[(Cu(phen)_2)_3(H_2O)(GS)](ClO_4)_3$. As the –SH signal is missing in the I.R. spectrum, it is clear that the sulfur atom participates in the coordination, then, in the presence of more than one metal ion, carboxylate and amino groups are also involved in the coordination as represented in Scheme 4 (the used numbering sequence of donor atoms is also shown). For the species $[Cu(phen)_2(GSH_2)](ClO_4)$, three isomers are possible (1–2, 4–5, and 1–5 coordinating atoms). All the coordination modes were studied by quantomechanical methods. Molecules as in i), ii), and iii) were built and their geometries were optimized by semi-empirical methods using a PM3 basis set [52], with the program SPARTAN'06 for Windows (Wavefunction Inc.). Molecules with an octahedral coordination core around the copper(II) ion were found to be the most stable. For ii), the isomer with 1–2 donor atoms had the lowest enthalpy formation energy. The optimized geometry for all the isomers and the corresponding formation enthalpies are reported in the S. I. (Fig. S4); the most stable isomers are shown in Scheme 4.

3.6. Cyclic voltammetry experiments

Redox properties of **1**, **2**, **3**, **C1**, and GSH were studied by cyclic voltammetry (S.I., Fig. S5). Compounds **1**, **2**, and **3** are characterized by two well-defined cathodic peaks and at least one poorly resolved anodic peak; while the peaks not detectable by direct examination of the voltammogram were shown by derivative analysis. All the compounds exhibit two one-electron potential waves belonging to the Cu^{II}/Cu^I and Cu^I/Cu^0 redox reactions (E_p (mV): −105 and 280 for **1**, 10 and 146 for **2**, −81 and 145 for **3**, −25 for **C1** and 300 for GSH). The redox reactions of **1** appear to be quasi-reversible. The distance between the cathodic peaks lowers passing from **1** to **2** and **3**. The intensity of the two cathodic peaks was comparable in **1**, while the more negative peak diminishes in intensity passing to **2** and **3**. In the voltammogram of **C1**, only one cathodic peak is evident and an anodic peak is present at a very high potential value. The GSH redox reaction appeared to be irreversible; in fact, only the reduction peak of GSSG was evident at each cycle. As can be seen by analyzing the potential values, under the chosen experimental conditions, copper(II) complexes are not reduced by GSH.

4. Conclusions

Copper(II) complexes with 1,10-orthophenanthroline (phen), $Cu(phen)(OH_2)_2(ClO_4)_2$ (**1**), $[Cu(phen)_2(OH_2)](ClO_4)_2$ (**2**) and $[Cu(phen)_3](ClO_4)_2$ (**3**) were synthesized and the crystal structure of **1** was solved. Mixed complexes $[Cu(phen)(\mathbf{L})]^{2+}$ (where L = N,N′-substituted-imidazolidine-2-thione) were synthesized, and the complex formation constants were evaluated. The cytotoxicity study of $[Cu(phen)_2(\mathbf{L})]^{2+}$ was extended to four tumor cell lines, showing good activity. The tested compounds are characterized by CC_{50} values in the range of 1–3 μM for very deadly types of cancers such as squamous lung cancer and prostate carcinoma. All complexes showed comparable inhibitory activities against both leukemia and carcinoma cells, unlike the majority of antineoplastic agents which are usually markedly more potent against hematologic cancer cells than solid tumor cells. The insertion of the thionic ligands **L** on the core of **2** produced different effects on the corresponding cytotoxic activity towards the four tumor cell lines, most probably because of the different hydrophilicity/lipophilicity of the resulting molecules. **C3** and **C4** derivatives, presenting the lower dipole moment calculated values, are more active with solid cancer than with leukemia, while **C1** and **C2** derivatives, presenting the higher dipole moment values, are more active with hematological cancer cells. The correspondence of the dipole moment and the kind of activity, i.e. versus solid or liquid cancer cells, suggest that the choice of the substituents, which vary the lipophilicity/hydrophilicity, may play an important role in the selection of the proper drug in the treatment of the cancer cells. Although none of tested compounds emerged as a lead compound in terms of anticancer potency, our results represent very promising preliminary data. UV–vis and cyclic voltammetry experiments showed that the Cu(II) ion in complexes **1**, **2**, **3**, and **C1** is not reduced by the tripeptide glutathione GSH which acted as a coordinating ligand only. In particular, as evidenced by spectrophotometric analysis, the **1**-GSH system leads to the formation of complexes with the proposed stoichiometry $[Cu(phen)(GS)]^-$, $[Cu(phen)(GS)_2]^{4-}$, and $[Cu(phen)(GS)_3]^{7-}$, where GSH binds the Cu(II) via the thiolate sulfur atom. In the case of the **2**-GSH system, the presence of two phen units crowding the copper center allows the entry of only one or two GSH units to form the complexes $[Cu(phen)_2(GS)]^-$ and $[Cu(phen)_2(GS)_2]^{4-}$. In the case of the **C1**-GSH system, the complex $[Cu(phen)_2(\mathbf{L1})(GS)]^-$ is formed; however, the substitution of **L1** with a GSH unit was only observed for **C1**/GSH molar ratios higher than 1. An interesting stable blue–violet solid is separated from the reaction of **3** or **2** with GSH. The above reported experimental data and the quantum mechanical calculations suggest the formation of the mononuclear compound $[Cu(phen)_2(OH_2)(GSH_2)](ClO_4)$ or the polynuclear compounds $[(Cu(phen)_2)_2(H_2O)(GS)](ClO_4)$ or $[(Cu(phen)_2)_3(H_2O)(GS)](ClO_4)_3$. Moreover, we have shown that under our experimental conditions, reagent concentration, temperature, and pH are important factors in driving the reaction towards either complex formation or electron exchange.

Appendix A. Supplementary data

Supplementary data to this article can be found online at http://dx.doi.org/10.1016/j.jinorgbio.2012.04.017.

References

[1] J.R. Sorenson, Prog. Med. Chem. 26 (1989) 437–568.
[2] G. Psomas, A. Tarushi, E.K. Efthimiadou, Y. Sanakis, C.P. Raptopoulou, N. Katsaros, J. Inorg. Biochem. 100 (2006) 1764–1773.
[3] F.Q. Liu, Q. Wang, K. Jiao, F. Jian, G. Liu, R. Li, Inorg. Chim. Acta 359 (2006) 1524–1530.
[4] D.S. Sigman, A. Mazumder, D.M. Perrin, Chem. Rev. 93 (1993) 2295–2316.
[5] C. Dendrinou-Samara, G. Psomas, C.P. Raptopoulou, D.P. Kessissoglou, J. Inorg. Biochem. 83 (2001) 7–16.
[6] B.K. Santra, P.A.N. Reddy, G. Neelakanta, S. Mahadevan, M. Nethaji, A.R. Chakravartym, J. Inorg. Biochem. 89 (2002) 191–196.
[7] L.Z. Li, C. Zhao, T. Xu, H. Ji, Y. Yu, G. Guo, H. Chao, J. Inorg. Biochem. 99 (2005) 1076–1082.

[8] I. Gracia-Mora, L. Ruiz-Ramírez, C. Gómez-Ruiz, M. Tinoco-Méndez, A. Márquez-Quiñones, L. Romero-De Lira, A. Marín-Hernández, L. Macías-Rosales, M.E. Bravo-Gómez, Met.-Based Drugs 8 (2001) 19–28.
[9] R. Alemon-Medina, M. Brena-Valle, J.L. Munoz-Sanchez, M.I. Gracia-Mora, L. Ruiz-Azuara, Cancer Chemother. Pharmacol. 60 (2007) 219–228.
[10] F. Carvallo-Chaigneau, C. Trejo-Solis, C. Gomez-Ruiz, E. Rodriguez-Aguilera, L. Macias-Rosales, E. Cortes-Barberena, C. Cedillo-Pelaez, I. Gracia-Mora, L. Ruiz-Azuara, V. Madrid-Marina, Biometals 21 (2008) 17–28.
[11] A. Corazza, I. Harvey, P.J. Sadler, Eur. J. Biochem. 236 (1996) 697–705.
[12] I. Jimenez, P. Aracena, M. Letelier, P. Navarro, H. Speisky, Toxicol. In Vitro 16 (2002) 167–175.
[13] M. Letelier, A.M. Lepe, M. Faundez, J. Salazar, R. Marin, P. Aracena, H. Speisky, Chem. Biol. Interact. 151 (2005) 71–82.
[14] R.N. Bose, S. Moghaddas, E.L. Weaver, E.H. Cox, Inorg. Chem. 34 (1995) 5878–5883.
[15] E.M. Kosower, in: I.M. Arias, E.B. Jakoby (Eds.), Glutathione: Metabolism and Function, Raven Press, New York, 1976, p. 1.
[16] T. Pivetta, M.D. Cannas, F. Demartin, C. Castellano, S. Vascellari, G. Verani, F. Isaia, J. Inorg. Biochem. 105 (2011) 211–220.
[17] F.J.C. Rossotti, H. Rossotti, The Determination of Stability Constants, McGraw-Hill, 1961.
[18] M. Meloun, J. Havel, E. Högfeldt, Computation of Solution Equilibria — A Guide to Methods in Potentiometry, Extraction and Spectrophotometry, Ellis Horwood, Chichester, 1988 297 pages, ISBN 0-7458-0201-X.
[19] A. Ringbom, J. Chem. Educ. 35 (6) (1958) 282–288.
[20] P. Gans, A. Sabatini, A. Vacca, Talanta 43 (1996) 1739–1753.
[21] C.F. Macrae, P.R. Edgington, P. McCabe, E. Pidcock, G.P. Shields, R. Taylor, M. Towler, J. van de Streek, J. Appl. Crystallogr. 39 (2006) 453–457.
[22] R. Pauwels, J. Balzarini, M. Baba, R. Snoeck, D. Schols, P. Herdewijn, J. Desmyster, E. De Clercq, J. Virol. Meth. 20 (1988) 309–321.
[23] SADABS Area-detector Absorption Correction Program, Bruker AXS Inc., Madison, WI, USA, 2000.
[24] A. Altomare, M.C. Burla, M. Camalli, G.L. Cascarano, C. Giacovazzo, A. Guagliardi, A.G.G. Moliterni, G. Polidori, R. Spagna, J. Appl. Crystallogr. 32 (1999) 115–119.
[25] G.M. Sheldrick, Acta Crystallogr. A64 (2008) 112–122.
[26] L.J. Farrugia, J. Appl. Crystallogr. 32 (1999) 837–838.
[27] K. Kaabi, M. El Glaoui, M. Zeller, C.B. Nasr, Acta Crystallogr. E Struct. Rep. Online (2010) m1145–m1146.
[28] J. Janiak, J. Chem. Soc., Dalton Trans. (2000) 3885–3896.
[29] M. Damous, M. Hamlaoui, S. Bouacida, H. Merazig, J.C. Daran, Acta Crystallogr. E67 (2011) m611–m612.
[30] G. Murphy, C. Murphy, B. Murphy, B. Hathaway, J. Chem. Soc., Dalton Trans. (1997) 2653–2660.
[31] A. Leo, C. Hansch, D. Elkins, Chem. Rev. 71 (1971) 525–616.
[32] C. Deegan, M. McCann, M. Devereux, B. Coyle, D.A. Egan, Cancer Lett. 247 (2007) 224–233.
[33] P. Job, Ann. Chim. (Paris) 9 (1928) 113–203.
[34] J. Foley, D. Kennefick, D. Phelan, S. Tyagi, B. Hathaway, J. Chem. Soc., Dalton Trans. (1983) 2333–2338.
[35] B.J. Hathaway, D.E. Billing, Coord. Chem. Rev. 5 (1970) 143–207.
[36] Z.L. Lu, C.Y. Duan, Y.P. Tian, X.Z. You, X.Y. Huang, Inorg. Chem. 35 (1996) 2253–2258.
[37] A.W. Addison, T.N. Rao, J. Reedijk, J. Van Rijn, G.C. Verschoor, J. Chem. Soc., Dalton Trans. (1984) 1349–1356.
[38] P.W. Albro, J.T. Corbett, J.L. Schroeder, J. Inorg. Biochem. 27 (1986) 191–203.
[39] B. Jezowska-Trzebiatowska, G. Formicka-Kozlowska, H. Kozlowski, J. Inorg. Nucl. Chem. 39 (1977) 1265–1268.
[40] M.R. Ciriolo, A. Desideri, M. Paci, G. Rotilio, J. Biol. Chem. 265 (1990) 11030–11034.
[41] N.D. Yordanov, Trans. Met. Chem. 22 (1997) 200–207.
[42] E.W. Ainscough, A.G. Bingham, A.M. Broide, Inorg. Chim. Acta 138 (1987) 175–177.
[43] J.M. Downes, J. Whelan, B. Bosnich, Inorg. Chem. 20 (1981) 1081–1086.
[44] B. Loeb, I. Crivelli, C. Andrade, Inorg. Chim. Acta 231 (1995) 21–27.
[45] W.S. Postal, E.J. Vogel, C.M. Young, F.T. Greenaway, J. Inorg. Biochem. 25 (1985) 25–33.
[46] H. Speisky, M. Gomez, F. Burgos-Bravo, C. Lopez-Alarcon, C. Jullian, C. Olea-Azar, M.E. Aliaga, Bioorg. Med. Chem. 17 (2009) 1803–1810.
[47] G.F. Smith, Anal. Chem. 26 (1954) 1534–1538.
[48] R.T. Pflaum, W.N. Brandt, J. Am. Chem. Soc. 72 (1955) 2019–2022.
[49] B.C. Gilbert, S. Silvester, P.H. Walton, J. Chem. Soc., Perkin Trans. 2 (1999) 1115–1121.
[50] B.J. Hathaway, in: G. Wilkinson, R.D. Gillard, J.A. McCleverty (Eds.), Comprehensive Coordination Chemistry, vol. 5, Pergamon, Oxford, 1987, p. 679.
[51] E.I. Solomon, K.W. Penfield, D.E. Wilcox, Struct. Bond. (Berlin) 53 (1983) 1–57.
[52] J.J.P. Stewart, J. Comput. Chem. 10 (1989) 209–220.

Talanta 115 (2013) 84–93

Contents lists available at SciVerse ScienceDirect

Talanta

journal homepage: www.elsevier.com/locate/talanta

Development and validation of a general approach to predict and quantify the synergism of anti-cancer drugs using experimental design and artificial neural networks

Tiziana Pivetta [a,*], Francesco Isaia [a], Federica Trudu [a], Alessandra Pani [b], Matteo Manca [b], Daniela Perra [b], Filippo Amato [c], Josef Havel [c,d,e]

[a] Chemical and Geological Sciences Department, University of Cagliari, 09042 Monserrato (CA), Italy
[b] Biomedical Sciences Department, University of Cagliari, 09042 Monserrato (CA), Italy
[c] Department of Chemistry, Faculty of Science, Masaryk University, Kampus Bohunice, Kamenice 5/A14, 62500 Brno, Czech Republic
[d] Department of Physical Electronics, Masaryk University, Kotlářská 2, 611 37 Brno, Czech Republic
[e] R&D Center for Low-cost PLasma and Nanotechnology Surface Modifications, Faculty of Science, Masaryk University, Kotlářská 2, 611 37 Brno, Czech Republic

ARTICLE INFO

Article history:
Received 8 January 2013
Received in revised form
9 April 2013
Accepted 12 April 2013
Available online 18 April 2013

Keywords:
Artificial neural networks
Cancer
Cisplatin
Copper complexes
Experimental design
Synergism

ABSTRACT

The combination of two or more drugs using *multidrug mixtures* is a trend in the treatment of cancer. The goal is to search for a synergistic effect and thereby reduce the required dose and inhibit the development of resistance. An advanced *model-free* approach for data exploration and analysis, based on artificial neural networks (ANN) and experimental design is proposed to predict and quantify the synergism of drugs. The proposed method non-linearly correlates the concentrations of drugs with the cytotoxicity of the mixture, providing the possibility of choosing the optimal drug combination that gives the maximum synergism. The use of ANN allows for the prediction of the cytotoxicity of each combination of drugs in the chosen concentration interval. The method was validated by preparing and experimentally testing the combinations with the predicted highest synergistic effect. In all cases, the data predicted by the network were experimentally confirmed.

The method was applied to several binary mixtures of cisplatin and [Cu(1,10-orthophenanthroline)$_2$(H_2O)](ClO_4)$_2$, Cu(1,10-orthophenanthroline)(H_2O)$_2$(ClO_4)$_2$ or [Cu(1,10-orthophenanthroline)$_2$(imidazolidine-2-thione)](ClO_4)$_2$. The cytotoxicity of the two drugs, alone and in combination, was determined against human acute T-lymphoblastic leukemia cells (CCRF-CEM). For all systems, a synergistic effect was found for selected combinations.

1. Introduction

Nowadays, a trend in the treatment of cancer is to combine the effects of several drugs using *multidrug mixtures* in order to reduce the required dose and to slow the onset of drug resistance. A combination of two or more drugs might show different effects with respect to those of the individual drugs. When no difference occurs, it means that the action of one drug is not influenced by the action of the other drugs, and the global effect is due to their individual activities. Otherwise, when a difference occurs, this can be either negative or positive; in the former case, the drugs act antagonistically, while in the latter synergistically. Then, the definition of the pure additive effect of the combined drugs is the reference point to understand if the biological activity of a multidrug mixture is due to synergism or antagonism. This definition has been proposed and interpreted by various authors [1–7] with different methods to search for synergy. The most common definitions are based on the combination index (CI) or isobologram (IB) methods. In particular, today, CI is the most commonly used method. In our opinion, this approach has limited applicability because it is based on the assumption that the action of the drugs is due only to the inhibition of enzyme kinetics [4]. In fact, a model introduced in 1984 [8] and based on this idea is still proposed for the interpretation of experimental data. However, it is now well-known that in addition to enzymatic inhibition, drug-receptor and non-specific interactions are also involved. Therefore, a modern model should consider the entire complexity of the phenomena occurring within the cell. Cisplatin (**CDDP**) is an example of drug that does not act directly on enzyme kinetics. In fact, it kills cancer cells by binding to their nuclear DNA [9,10], distorting its structure and triggering cellular processes that result in apoptosis [11]. Therefore, experimental data should be analyzed using approaches that are more general than CI or IB.

* Correspondence to: Dipartimento di Scienze Chimiche e Geologiche, Università degli Studi di Cagliari, Cittadella Universitaria, 09042 Monserrato (CA), Italy. Tel./fax: +39 070 675 4473.
E-mail address: tpivetta@unica.it (T. Pivetta).

0039-9140/$ - see front matter © 2013 Elsevier B.V. All rights reserved.
http://dx.doi.org/10.1016/j.talanta.2013.04.031

Models based on the physico-chemical description of the processes occurring in a system are usually called *hard*. However, because of the lack of knowledge on all the possible interactions among drugs and the constituents and/or the biochemical processes involved within the cell, this kind of model is incomplete and therefore limited. In fact, the CI and IB methods are neither able to quantify nor to predict the cytotoxicity of a given combination of studied drugs. Therefore, the features of such models limit their general applicability and sometimes lead to contradictory results. For all these reasons, we suggest a different way of thinking.

Let us consider the concentrations of the drugs in the mixture as *input* variables while cytotoxicity as a response or output one. The values of the response variable for all the possible combinations of the *input* variables form the response surface. The value of the response depends upon all the processes or phenomena that occur in the system and are reflected in the shape of the response surface. Therefore, building a *model* of the response surface means to build a *model* of the whole system's behavior. As a consequence, the response for all the possible values of the input variables can be estimated or *predicted*. The model can be built by *soft* methods which do not require any assumptions. Polynomial fitting, multiple linear regression (MLR) and partial least squares are examples of common *soft* methods. However, several of them suffer of some limitations [12].

Artificial neural networks (ANN) represent a powerful mathematical tool able to accomplish a *learning* process using a set of experimental data (training set) and to generalize this *knowledge* to *predict* the response. Then, the ANN can *understand* the unknown relationship existing among the input and the response variables. The network *learns* by extracting the information hidden in the experimental data of the training set. The choice of the experimental data is crucial for good results, and, for practical reasons, the number of experiments should be as low as possible while providing a high content of information. This can be achieved by using experimental design (ED) techniques [13].

The aim of this work is to: (i) generalize in a rigorous mathematical form the definition of the pure additive effect of an arbitrary number of drugs, (ii) develop an original approach for the evaluation of cytotoxicity data with which to search for the optimal drug combination that gives the maximum synergism and (iii) apply the proposed approach to evaluate the occurrence of synergism in a series of binary mixtures of **CDDP** and three different complexes of copper(II) with 1,10-ortho-phenanthroline (phen) against a human acute T-lymphoblastic leukemia cell line (CCRF-CEM). The chosen complexes, Cu(1,10-orthophenanthroline)$(H_2O)_2(ClO_4)_2$ (**1**), [Cu(1,10-orthophenanthroline)$_2(H_2O)](ClO_4)_2$ (**2**) and [Cu(1,10-orthophenanthroline)$_2$(imidazolidine-2-thione)]$(ClO_4)_2$ (**C1**), show antitumor effects both *in vitro* and *in vivo* [14] and high cytotoxic activity against mouse neuroblastoma, human hematologic and also solid tumor-derived cell lines [15,16]. The proposed approach was validated and tested. The results were achieved using an advanced approach of data exploration and analysis, based on ANN and ED. A comparison with the traditional methods, IB and CI, is also given. The results obtained with the proposed method are compared with those obtained by MLR. The results of the mass spectrometric analysis of the studied mixtures are also given and discussed.

2. Theoretical aspects of the proposed approach

2.1. Generalized definition of additive effect

Starting from the simple definition of the additive effect of two drugs proposed by Webb and Bliss [17,18], we developed a general definition for any number of drugs. The additive effect of drugs is not the algebraic summation of their cytotoxic activities. For this reason, the expression "non-algebraic additive effect" (*NAAE*) will be used in this work in place of "additive effect".

Given n drugs (with $n\geq 2$) with individual percentage of mortality values (number of dead cells with respect to the controls) $a_1, a_2, \ldots, a_n$, (with $a_i\geq 0$), the *NAAE* is expressed for each drug combination in generalized form as:

$$NAAE = \sum_{i=1}^{n} a_i + \sum_{k=2}^{n} \left[(-1)^{k-1} \cdot \frac{C_{n,k}\{a_1, a_2, \ldots, a_n\}}{100^{k-1}} \right] \quad (1)$$

where $C_{n,k}\{a_1, a_2, \ldots, a_n\}$ are the simple combinations without repetition of the cytotoxicity values of the n drugs taken k at a time (with $k\geq 2$). The set of the values given by Eq. (1) has 0% and 100% as the lower and upper limits, respectively, because no mixture of drugs can have an effect greater than 100% and/or lower than 0%. The *NAAE* as expressed by Eq. (1) represents a new operational definition of the additive effect. It is calculated according to a sequential action of the drugs and does not need to be justified on a biochemical basis.

The expanded form of Eq. (1) is given by Eq. (2), where each term in square brackets accounts for $n!/[k!(n-k)!]$ elements.

$$NAAE = \sum_{i=1}^{n} a_i - \frac{1}{100}\left[\sum_{i\neq j} a_i a_j\right] + \frac{1}{100^2}\left[\sum_{i\neq j\neq l} a_i a_j a_l\right] - \ldots + (-1)^{k-1} \cdot \frac{1}{100^{n-1}}\left[\prod a_i\right] \quad (2)$$

For two drugs, Eq. (2) assumes the same form (Eq. (3)) of the equation proposed by Webb and Bliss [17,18].

$$NAAE = a_1 + a_2 - \frac{a_1 a_2}{100} \quad (3)$$

For three drugs, Eq. (2) becomes Eq. (4).

$$NAAE = a_1 + a_2 + a_3 - \frac{a_1 a_2 + a_1 a_3 + a_2 a_3}{100} + \frac{a_1 a_2 a_3}{100^2} \quad (4)$$

The definition of *NAAE* given by Eq. (1) is the reference point which allows us to define the occurrence of synergism or antagonism of drugs. This is done by calculating the net multi-drug effect index (*NMDEI*) as in Eq. (5), where $E_{exp.}$ is the experimental antiproliferative effect of a given drug combination.

$$NMDEI = E_{exp.} - NAAE \quad (5)$$

NMDEI gives a quantitative account of the net multidrug effect and can assume either positive or negative values that indicate synergism or antagonism, respectively. When *NMDEI* is equal to zero, then the experimental activity of the multidrug mixture is equal to *NAAE* (Eq. (5)). Since the cytotoxic activity of an individual drug and/or that of a drug combination is expressed as a percentage, *NAAE* and *NMDEI* are also expressed as a percentage.

Using the proposed ED–ANN combined approach, the cytotoxicity of individual drugs and that of their combinations at concentrations not experimentally tested can be predicted on the whole working space using a grid with desired dimensions. The values estimated for each point of the chosen grid in place of the experimental values ($E_{exp.}$) can be used in Eq. (5). The cytotoxicity values of individual drugs (a_i) estimated by the network compose their related dose–response curves. Using such curves, the *NAAE* can be calculated for each point of the grid. Then, the *NMDEI* can be calculated according to Eq. (5) for each point of the chosen grid.

2.2. Artificial neural networks

An ANN is a formal object that emulates the structure of the brain and its *learning* ability [13]. A series of logic units, called *neurons*, is organized in layers: input, hidden and output. An

example of the ANN architecture used in this work is given in the supplementary materials (Fig. S1).

As for the biological brain, an ANN needs to be trained before it can be used for *prediction*. This is done using a *training set* formed by known input-response data. The inputs are iteratively processed by the network according to a suitable *training algorithm* in order to estimate the actual output of the training set. Several algorithms are available [19], for example standard back-propagation [20], R-propagation [21] and quick-propagation [22]. The root mean square error (*RMSE*) is calculated according to Eq. (6), where N, M, o_{pk}, and $o_{pk}^{(*)}$ are the number of experiments used for training, the number of response variables, the estimated and the actual output value, respectively.

$$RMSE = \sqrt{\frac{\sum_{p=1}^{N}\sum_{k=1}^{M}(o_{pk} - o_{pk}^{*})^2}{N \times M}} \quad (6)$$

The available data set is usually divided into three subsets: (i) training, (ii) verification and (iii) the test set. The verification set is used during training to monitor the generalization ability of the network. Training is stopped when the minimum *RMSE* for the verification set is reached. Once the network is trained and verified, it should be validated. This is done in the so-called *test step* by comparing the estimated and experimental response for selected input data.

2.3. Response surface and experimental design

The *working space* is the plane delimited by the minimum and maximum values of the chosen variables. For example, let us consider the concentration of drug A (C_A) as the x-axis, while that of drug B (C_B) as the y-axis. Supposing $p \le C_A \le q$ and $r \le C_B \le s$, the working space is given by all the points w belonging to the set W defined by Eq. (7).

$$W = \{w / w = (C_A, C_B) \in R / p \le C_A \le q \wedge r \le C_B \le s\} \quad (7)$$

Therefore, each point w belonging to W represents the conditions of one experiment. The response variable z (e.g. cytotoxicity) is a function of the chosen C_A and C_B variables (Eq. (8)).

$$z = f(w) = f(C_A, C_B) \quad (8)$$

The set Z given by Eq. (9) defines the *response surface*.

$$Z = \{z / z = f(w), w \in W\} \quad (9)$$

The aim of *hard* modeling is finding out the analytical expression of the function f according to a rigorous physical description of the studied system. However, f is often very complex or even unknown. Therefore, the function f can be approximated employing *soft* modeling. Each point w provides information about the function f. A greater number of experiments is associated with a better model. However, the duration and the cost of the experiments are often crucial. Then, a compromise to obtain an acceptable model with the lowest number of experiments is needed. ED is a chemometrical tool used to distribute n experiments on the working space in such a way that the information content for that n is the highest [23]. For the study of drug combinations, as a first approach, the concentrations of the drugs should be chosen in the range within 0 and twice the CC_{50} (the dose of the drug which inhibits 50% of cell proliferation). Therefore, knowledge of a simple estimation of CC_{50} is needed.

For the evaluation of the cytotoxic activity of two or more drugs, the following information is necessary:

- a sufficient number of experiments to model the dose–response curve of each drug;
- a sufficient number of experiments distributed in the studied space to model the cytotoxicity response surface.

Due to the assay techniques of the cytotoxic activity, a non-symmetrical experimental design was used here. However, the lack of symmetry of the experimental design does not affect the performance of the chosen method that has been shown to properly describe the studied systems.

The chosen experimental designs are shown in Fig. 1a, c and e. The points used in the training, validation and test sets are highlighted in Figs. 1–4 and S3–S6.

2.4. Structure of the proposed approach

The proposed ED–ANN approach consists of the following steps:

(1) Set-up of the ED.
(2) Experimental determination of the cytotoxicity of the drugs alone and those of the multidrug mixtures prepared according to the chosen ED.
(3) Training and verification of the artificial neural network.
(4) Prediction of the response using the network, according to a suitable grid that covers the entire working space.
(5) Calculation of the *NAAE* for each point of the grid.
(6) Calculation and plot as a function of the drug concentrations of *NMDEI* (*NMDEI* surface).
(7) Testing the obtained results.

3. Materials and methods

3.1. Reagents

Copper(II) carbonate basic ($Cu_2(CO_3)(OH)_2$), 1,10-phenanthroline monohydrate, cisplatin (**CDDP**), perchloric acid, ethanol, ethyl ether, dimethyl sulfoxide (DMSO), imidazolidine-2-thione, 3-hydroxy picolinic acid, acetonitrile (CH_3CN), trypan blue and 6-mercaptopurine were purchased from Sigma-Aldrich (Milan, Italy) and used without any further purification. Fetal calf serum (FCS), penicillin G sodium and streptomycin sulfate were purchased from Gibco-Invitrogen (Milan, Italy) and used without any further purification. Red phosphorus was purchased from Riedel de Haën (Hannover, Germany). Water was double distilled from a quartz apparatus from Heraeus Quarzschmelze (Hanau, Germany).

3.2. Synthesis

The compounds **1**, **2** and **C1** were prepared as previously reported [15,16]. Briefly, copper perchlorate was prepared *in situ* by the reaction of $Cu_2(CO_3)_2(OH)_2$ with $HClO_4$ in a 1:2 M ratio in ethanol solution; phen was added in a Cu(II):phen molar ratio of 1:1 or 1:2 to obtain **1** or **2**, respectively. **C1** was prepared by the reaction of **2** and imidazolidine-2-thione in a 1:1 M ratio in CH_3CN solution.

3.3. Cell lines

The CCRF-CEM (acute T-lymphoblastic leukemia) human cell line was purchased from the American Type Culture Collection (ATCC-LGC; Milan, Italy). The cell line was grown at 37 °C in a 5% CO_2 atmosphere in RPMI 1640 medium according to instructions from ATCC in the presence of 10% FCS, 100 U/mL penicillin and 100 μg/mL streptomycin. The cell line was maintained in

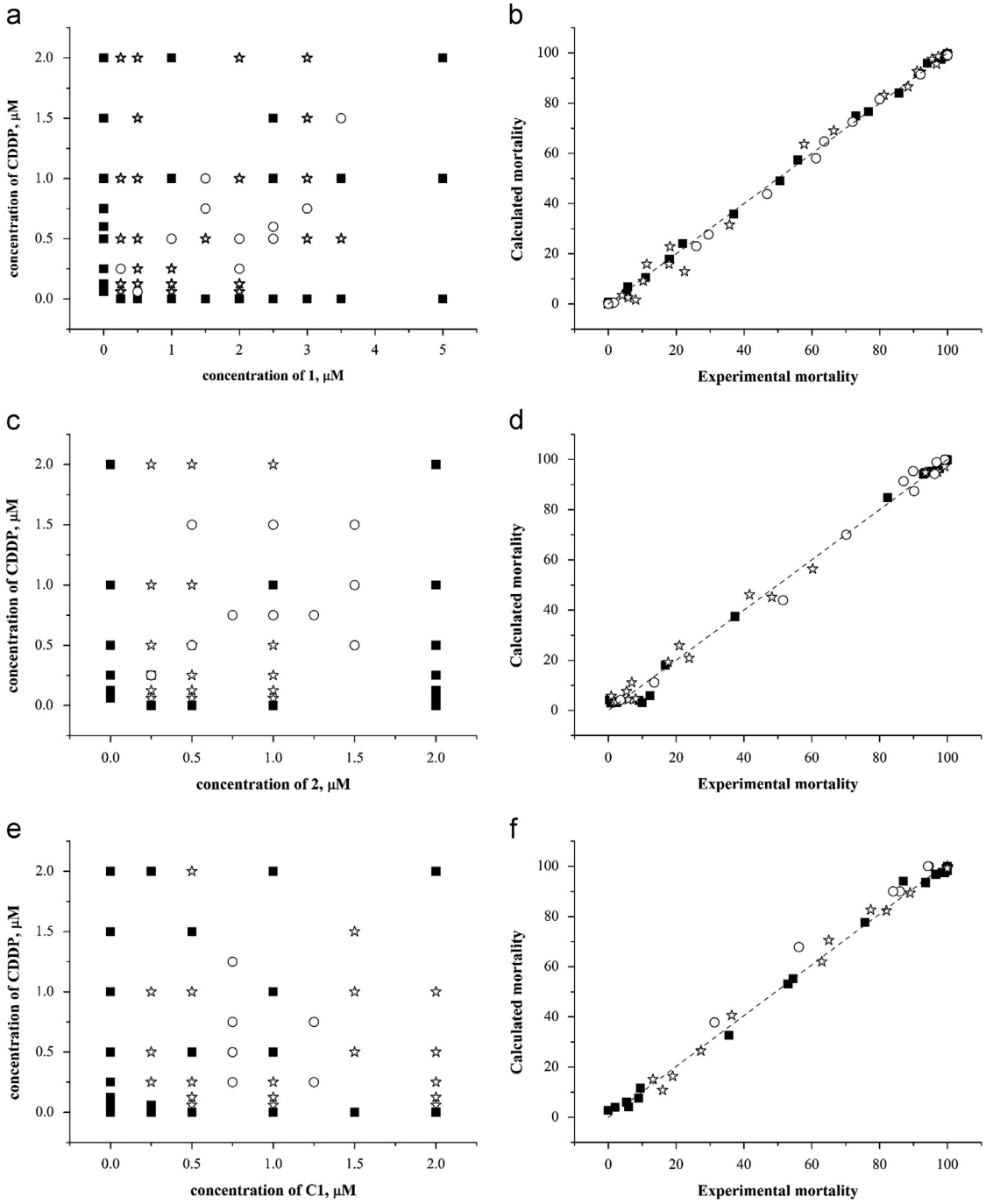

Fig. 1. Experimental design (■ training set, ☆ validation set and ○ test set) for the systems (a) **1-CDDP**, (c) **2-CDDP** and (e) **C1-CDDP**; comparison between experimental (■ training set, ☆ validation set and ○ test set) and calculated mortality values for the systems (b) **1-CDDP**, (d) **2-CDDP** and (f) **C1-CDDP** (linear fitting parameters for the equation $y=mX$ are $m=0.999(3)$ with $r=0.9999$ for the training set, $m=1.00(1)$ and $r=0.9986$ for the validation set, $m=0.990(1)$ and $r=0.9995$ for the test set, $m=1.00(1)$ and $r=0.9993$ for all the data values for **1-CDDP**; $m=1.00(1)$ with $r=0.9991$ for the training set, $m=0.99(1)$ and $r=0.9978$ for the validation set, $m=1.00(1)$ and $r=0.9988$ for the test set, $m=1.00(1)$ and $r=0.9988$ for all the data values for **2-CDDP**; $m=1.00(1)$ with $r=0.9991$ for the training set, $m=1.00(1)$ and $r=0.9995$ for the validation set, $m=1.08(2)$ and $r=0.9977$ for the test set, $m=1.02(1)$ and $r=0.9988$ for all the data values for **C1-CDDP**.

exponential growth by periodically splitting high density suspension cultures (*i.e.* 10^6/mL). The cell culture was periodically tested for the absence of mycoplasma contamination.

3.4. Cytotoxic assay

The cytotoxic effect of test compounds was evaluated in exponentially growing cell cultures. Stock solutions of test compounds were made at 1 mM in DMSO and stored at 4 °C in the dark. For the evaluation of cytotoxicity, each compound was serially diluted in specific growth medium so that the concentration of DMSO was never higher than 0.1%. Cell growth in the absence and in the presence of the test compounds was determined after 96 h of incubation, corresponding to three duplication rounds of untreated cells, by the 3-(4,5-dimethylthiazol-2-yl)-2,5-diphenyl-tetrazolium bromide (MTT) method [24]. Numbers of viable cells were also determined by the trypan blue dye exclusion method. Cell growth at each drug concentration was expressed as the percentage of untreated controls. Each compound was tested in at least three independent assays. Statistical analysis was

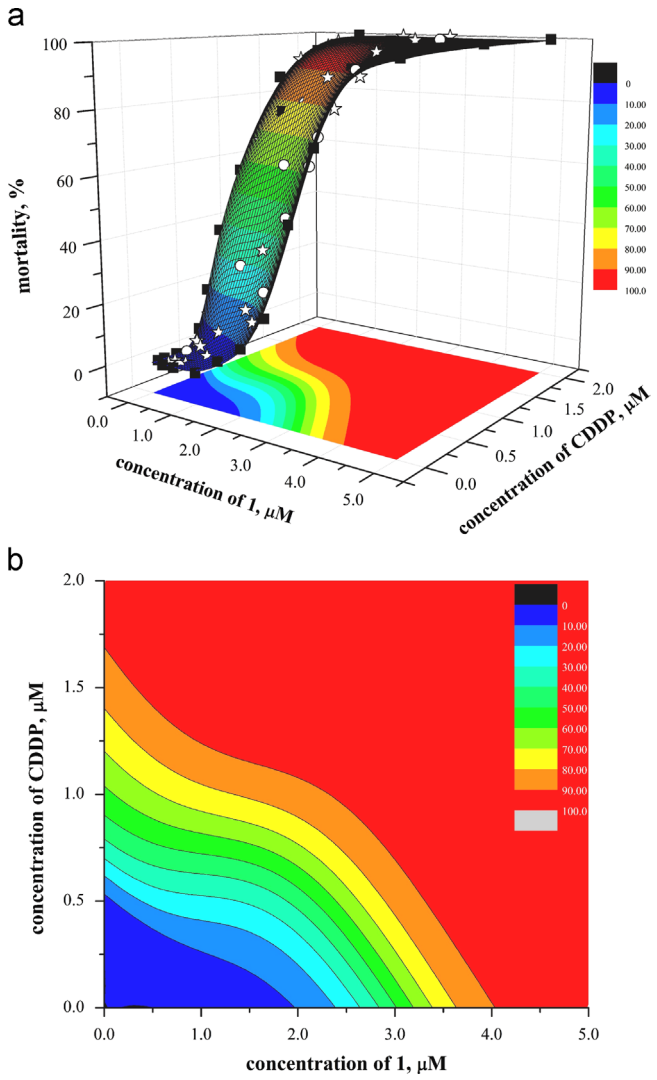

Fig. 2. Response surface with experimental data (■ training set, ☆ validation set and ○ test set) (a) and contour plot of cytotoxicity iso-values (b) for the system **1**-**CDDP**.

performed with Student's t-test, and significance was set at $p \leq 0.05$. The antitumor agent 6-mercaptopurine was used as a reference compound. Because of the variability in cell reactivity (correlated to the growing time and the final density of the suspension cultures) slight differences were observed in the cytotoxicity values of **CDDP** obtained in these experiments.

3.5. Mass spectrometry

Mass spectra were recorded using AXIMA Resonance mass spectrometer from Kratos Analytical (Manchester, UK), equipped with a quadruple ion trap (QIT) and a reflectron time-of-flight analyzer (RTOF). The instrument for drying samples was from Kratos Analytical. Calibration was done using red phosphorus clusters as described in [25].

Laser desorption ionization (LDI) and matrix-assisted laser-desorption ionization (MALDI) were used. From several matrices examined, 3-hydroxo picolinic acid was found to be the most suitable. It was found that all the species detected both in LDI and MALDI analyses were singly charged. The mixtures of **1**, **2** and **C1** complexes with **CDDP** (5:1 molar ratio) were prepared in 50% acetonitrile/water. For LDI analysis, 5 μL of the mixture were deposited on the metallic target of the instrument and, after drying, the mass spectra were recorded. For MALDI analysis, first 5 μL of saturated solution of matrix were deposited and, after drying, 5 μL of the mixture were deposited on the matrix layer and dried again.

Mass spectra were recorded in both reflectron positive and negative ion mode after the pressure was below 10^{-4} Torr. Mass spectra recorded in negative ion mode were found to be not suitable, therefore only mass spectra recorded in positive ion mode were used.

3.6. Software

ANN computation was performed using the Trajan Neural Network Simulator (release 3.0 D, Trajan Software, Horncastle, UK) and EasyNN-plus (Neural Planner Software Ltd, Cheadle Hulme, UK) programs. All computations were performed on a standard PC computer with Microsoft Windows XP Professional as operating system. Other mathematical calculations were done using GNU Octave ver. 3.2.4 (Free Software Foundation, Inc. http://fsf.org/) configured for i686-pc-linux-gnu on a standard PC x86 running Ubuntu Linux ver. 12.04.

4. Results and discussion

4.1. Set up of the ED

For each binary mixture, the experimental design was built choosing the concentration interval of the drugs in the range 0 −~2 × CC_{50}. Following the experimental design reported in Fig. 1a, 42 combinations of **1** and **CDDP**, nine solutions of **CDDP** alone and nine solutions of **1** alone were prepared. Among the 60 solutions, 25 were used as the training set, 24 as the validating set and 11 as the test set. Following the experimental design reported in Fig. 1c, 34 combinations of **2** and **CDDP**, six solutions of **CDDP** alone and four solutions of **2** alone were prepared. Among the 44 solutions, 18 were used as the training set, 16 as the validating set and 10 as the test set. Following the experimental design reported in Fig. 1e, 33 combinations of **C1** and **CDDP**, seven solutions of **CDDP** alone and five solutions of **C1** alone were prepared. Among the 46 solutions, 21 were used as the training set, 19 as the validating set and six as the test set. The test sets for all the systems were chosen after the inspection of the results obtained by the network.

4.2. Experimental determination of the cytotoxicity of individual drugs and multidrug mixtures prepared according to the chosen ED

Three different sets of experiments were carried out, each one in three replicates, for the **1**-**CDDP**, **2**-**CDDP** and **C1**-**CDDP** combinations. The concentration of **1** was in the range of 0–5 μM, while the concentrations of **2**, **C1** and **CDDP** were in the range of 0–2 μM. The vitality (% of living cells) after the treatment with the drugs was measured for each solution with respect to the control (untreated cells) and converted into mortality (100% minus vitality).

4.3. Training and verification of the artificial neural network

The concentrations of the drugs and the experimental cytotoxicity values were used as the input and output data. As the training algorithm, standard back-propagation [20] was used.

At first, the optimal neural network architecture was searched for using the criteria of lowest *RMSE*. The number of hidden layers and the number of neurons therein were investigated. The value of *RMSE* for the training and verification sets were plotted against the number of neurons in the hidden layers. The optimal number of

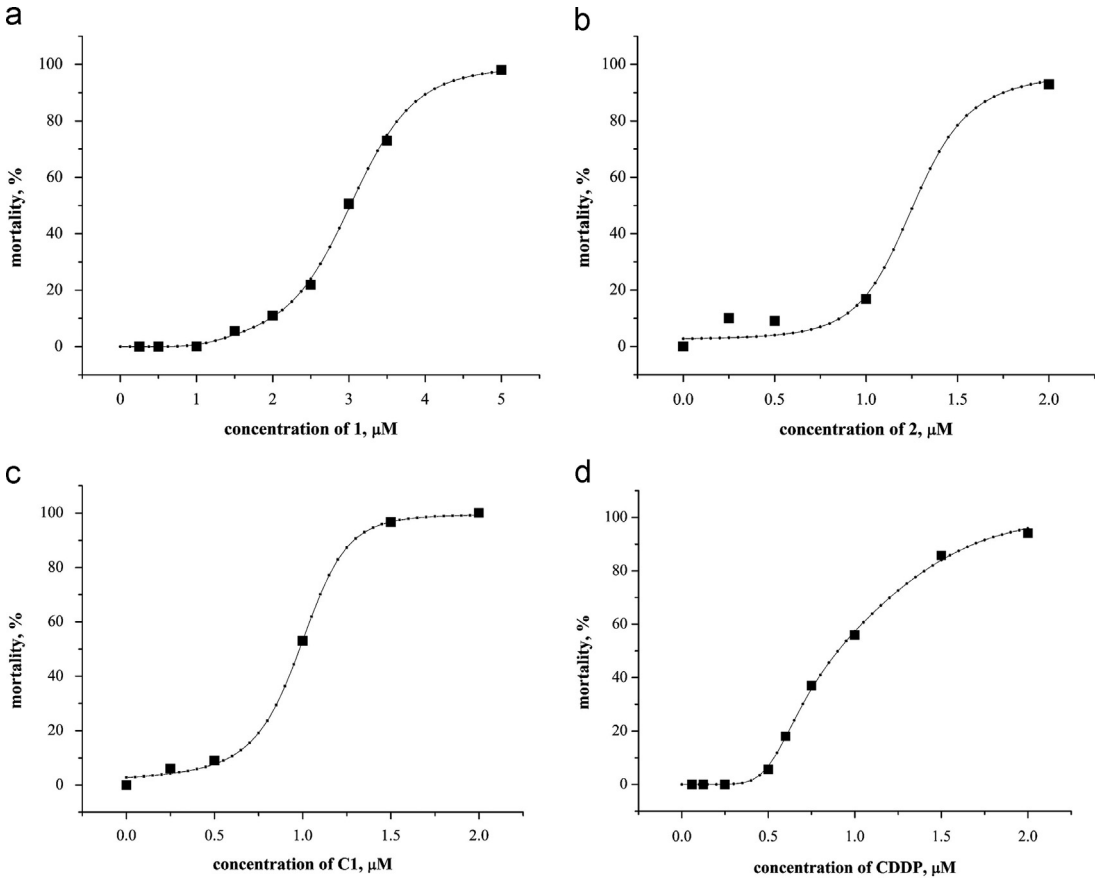

Fig. 3. Calculated (-●-) and experimental (■) dose–response data for (a) **1**, (b) **2**, (c) **C1** and (d) **CDDP** against the CCRF-CEM cell line.

neurons is found when the minimum *RMSE* for the verification set is reached. It was found that a three-layer structure, *i.e.* one input, one hidden and one output, with four (for **1-CDDP** and **C1-CDDP**) or five (for **2-CDDP**) neurons in the hidden layer was sufficient. The network's parameters were re-initialized several times, randomly changing their initial values to prove the robustness of the model and the reproducibility of the results. The resulting architecture of the network for the **C1-CDDP** system is shown in Fig. S1 as an example.

For each system, the network was trained and verified using the proper training and validation sets. All points lying on the borders of the experimental design were included in the training set. Validation points were chosen randomly on the working space. The training was stopped when the minimum *RMSE* for verification step was reached (the plot of *RMSE vs*. number of epochs for the system **1-CDDP** is shown as an example in Fig. S2). The agreement between the values calculated by the network and the experimental ones is shown in Fig. 1b, d, f, where the calculated and experimental data are plotted against each other.

Once trained and verified, the network was used to predict the cytotoxicity on the whole working space according to a grid with dimensions 40×40.

4.4. Exploring the response surface

The plot of the calculated cytotoxicity values as a function of the concentration of the drugs represents the response surface. The response surface and related contour plot for **1-CDDP** system is shown in Fig. 2. The results for **2-CDDP** and **C1-CDDP** systems are shown in Figs. S3 and S4. The mortality of the mixtures increases proportionally with the concentrations of the two drugs (Fig. 2a, S3a and S4a). The resulting surface shows similar trend to that of the dose–response curve.

Using the contour plot (Fig. 2b, S3b and S4b), the areas of cytotoxicity iso-values for the various mixtures can be explored. In this way, the mixture with the desired cytotoxicity and the related lowest dose of both drugs can be found. In fact, for a toxicity of 70%, instead of choosing **1** alone at a concentration of ≈3.5 μM, **2** alone at ≈1.5 μM, **C1** alone at ≈1.4 μM or **CDDP** alone at a ≈1.2 μM, it is possible to select appropriate combinations such as:

- **1** at 2.0 μM and **CDDP** at 0.78 μM (Fig. 2b)
- **2** at 0.9 μM and **CDDP** at 0.95 μM (Fig. S3b)
- **C1** at 0.65 μM and **CDDP** at 0.60 μM (Fig. S4b)

For a toxicity of 50%, instead of choosing **1** alone at a concentration of ≈3 μM, **2** alone at ≈1.25 μM, **C1** alone at ≈1 μM or **CDDP** alone at ≈1 μM, it is possible to select:

- **1** at 1.88 μM and **CDDP** at 0.60 μM (Fig. 2b)
- **2** at 0.75 μM and **CDDP** at 0.80 μM (Fig. S3b)
- **C1** at 0.50 μM and **CDDP** at 0.45 μM (Fig. S4b).

The use of a lower concentration of each drug minimizes the side effects related to the doses. The reliability of the network and of the obtained results is shown by the good agreement between the calculated and experimental values, as can be seen in Fig. 2a, S3a and S4a, where the experimental points are superimposed on the calculated surfaces.

From the calculated cytotoxicity values of the bottom and left borders of the ED (*i.e.* for a single drug at time) the dose–response curves for **1**, **2**, **C1** and **CDDP** is obtained. In Fig. 3a–d, the calculated curves are shown together with the experimental

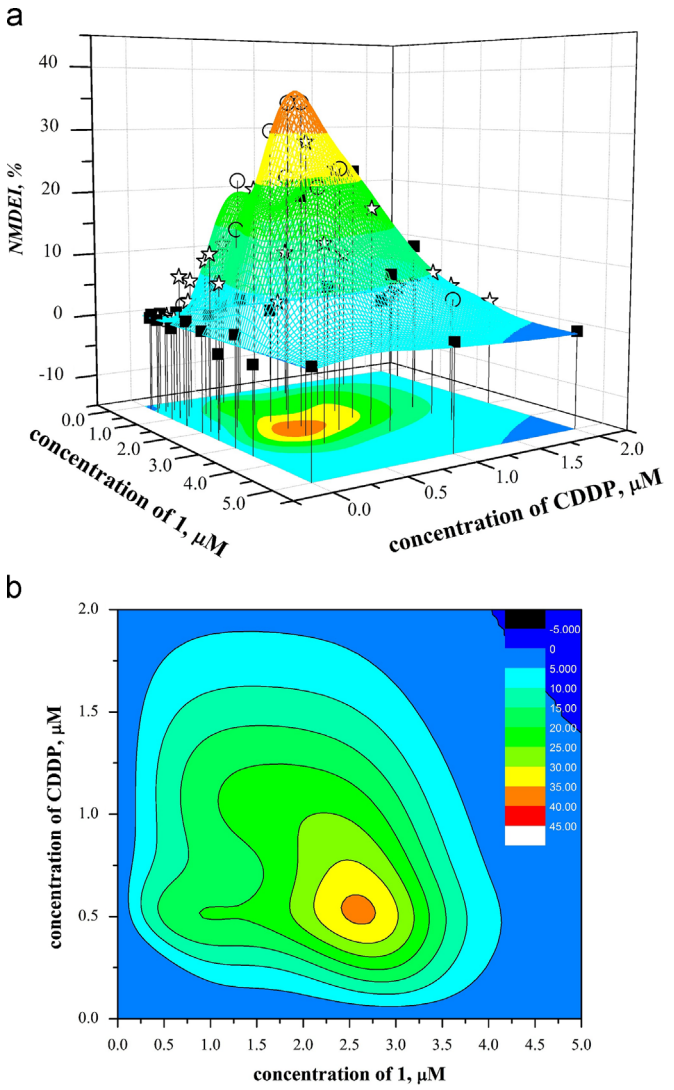

Fig. 4. *NMDEI* surface with experimental data (■ training set, ☆ validation set and ○ test set) (a) and contour plot of *NMDEI* iso-values (b) for the system **1-CDDP**.

points. For **1**, **2** and **C1**, a sigmoidal curve was obtained. The threshold doses (the minimum dose at which the drug presents an effect) for **1**, **2**, **C1** and **CDDP** are 1 μM, 0.5 μM, 0.25 μM and 0.375 μM, respectively. The calculated CC_{50} values are in the order: **CDDP** (0.922 μM)<**C1**(0.989 μM)<**2**(1.26 μM)⩽**1** (3.01 μM).

4.5. Calculation of the NAAE and the NMDEI surface

The *NAAE* was calculated according to Eq. (1) and subtracted from the cytotoxicity values for all the points of the used grid to determine the *NMDEI* (Eq. (5)). The plot of the *NMDEI* as a function of the drug concentrations and the related contour plot is shown in Fig. 4 for **1-CDDP** system. The results for **2-CDDP** and **C1-CDDP** systems are shown in Figs. S5 and S6. Only positive values of *NMDEI* are present for the **1-CDDP** system (Fig. 4a), indicating a synergistic effect between the two drugs. The maximum *NMDEI* is present at a concentration of **1** equal to 2.63 μM and a concentration of **CDDP** equal to 0.55 μM (Fig. 4b). As can be seen from Fig. 2b, this combination induces 73.6% mortality, while **1** and **CDDP** alone show at the same concentrations as the combination mortality values of 29.3 and 11.8%, respectively. The same considerations can be done for the systems **2-CDDP** and **C1-CDDP**. In fact, the maximum *NMDEI* indicating a synergistic effect is revealed (Fig. S5a, S5b) at **2** equal to 1.05 μM and **CDDP** equal to 0.85 μM. This combination induces 81.6% cytotoxicity (Fig. S3), while **2** and **CDDP** alone show at the same concentrations as the combination cytotoxicity values of 19.7% and 18.5%, respectively. For the **C1-CDDP** system (Figs. S6a and S6b), a maximum is revealed at **C1** equal to 0.87 μM and **CDDP** equal to 0.45 μM. This combination induces 82.8% cytotoxicity (Fig. S4), while **C1** and **CDDP** alone show at the same concentrations as the combination cytotoxicity values of 32.9% and 27.5%, respectively.

No negative values of *NMDEI* are present in any case, indicating that **CDDP** and the studied copper(II) complexes do not act antagonistically in the studied range of concentrations.

4.6. Test of the obtained result

In order to confirm the predicted maxima of *NMDEI* and to check the overall predictive ability of the network, new sets of 11 combinations of **1-CDDP**, 10 combinations of **2-CDDP** and six combinations of **C1-CDDP** were prepared (test sets) and the corresponding cytotoxic activities were measured. These test data values were corrected for the *NAAE* and compared with the calculated values. It was found that all the data predicted by the network were experimentally confirmed. The test points are superimposed to the surfaces in Figs. 1, 2, 4 and S3–S6. The quality of the prediction can also be seen from Fig. 1b, d and f ("o" symbol).

4.7. Mass spectrometry

Since the highest values of *NMDEI* occurs for almost integer ratios of copper complexes and **CDDP** concentrations (5:1, 1:1 and 1:2 Cu(II)/**CDDP** for **1**, **2** and **C1**, respectively), we verified the possible formation of mixed complexes between either **1**, **2** or **C1** with **CDDP** by mass spectrometry. Both the LDI and MALDI mass spectra of the mixtures of Cu(II) complexes and **CDDP** at 1:5 and 5:1 molar ratios were recorded. No mixed copper-platinum complexes were detected (mass spectra are not shown).

4.8. Comparison with IB and CI methods

4.8.1. Brief description of the methods

The IB method [5] consists of the construction of a graph in which equally effective doses of two drugs are reported for a single effect level (isoboles). Once a specific level is chosen, such as 50% of the maximum, the doses of the two drugs A and B that give the same degree of effect are plotted as axial points in a Cartesian plot. The straight line connecting A and B defines the combinations that produce a pure additive effect. The experimental points which fall below or above that line represent drug combinations that have synergistic or antagonistic effect, respectively.

The CI method [3,4,6,7] tries to measure the extent of drug interactions. It considers the existence of a relationship between the fraction affected (f_a) and unaffected ($1-f_a$) by a drug and the ratio $(D/D_m)^m$, according to Eq. (10), where D is the dose of the drug and D_m is the median effect dose, *i.e.* the concentration at which the drug inhibits the system by 50% (the fraction affected (f) coincides with the cytotoxic activity divided by 100).

$$\frac{f_a}{(1-f_a)} = \left(\frac{D}{D_m}\right)^m \tag{10}$$

The values of m and D_m are determined by applying a logarithm to Eq. (10), which gives $log\ (f_a/(1-f_a)) = m\ log\ (D) - m\ log\ (D_m)$ and plotting the function $y = log\ (f_a/(1-f_a))$ *vs.* $x = log\ (D)$. By linear fitting, the variables m and D_m can be obtained as the slope and intercept, respectively.

Once m and D_m are defined, as the second step of the method, the value of D_x for each drug (Eq. (11)) and finally the *CI* (Eq. (12)) have to be calculated (the numbers 1 and 2 indicate the two

drugs).

$$D_x = D_m\left(\frac{f_a}{1-f_a}\right)^{1/m} \quad (11)$$

$$CI = \frac{D^1}{D_x^1} + \frac{D^2}{D_x^2} \quad (12)$$

A *CI* lower than, equal to and higher than 1 indicates synergism, additivity and antagonism, respectively.

4.8.2. Selected examples

Both CI and IB methods require that the concentrations of the individual drugs and that of their combinations providing the same cytotoxic effect have to be compared. Let us consider the solutions reported in Table 1. In the solutions *a* and *b*, **CDDP** and **1** have a concentration of 1.0 and 3.0 μM, respectively; at these concentrations, they both show a cytotoxicity value of 50%. Following the IB and CI methods, these two solutions should be compared with all the combinations which show the same cytotoxic activity, for example solution *c*. On the basis of the results of the isobologram (Fig. S7a, triangle symbol and dotted line) and of *CI* calculus (*CI*=1.28), this combination presents antagonistic effect. Instead, in our view, the final effect of a combination should be compared with the effects that the individual drugs provide at the same concentration. In fact, solution *c* should be compared with *d* and *e*, *i.e.* where **1** and **CDDP** have the same concentration of their combination. The drugs **1** and **CDDP** alone present a cytotoxicity value of 9% and 18%, respectively. Comparing these two values with the cytotoxicity of their combination (50%), a clear synergistic effect is evident, as also pointed out by the *NMDEI* calculated by our approach, being positive and higher than zero (*NMDEI*=25).

To stress the concept, we can consider the solutions *f*, *g* and *h*. If we compare the cytotoxic activity of **1** at the concentration of 2.63 μM, which is equal to 29%, and that of **CDDP** at a concentration of 0.55 μM, which is equal to 12%, it appears evident that the cytotoxic activity of their combination (74%) is even greater than a simple algebraic sum of the effects, and, without any kind of calculation, a synergistic effect is evident. The *CI* (*CI*=1.23) instead suggests an antagonistic effect. Note that solution *f* has the maximum value of *NMDEI* (*NMDEI*=36, Fig. 4).

The same considerations may be presented for the **2-CDDP** (solutions *i*–*n*) and **C1-CDDP** systems (solutions *o*-*u*). In particular, the solutions *l* and *s* that give rise to the maximum value of *NMDEI* for the **2-CDDP** and **C1-CDDP** systems, respectively, present a *CI* indicating an additive effect (*CI*=0.98) or a weak synergistic effect (*CI*=0.88).

Let us now analyze some other results reported in the literature for the system **CDDP**-paclitaxel [6] on 833 K teratocarcinoma cells. Considering the solutions *aa*, *ab* and *ac*, we find that the cytotoxic activity of paclitaxel at 0.01 μM is 88%, that of **CDDP** at 1.0 μM is 82%, while their combination has a cytotoxic activity of 97%. According to the *CI*, this combination has a synergistic effect (*CI*=0.602), but, applying our method, we find that the *NMDEI* for the two drugs is equal to −1%; therefore, a slight antagonistic rather than synergistic effect should be considered. Let us now analyze the solutions *ad*, *ae* and *af*; the compounds paclitaxel at 0.002 μM and **CDDP** at 0.2 μM present a cytotoxicity value of 43% and 30%, respectively, while their combination has a cytotoxicity value of 70%. According to the *CI*, this combination has a moderate synergistic effect (*CI*=0.815), lower than that shown by the solution *ac*, as it is closer to 1. According to our calculation, the *NMDEI* of this combination is 10%, indicating a synergistic effect, unlike the previous case.

Table 1
Results for selected experimental data analyzed using the method proposed in this work and the combination index (*CI*).

System	Solution	Conc. of drug$_1$ (μM)	Conc. of CDDP (μM)	Experimental cytotoxicity (%)	*NMDEI (%)*[a]	*CI.I.*[b]
CDDP	***a***		1.0	50		
1-CDDP	***b***	3.00	–	50	–	–
	c	1.88	0.60	50	25	1.28
	d	1.88	–	9	–	–
	e	–	0.60	18	–	–
	f	2.63	0.55	74	36	1.23
	g	2.63		29	–	–
	h		0.55	12	–	–
2-CDDP	***i***	1.25		50	–	–
	j	0.75	0.80	50	29	1.50
	k	0.75		7	–	–
	l	1.05	0.85	82	44	0.98
	m	1.05		20	–	–
	n		0.85	19	–	–
C1-CDDP	***o***	0.98	–	50	–	–
	p	0.50	0.45	50	16	1.40
	q	–	0.45	28	–	–
	r	0.50	–	8	–	–
	s	0.87	0.45	83	33	0.88
	t	0.87		32	–	–
	u		0.45	28	–	–
PAC-CDDP[c]	***aa***	0.01	–	88	–	–
	ab		1.0	82	–	–
	ac	0.01	1.0	97	−1	0.602
	ad	0.002	–	43	–	–
	ae	–	0.2	30	–	–
	af	0.002	0.2	70	10	0.815

[a] Calculated by Eq. (5).
[b] Calculated as proposed by Chou [6] (a number greater, lower or equal to 1, indicates antagonism, synergism and additive effect, respectively).
[c] PAC is paclitaxel [6].

4.8.3. Our considerations

In our opinion, comparing the concentrations of individual drugs and that of their combination providing the same cytotoxic effect, as the CI and IB methods suggest, might lead to misleading results. A better comprehension of the studied system arises from a comparison between the effect of a given combination and the effect that the individual drugs provide at the same concentration.

The CI method tries to explain the cytotoxic effect of drug mixtures considering the inhibition of enzymatic activity, a mechanism that follows an exponential trend. In our opinion, this is actually a limitation. If the mechanism of drug action is not due only to the inhibition of enzymatic kinetics, then linearizing a pattern which is not *a priori* exponential leads to approximate results. In fact, the application of the logarithm mathematical operator to linearize a function is justified only when the trend of the function is exponential over its entire interval of existence. The common choice to consider only the points that lie on a portion of a straight line, *i.e.* those that lie around the inflection point on the dose–response curve, is not mathematically rigorous and shows even more the inability of the method to generalize. The limits of the method are clearly understandable from Fig. S7b–d, where the data of **1** and **CDDP** and paclitaxel alone are reported treated following Eq. (11). As can be seen, the linear fitting of the trend does not give acceptable results, in particular for **1** and **CDDP**.

4.8.4. The choice of the combinations

According to Chou [6,7], the most efficient and economical way to study the combinations of the drugs in order to save data points, costs and time is to keep the ratio of the concentrations constant. In our opinion, this procedure is hazardous because some drug combinations that may exhibit synergism could be lost. In fact, synergism (as well as antagonism) may be due to chemical or bio-chemical reactions (formation of adducts, complexes, redox reactions, ligand/metal exchange, *etc.*) that depend on the experimental conditions, for example the molar ratio. Therefore, by working at a constant molar ratio, the optimal combinations of the drugs might go unnoticed. On the contrary, our method based on the combined approach of ED and ANN, allows the evaluation of all the possible combinations on the entire space defined by the selected concentration intervals.

4.9. Multiple linear regression

As stated in the introduction, the response surface is usually modeled using MLR methods. These were applied to model the cytotoxicity response surface and in this section the results are given. For MLR treatment, the same data used to train the network (Section 4.1) were used.

Polynomials with the general expression shown in Eq. (13) were used.

$$y = \alpha_0 + \sum_{i=1}^{n} \alpha_i x_1^i + \sum_{i=1}^{n} \beta_i x_2^i + \sum_{i=1}^{n}\sum_{j=1}^{n}\sum_{k=1}^{n\times n} \gamma_k x_1^i x_2^j \quad (13)$$

At first, the concentrations of the two drugs could be considered uncorrelated to each other. However, because the possible synergistic or antagonistic effect may be due to a chemical or biochemical reaction between the drugs, the concentrations of the drugs are actually related. In fact, models without the interaction terms ($x_1^i x_2^j$) provided non-acceptable regression parameters (confidence lower than 80%).

A third degree polynomial was used for the system **2-CDDP** and a fourth degree polynomial for the systems **1-CDDP** and **C1-CDDP** (confidence ≥ 95%). Polynomials with a degree higher than four or lower than two gave unreliable results (confidence ≤ 60%). The models obtained for the studied systems are given below (***y*** is the percentage of mortality, $\boldsymbol{x_1}$ and $\boldsymbol{x_2}$ are the concentrations of the two drugs and *RSS* is the residual sum of squares):

- ***System* 1-CDDP**:

$$y = -0.9x_1^4 + 2.9x_1^3x_2 + 6.1x_1^2x_2^2 - 2.4x_1x_2^3 + 31.8x_2^4 + 5.6x_1^3 - 33.4x_1^2x_2 - 22.0x_1x_2^2 - 168.4x_2^3 - 0.659x_1^2 + 78.3x_1x_2 + 276.5x_1^2 - 10.8x_1 - 89.1x_2 + 5.1;\ RSS = 141.$$

- ***System* 2-CDDP**:

$$y = 10.4x_1^3 - 43.2x_1^2x_2 - 9.4x_1x_2^2 - 16.3x_2^3 + 0.5x_1^2 + 83.0x_1x_2 + 61.7x_2^2 + 4.7x_1 - 12.6x_2 + 2.9;\ RSS = 189.$$

- ***System* C1-CDDP**:

$$y = -16.6x_1^4 + 20.9x_1^3x_2 + 36.0x_1^2x_2^2 + 39.0x_1x_2^3 + 28.1x_2^4 + 19.0x_1^3 - 134.4x_1^2x_2 - 151.6x_1x_2^2 - 129.4x_2^3 + 58.1x_1^2 + 164.4x_1x_2 + 164.9x_2^2 - 9.5x_1 + 11.3x_2 + 0.9;\ RSS = 45.$$

The response surface was calculated according to a grid with dimensions of 40×40. The calculated and experimental data for the training sets are in agreement (Fig. S8 a, c and e; *R* ranges from 0.9972 to 0.9993). On the contrary, no satisfactory agreement is achieved for both the validation and test sets (*R* ranges from 0.8870 to 0.9869). The shapes of the obtained response surfaces are quite irregular, indicating that overfitting had occurred (Fig. S8 b, d and f).

Moreover, the polynomial model does not allow for properly fitting the experimental dose-response curves (Fig. S9) as done by the neural network (Fig. 3). This result is instead crucial for the application of the method proposed in this work, as described in Section 4.5. Finally, the resulting *NMDEI* surfaces do not agree with the experimental values (Fig. S10).

5. Conclusions

A generalized and rigorous mathematical form for the definition of additive effect for an arbitrary number of drugs has been proposed. An advanced *model-free* approach of data exploration and analysis, based on the ANN and ED was set up to predict and quantify the synergism of drugs.

From the analysis of the calculated cytotoxicity surface, the drug combinations with the desired cytotoxicity and the related lowest dose of the drugs can be found. From the analysis of the calculated *NMDEI* surface, the drug combination with the highest synergistic effect can be chosen. Unlike traditional methods, the use of ANN allows to evaluate the cytotoxicity of all the possible combinations on the entire space defined by the chosen concentration intervals.

The copper(II) compounds Cu(1,10-orthophenanthroline)$(H_2O)_2(ClO_4)_2$, [Cu(1,10-orthophenanthroline)$_2$$(H_2O)$]$(ClO_4)_2$ or [Cu(1,10-orthophenanthroline)$_2$(imidazolidine-2-thione)]$(ClO_4)_2$ act synergistically with **CDDP**. Against *in vitro* tested cells, the optimal compositions of the combinations present an antiproliferative effect 3 to 6 times greater than that of **CDDP** alone. The combinations with the maximum synergistic effect present high cytotoxic activity (from 74% to 83%), with required doses significantly lower than those needed for the individual drugs. The predicted combinations that presented the highest synergistic effect were actually prepared and experimentally tested. In all cases, the data predicted by the network were experimentally confirmed.

Acknowledgments

Support from Ministry of Education, Youth and Sports of Czech Republic (Projects MSM, 0021622411, 0021627501) and Czech Science Foundation (Projects no. 104/08/0229, 202/07/1669) are greatly acknowledged. This research has been also supported by the project R&D center for low-cost plasma and nanotechnology surface modifications (CEPLANT) CZ.1.05/2.1.00/03.0086 funding by European Regional Development Fund.

Federica Trudu gratefully acknowledges Sardinia Regional Government for the financial support of her PhD scholarship P.O.R. Sardegna F.S.E. Operational Programme of the Autonomous Region of Sardinia, European Social Fund 2007–2013—Axis IV Human Resources, Objective l.3, Line of Activity l.3.1.

Appendix A. Supporting information

Supplementary data associated with this article can be found in the online version at http://dx.doi.org/10.1016/j.talanta.2013.04.031.

References

[1] W.R. Greco, G. Bravo, J.C. Parsons, Pharmacol. Rev. 47 (1995) 331–385.
[2] M.C. Berenbaum, Pharmacol. Rev. 41 (1989) 93–141.
[3] T.C. Chou, Mol. Pharmacol. 10 (1974) 235–247.
[4] T.C. Chou, P. Talalay, Eur. J. Biochem. 115 (1981) 207–216.
[5] S. Loewe, Arzneim. Forsch. 3 (1953) 285–290.
[6] T.C. Chou, Pharmacol. Rev. 58 (2006) 621–681.
[7] T.C. Chou, Cancer Res. 70 (2010) 440–446.
[8] T.C. Chou, P. Talalay, Adv. Enzyme Regul. 22 (1984) 27–55.
[9] A. Estman, N. Schulte, Biochemistry 27 (1988) 4730–4734.
[10] A.C.M. Plooy, M. van Dijk, P.H.M. Lohman, Cancer Res. 44 (1984) 2043–2051.
[11] T. Furuta, T. Ueda, G. Aune, A. Sarasin, K.H. Kraemer, Y. Pommier, Cancer Res. 62 (2002) 4899–4902.
[12] D. Bas, İ.H. Boyacl, J. Food Eng. 78 (2007) 836–845.
[13] D.L. Massart, B.G.M. Vandeginste, L.M.C. Buydens, S. De Jong, P.J. Lewi, J. Smeyers-Verbeke, Handbook of Chemometrics and Qualimetrics, Part A, Elsevier Science, 1997 P.O. Box 211, 1000 AE Amsterdam, The Nederlands.
[14] F. Carvallo-Chaigneau, C. Trejo-Solis, C. Gomez-Ruiz, E. Rodriguez-Aguilera, L. Macias-Rosales, E. Cortes-Barberena, C. Cedillo-Pelaez, I. Gracia-Mora, L. Ruiz-Azuara, V. Madrid-Marina, F. Constantino-Casas, Biometals 21 (2008) 17–28.
[15] T. Pivetta, M.D. Cannas, F. Demartin, C Castellano, S. Vascellari, G. Verani, F. Isaia, J. Inorg. Biochem. 105 (2011) 329–338.
[16] T. Pivetta, F. Isaia, G. Verani, C. Cannas, L. Serra, C. Castellano, F. Demartin, F. Pilla, M. Manca, A. Pani, J. Inorg. Biochem. 114 (2012) 28–37.
[17] J.L. Webb, Effect of more than one inhibitor, in Enzymes and Metabolic Inhibitors, vol. 1, Academic Press, New York, NY, 1961, p. 66 and 488.
[18] C.I. Bliss, Ann. Appl. Biol. 26 (1939) 585–615.
[19] I.A. Basheer, M. Hajmeer, J. Microbiol. Methods 43 (2000) 3–31.
[20] D. Svozil, V. Kvasnička, J. Pospíchal, Chemometr. Intell. Lab. 39 (1997) 43–62.
[21] M. Riedmiller, H. Braun, Proceedings of IEEE International Conference on Neural Networks, vol. 1, 1993, pp. 586–591.
[22] S.S. Rao, Optimisation: Theory and Applications Ravi, Acharya for Wiley Eastern, New Delhi, 1978.
[23] R. Leardi, Anal. Chim. Acta 652 (2009) 161–172.
[24] R. Pauwels, J. Balzarini, M. Baba, R. Snoeck, D. Schols, P. Herdewijn, J. Desmyster, E. De Clercq, J. Virol. Methods 20 (1988) 309–321.
[25] K. Sládková, J. Houška, J. Havel, Rapid Commun. Mass Spectrom. 23 (2009) 3114–3118.

Supplementary materials, figures:

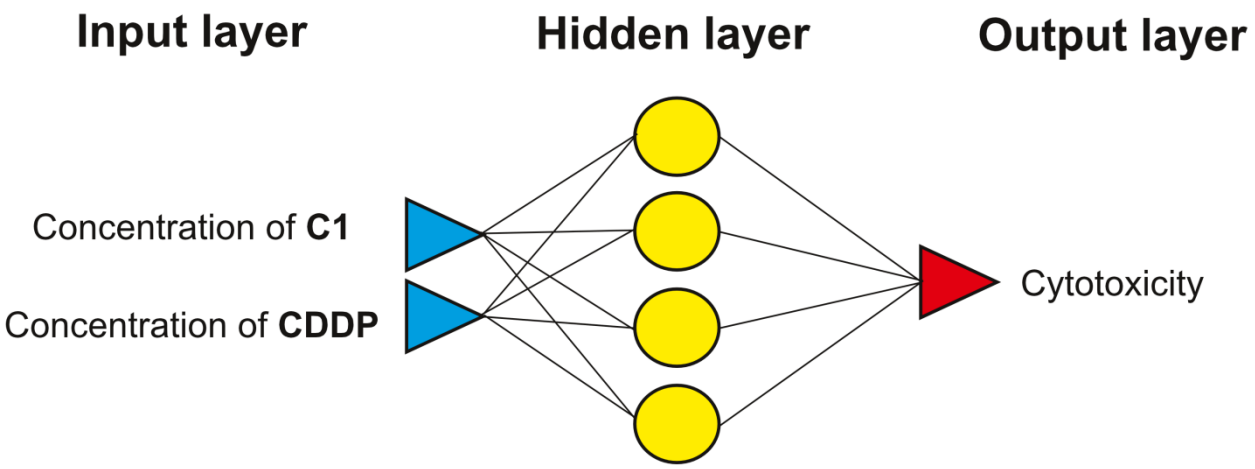

Fig. S1. The architecture of the ANN for the system **C1-CDDP**.

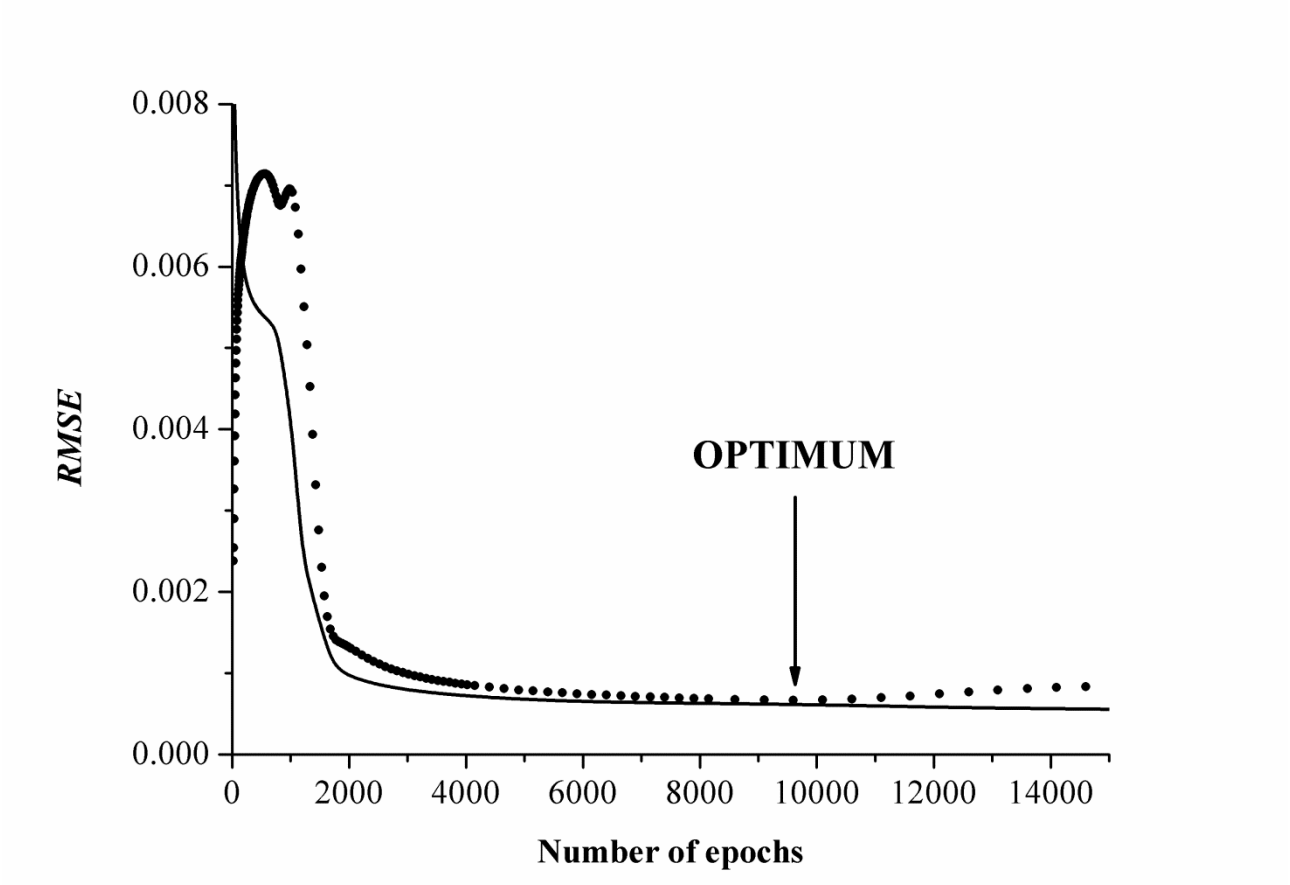

Fig. S2. Plot of the root mean square error (*RMSE*) *vs.* the number of epochs for the system **1-CDDP** (- training set, ••• validation set). The optimal number of epochs is shown by an arrow.

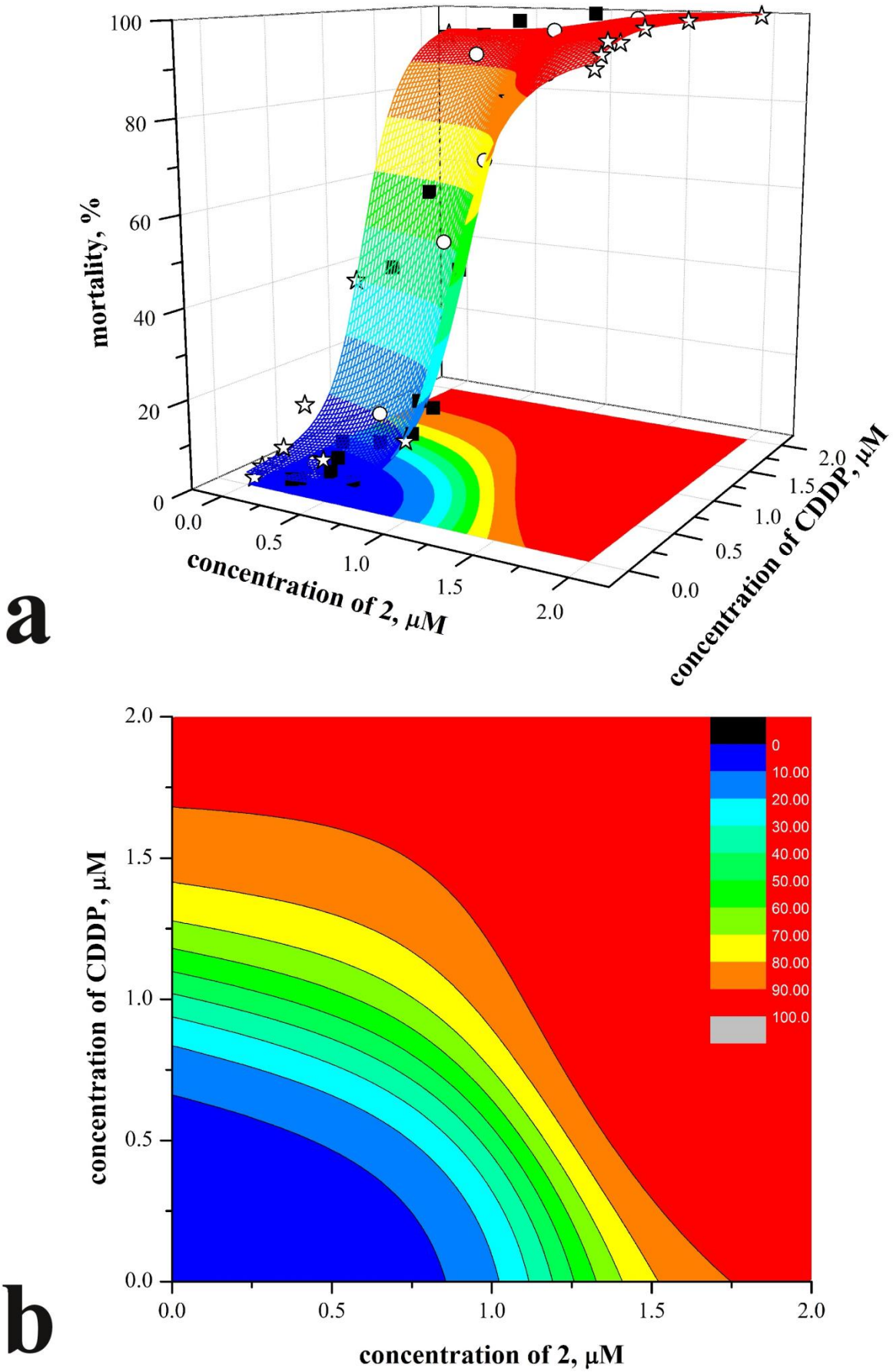

Fig. S3. Response surface with experimental data (■ training set, ☆ validation set and ○ test set) (**a**) and contour plot of cytotoxicity iso-values (**b**) for the system **2-CDDP**.

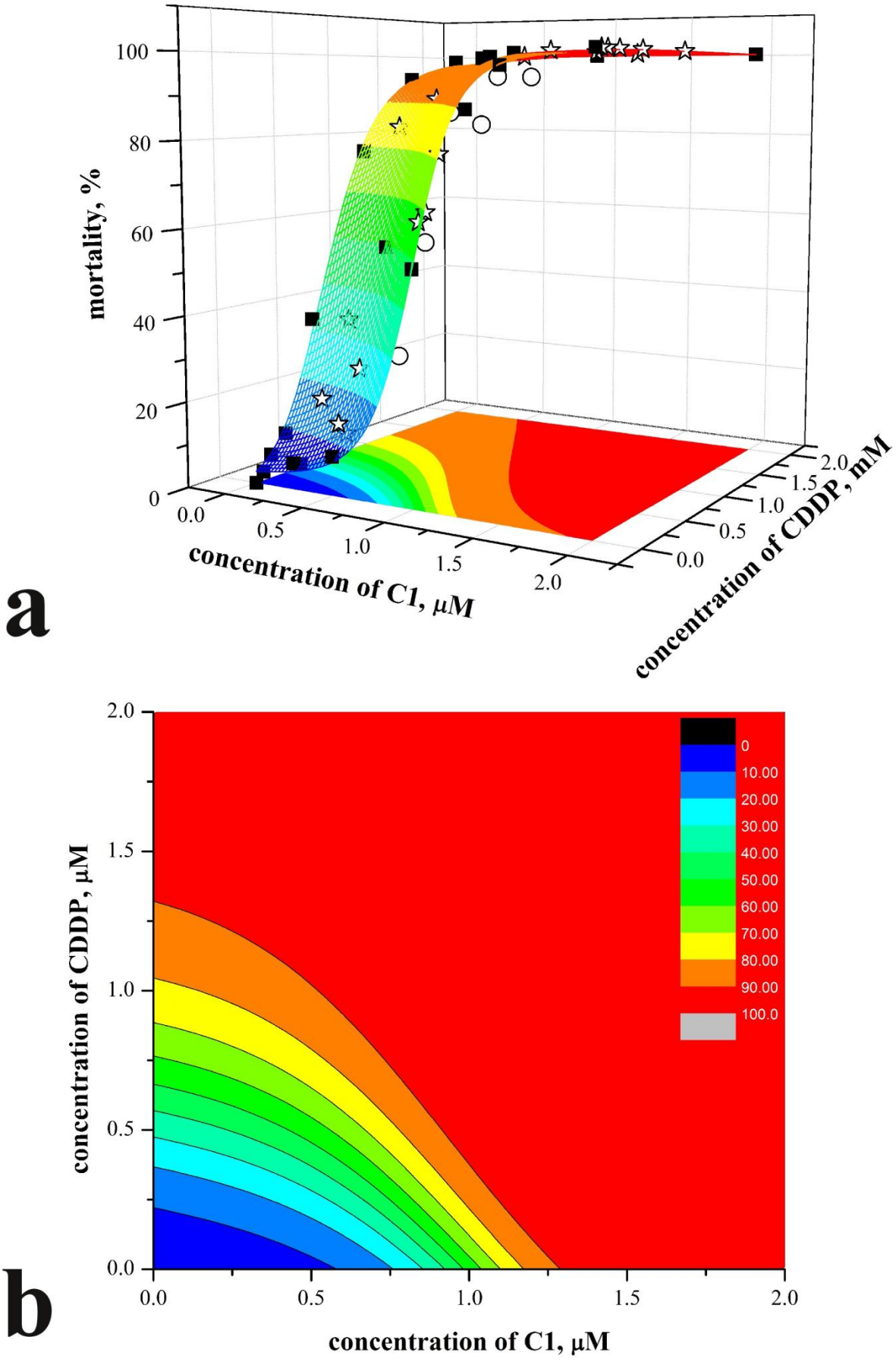

Fig. S4. Response surface with experimental data (■ training set, ☆ validation set and ○ test set) (**a**) and contour plot of cytotoxicity iso-values (**b**) for the system **C1-CDDP**.

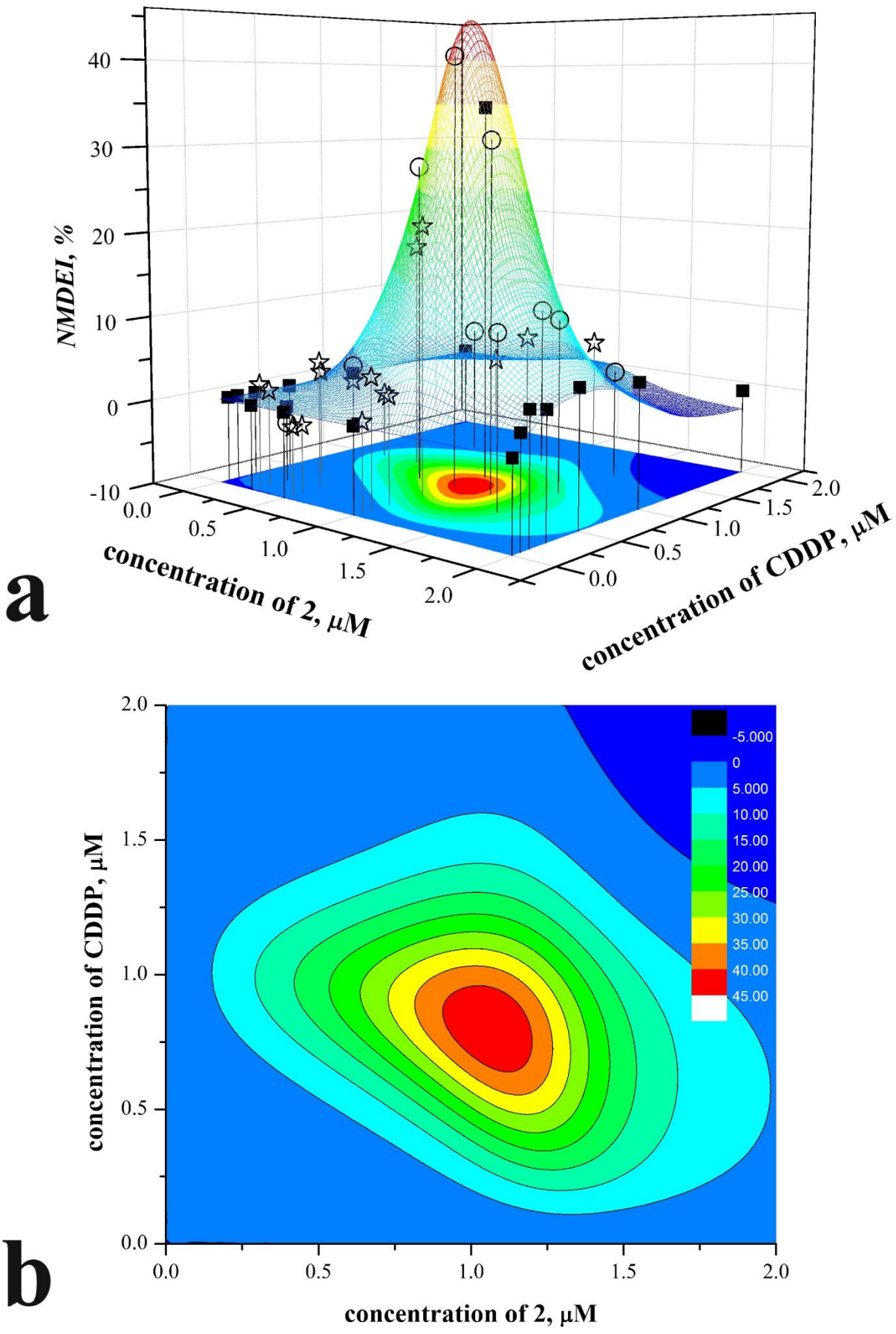

Fig. S5. *NMDEI* surface with experimental data (■ training set, ☆ validation set and ○ test set) (**a**) and contour plot of *NMDEI* iso-values (**b**) for the system **2-CDDP**.

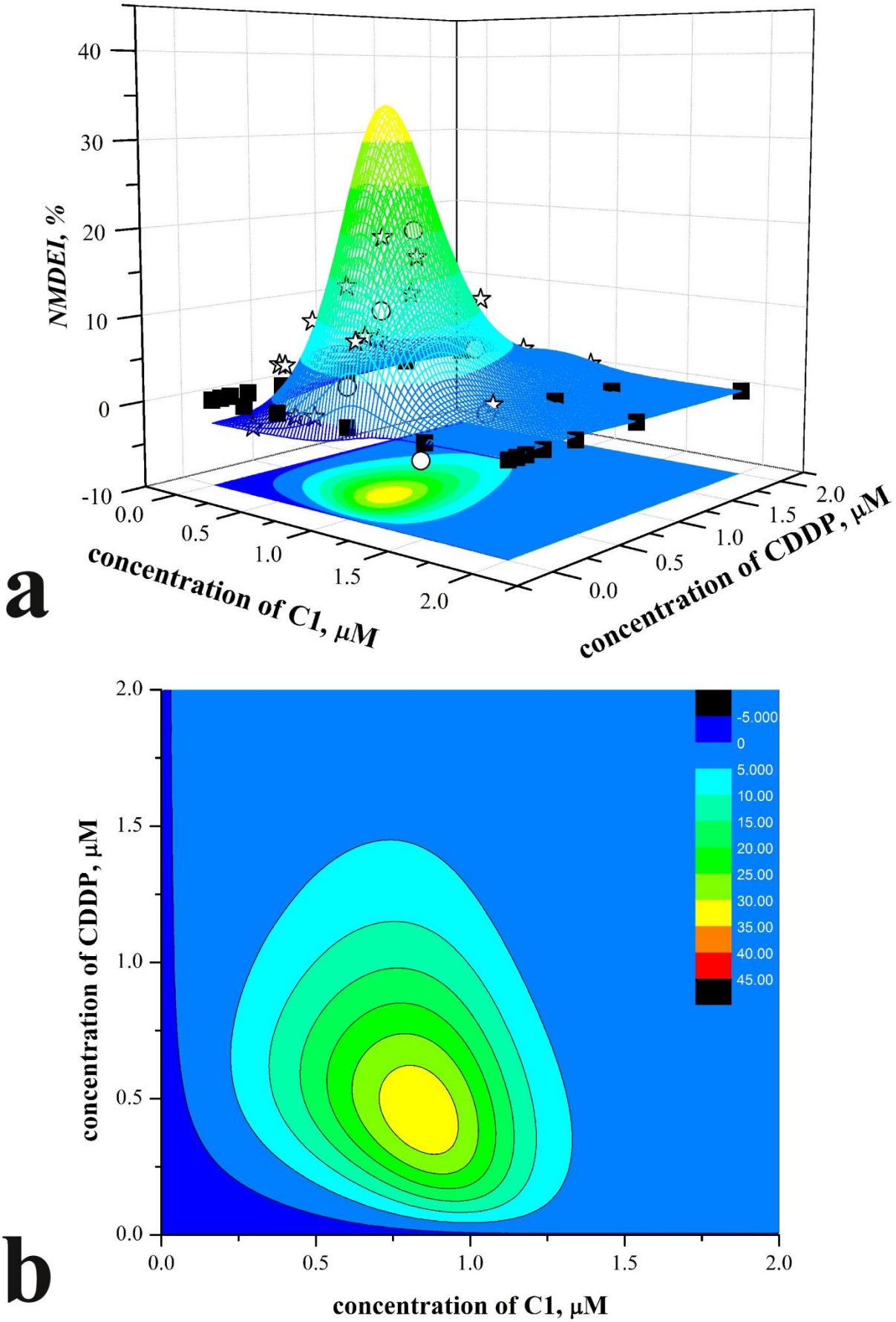

Fig. S6. *NMDEI* surface with experimental data (■ training set, ☆ validation set and ○ test set) (**a**) and contour plot of *NMDEI* iso-values (**b**) for the system **C1-CDDP**.

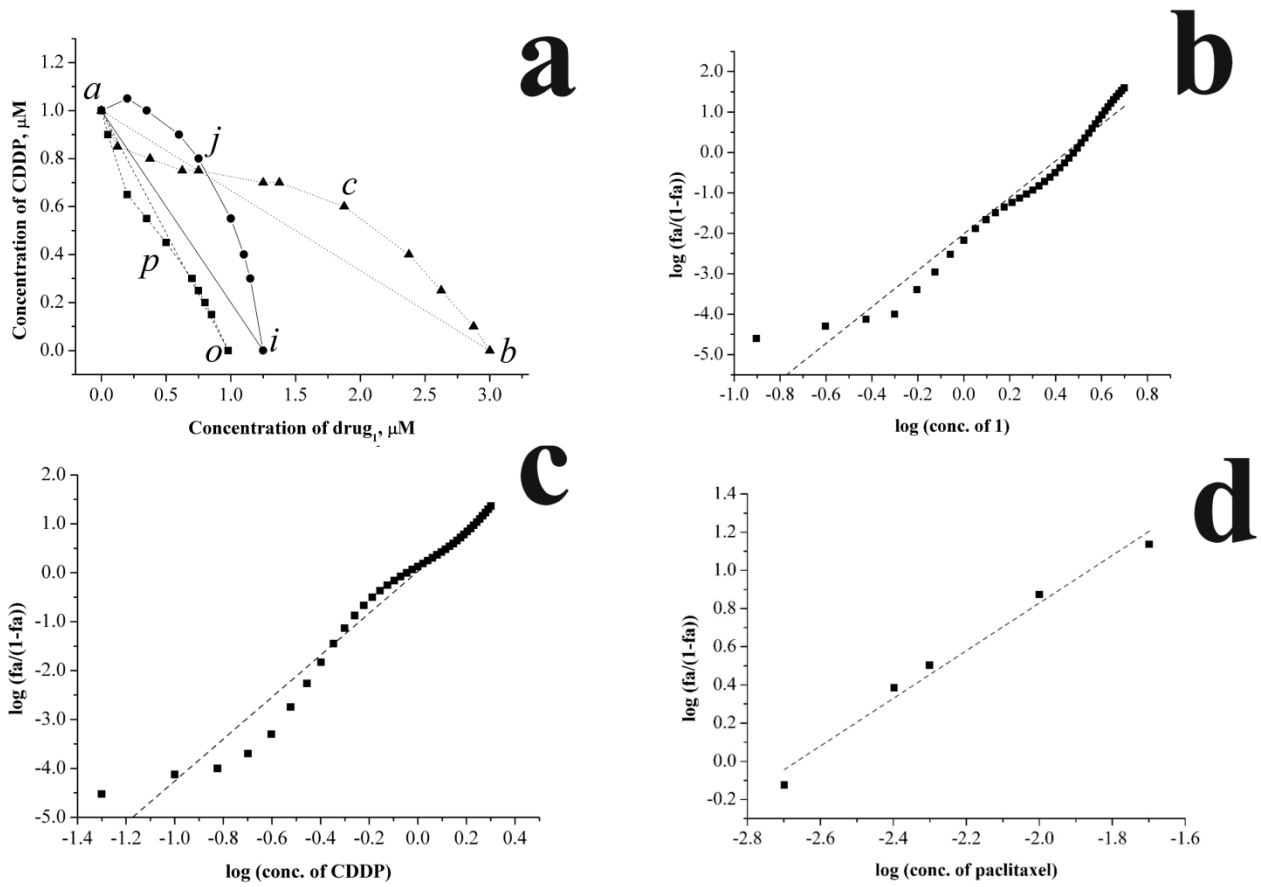

Fig. S7. Calculated isobologram for **1-CDDP** (triangle and dotted line), **2-CDDP** (circle and solid line) and **C1-CDDP** (square and dashed line) systems, for a cytotoxic activity of 50% (a); results of the application of the combination index method to the experimental data (concentration and cytotoxicity) of **1** (b), **CDDP** (c) and paclitaxel* (d); linear fitting parameters are: slope = 4.5149, intercept = -2.0159 and r = 0.9837 for **1** (b), slope = 4.2859, intercept = 0.02882 and r = 0.9769 for **CDDP** (c), slope = 1.2478, intercept = 0.1020 and r = 0.9868 for paclitaxel (d); *data from ref. 6.

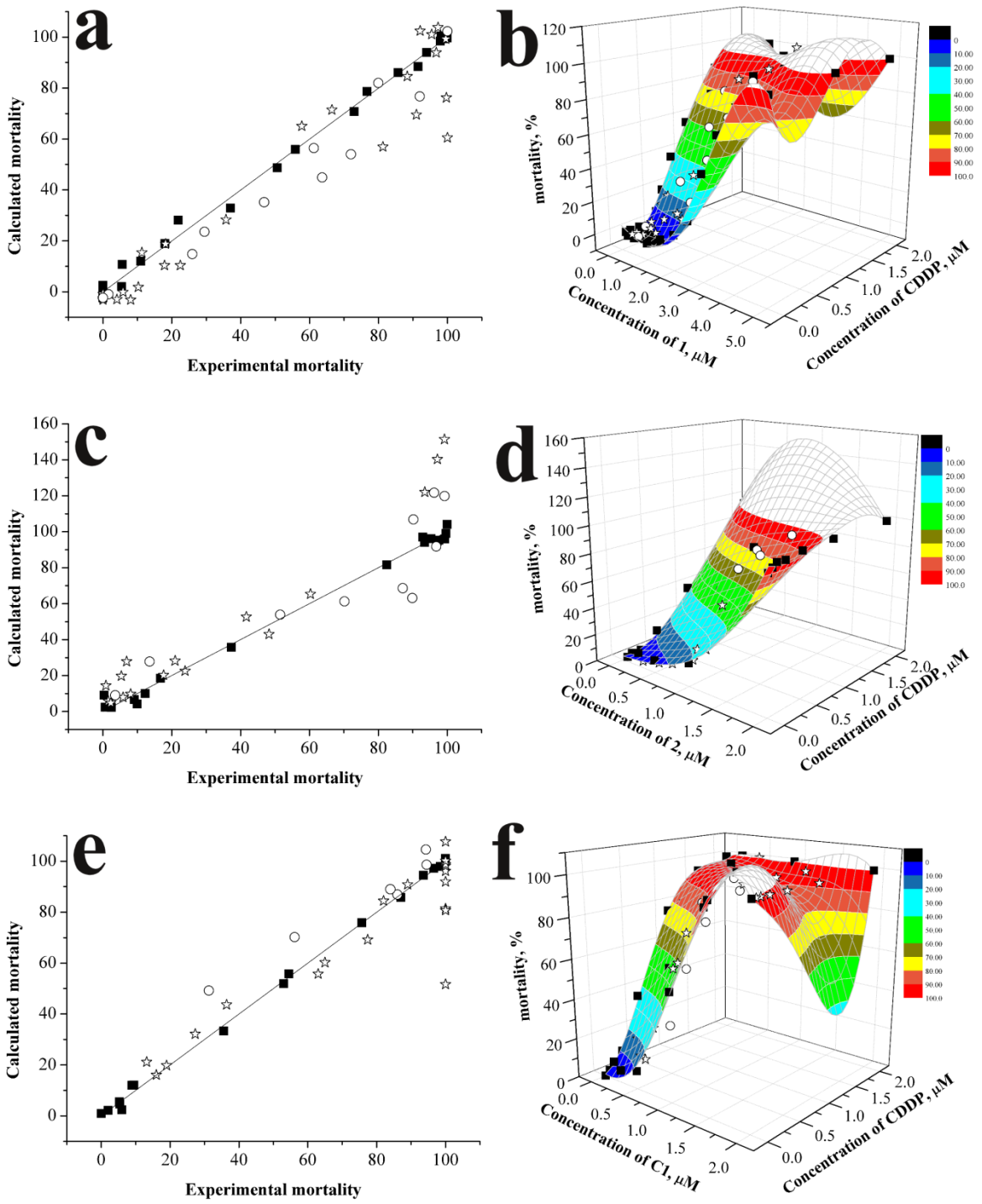

Fig. S8. Experimental (■ training set, ☆ validation set and ○ test set) and calculated mortality values and response surfaces obtained by multiple polynomial regression for a, b) **1-CDDP**, c, d) **2-CDDP** and e, f) **C1-CDDP** systems; linear fitting parameters for the equation $y = mX$ are: m = 0.999(8) with r = 0.9983 for the training set, m = 0.91(4) and r = 0.9869 for the validation set, m = 0.88(4) and r = 0.9597 for the test set for **1-CDDP**; m = 1.00(1) with r = 0.9972 for the training set, m = 1.35(6) and r = 0.9722 for the validation set, m = 1.02(7) and r = 0.8870 for the test set for **2-CDDP**; m = 0.999(5) with r = 0.9993 for the training set, m = 0.92(4) and r = 0.9149 for the validation set, m = 1.09(5) and r = 0.9020 for the test set for **C1-CDDP**.

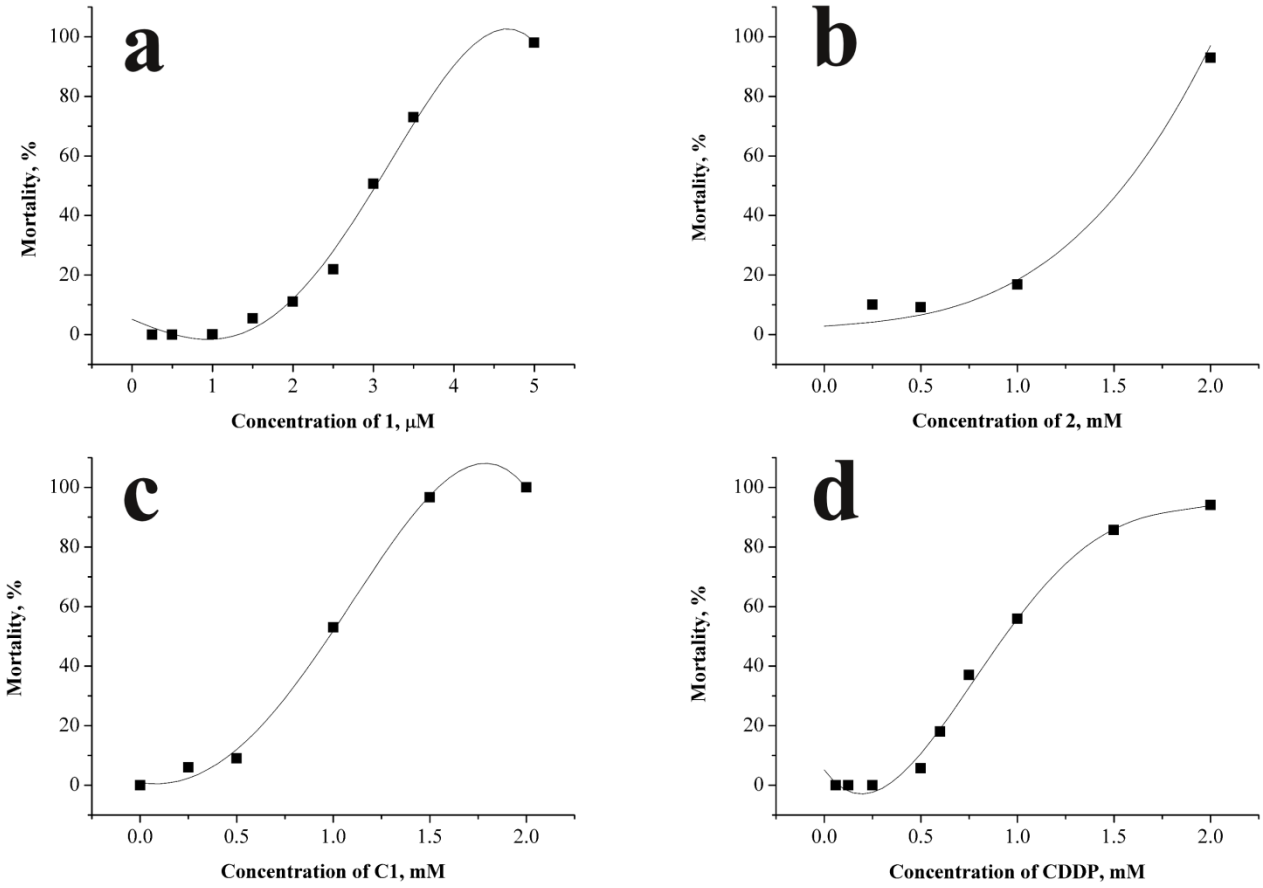

Fig. S9. Calculated (-) with multiple polynomial fitting and experimental (■) dose-response data for (**a**) **1**, (**b**) **2**, (**c**) **C1** and (**d**) **CDDP** (see section 4.9 for fitting parameters).

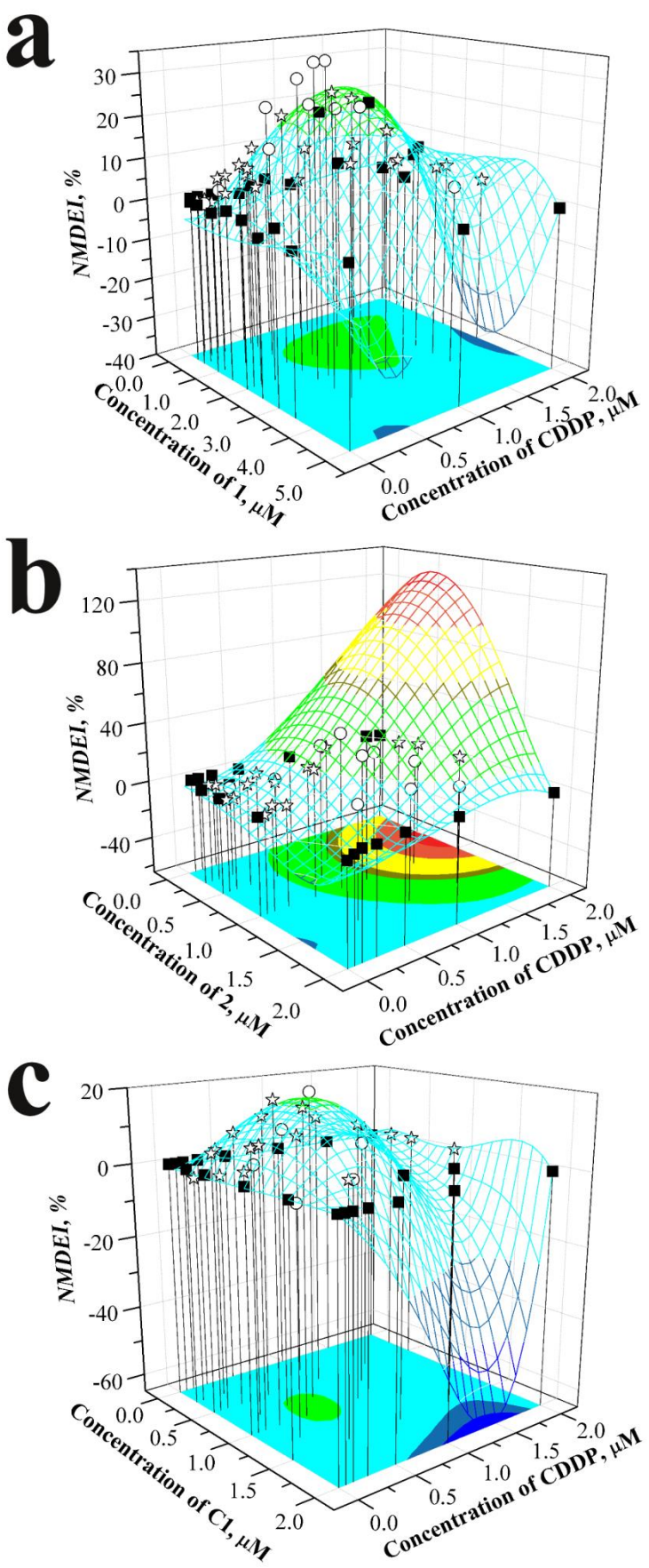

Fig. S10. *NMDEI* surface with experimental data (■ training set, ☆ validation set and ○ test set) calculated with multiple polynomial fitting for the a) **1-CDDP**, b) **2-CDDP** and c) **C1-CDDP** systems.

Chapter 2
Novel approaches to early diagnosis of prion diseases

Introduction

Protein misfolding

The biological functionality of cells depends on the correct folding of a network of thousands of proteins. The information required to fold a protein into a functional and specific three-dimensional structure is contained in its amino-acid sequence. Normally, proteins fold properly into their native conformation; however, it's possible that the protein adopts a wrong conformation, which keeps it from carrying out its function. This process, known as "misfolding", is usually hampered by a series of mechanisms of "rescue" that include molecular chaperones, whose main role is to protect the incompletely folded polypeptide chain from non-productive interactions, and the ubiquitin-proteasome system, which provides the degradation of these aberrant proteins (Fink 1999).

Misfolded proteins show a common characteristic, a high β-sheets content in their secondary structure. This particular conformation makes proteins unstable and, in attempt to seek lower energy levels and more stability, prone to aggregate in ordered fibrils called amyloid. Amyloid is toxic; its formation and deposition is the common pathological event which leads, over time, to protein misfolding disorders (PMDs), a large group of pathologies that affect several organs and tissues of the mammalians. PMDs are particularly devastating when amyloid is deposited in the central nervous system causing neurodegenerative pathologies such as Alzheimer's (AD), Huntington's and Parkinson's disorders, amyotrophic lateral sclerosis (ALS) and prion-related diseases.

Prion diseases

Also known as Transmissible Spongiform Encephalopathies (TSE), prion disorders are invariably fatal neurodegenerative pathologies that include Creutzfeldt-Jakob Disease (CJD), Gerstman-Straussler-Scheinker syndrome (GSS) and fatal familial insomnia in humans, bovine spongiform encephalopathy (BSE) in cattle, Scrapie in sheep and goats, chronic wasting disease (CWD) in cervids (Prusiner 2013). In human beings, sporadic (~85% of cases), genetic (~15%) or acquired through dietary or medical exposure to infected tissues (<5%) forms have been described (http://www.cdc.gov/ncidod/dvrd/cjd/index.htm), while in animals only infectious forms have been identified (Novakofski et al. 2005). The onset of clinical illness is preceded by a long incubation period lasting from months to decades. These diseases are usually neuropathologically characterized by spongiform change (microcavitation of the brain), neuronal loss, glial activation and accumulation of an abnormal amyloidogenic protein. The clinical features of TSEs, which consist of mental changes, ataxia,

and loss of fine control of body homeostasis, are due to massive loss of neuron function in the brain and are characteristic of many other fatal neurodegenerative diseases (Prusiner 2004).

The prion protein

It is now known that the central feature of prion diseases is the post-translational conversion of a normal host-encoded protein, the cellular prion protein (PrP^{C}), to an abnormal isoform (PrP^{Sc}) (Prusiner 1982; Legname et al. 2004). PrP^{C} is a glycoprotein made of ~208 aminoacids (35-36 kDa); it is attached to the membrane surface by a Glycophosphatidylinositol-anchor (GPI-Anchor) (Riesner 2003). The exact mechanism by which the conversion occurs is still unclear, although it is known that it is required interaction between PrP^{C} and aberrant PrP^{Sc} isoforms. Proteins interaction and conversion mainly happens in specific regions of the plasma membrane named cholesterol rich domains or lipid rafts, and it seems influenced by variations of the cholesterol content within these regions (Pani et al. 2010). After the abnormal conversion, the prion protein biochemical features change; the aberrant isoform becomes rich in β-sheet domains (Nguyen et al. 1995), insoluble in mild detergents, the N-terminal region becomes partially resistant to digestion with proteinase K, and thus prone to aggregation and deposition in form of ordered fibrils (called amyloid), which triggers cytotoxic effects eventually leading to cell death. (Telling et al. 1996; Riesner 2003).

Diagnosis of prion diseases, overlook

All the diagnosis methods to identify infectious disease nowadays in use fall into two main categories, direct and indirect. Direct diagnosis aims to find the infectious agent or its components, for example viral genome in blood samples; on the contrary, indirect diagnosis seeks for signs of the presence of the infectious agent like molecular (antibodies reactive to its components, variation of molecules, metabolites, or gene expression) and/or histopathological markers which are associated to the active presence of that particular agent in the host.

With respect to prion diseases, diagnosis becomes more complicated. Unlike other infectious diseases caused by viruses, bacteria, parasites etc., it is not possible to diagnose prion disorders using conventional methods such as PCR, serology or culture assays. This is because prions, lacking a nucleic acid component, are not life forms that can be cultured. They simply represent abnormal isoforms of the physiologic protein (PrP^{C}) that the infected organism do not recognize as foreign; therefore no immunological response (production of anti-prion antibodies) is observed.

The discovery of PrP^{Sc} in 1982 (Prusiner 1982; 1998) profoundly changed research on TSEs; it provided a molecular marker specific for all prion diseases thus opening an entire new path for direct diagnosis.

Direct diagnosis tools for TSE take advantage of the proteic nature of the prion and its biochemical features. Many antibodies have been developed to react with PrP^{Sc} and immuno-based assays are, so far, the only tests to confirm TSE cases, approved by national authorities.

Currently, definite diagnosis for both human and animal TSE is only possible postmortem. It consists in the immuno-detection of pathological PrP in the central nervous system (CNS) and, when suitable, histopathological analysis of the brain to look for spongiform changes and gliosis (this could be considered as an indirect diagnosis). The TSE surveillance in small ruminants is based on rapid tests using brainstem material. All samples with positive result in one of the rapid tests must be retested in the national reference laboratory using one of the World Organisation for Animal Health (OIE) approved confirmatory methods (Matthews et al. 2008). These are histopathology, immunohistochemistry (IHC), electron microscopy and Scrapie-associated fibrils (SAF) immunoblot. For practical reasons, only the IHC and immunoblot are routinely performed.

Although the final confirm comes from post mortem analyses, for what concerns lymphotropic TSEs, such as vCJD, Scrapie and chronic wasting disease (CWD), it is possible the use of immunohistochemistry for PrP^{Sc} on lymphoid tissue. It was shown that vCJD can be diagnosed by detection of PrP^{Sc} on tonsil biopsy (Hill et al. 1997). Similarly, pathological PrP can be detected in lymphoid tissues 42 days following oral exposure of deer to CWD prions (Sigurdson et al. 1999).

Laboratory diagnosis of TSEs is complicated by the uneven distribution of prions in body tissues; depending on the disease, highest concentrations can be consistently found in central nervous system, but very low (often under immuno-assay detection limit) in easily accessible peripheral tissues and body fluids. Of note, studies conducted by Dr. Zanusso and colleagues that highlighted the presence of PrP^{Sc} in the the neuroepithelium of the olfactory mucosa of sCJD patients, suggesting olfactory biopsy as a novel diagnostic tool in living patients (Zanusso et al. 2003).

In the last few years, in attempt to overcome detection limits of "traditional immunoassays", PrP^{Sc} capability of propagating itself has been exploited to develop several new ultrasensitive assays. These assays include include PMCA (Saà et al. 2006), rPrP-PMCA (rPMCA)(Atarashi et al. 2007), standard quaking-induced conversion (S-QuIC) (Atarashi et al. 2008), amyloid seeding assay (ASA) (Colby et al. 2007), Real-Time QuIC (RT-QuIC) (Atarashi et al. 2011) and enhanced QuIC (eQuIC) (Orrù et al. 2011). Recently, RT-QuIC was applied to neuroepithelium samples from sCJD patients (Orrù et al. 2014). The new sampling procedure, combined with the specific, fast and efficient in vitro amplification provided by RT-QuIC could represent a mile stone on the difficult pathway of antemortem diagnosis of human prion diseases.

In the past decade, improvements in mass spectroscopy (MS) techniques and their application to proteomics, gave birth to promising tools for protein profiling and biomarker discovery in various types of samples such as cell cultures, tissues and biological fluids. These methods allow to identify hundreds

of protein in a single run, but due to high abundance of protein in samples, usually a pretreatment is required. These techniques have been applied in the research of other protein biomarkers in prion diseases as well and led to the identification of several potential candidates in CSF (majority), plasma and urine. Currently, sensitivity and specificity of these new potential biomarkers need to be need to be verified (Ma et al. 2012).

At the same time, efforts have been made in finding systemic metabolism changes that could serve as early biomarkers of the disease. Of note, studies conducted by my supervisor and collaborators showing abnormal levels of cholesteryl ester (up to 3-fold higher) in lymphocytes and skin fibroblasts isolated from healthy (carrying a Scrapie-susceptible genotype) and Scrapie-affected sheep, compared to sheep with a resistant genotype (Pani et al. 2007a and b).

Chapter 2, part 1
Brain lipid profile variations as early biomarker for *in vitam* diagnosis of Scrapie

Sheep Scrapie

Scrapie is the prototype of TSEs and also the prion disease with the longest history of publication, the first authentic report on Scrapie was written in Germany and dates back to 1750 (Leopoldt 1750). It affects sheep and goats and is endemic in almost all member states of the European Union as well as in Norway, Iceland and Switzerland.

Brazil, Canada, Israel, Japan, Palestinian Autonomous Territories, Russia, Tajikistan and the USA reported Scrapie cases (atypical and/or classical) in the last 6 years. (World Animal Health Data Base (WAHID); http://web.oie.int/wahis/public.php?page=disease_timelines). According to the "World Livestock Disease Atlas 2011" (Anonymous 2011), Scrapie ranks third worldwide as cause for sheep and goat losses.

Several epidemiological studies showed that the successful transmission of classical Scrapie requires sheep with susceptible genotype. Other than susceptibility to the disease, Ovine PrP polymorphisms influence and also modulate the progression including the incubation period and clinical signs. The vast majority of polymorphisms are due to single nucleotide polymorphisms (SNP) in the DNA, which often cause single amino acid changes. Of particular interest are polymorphisms at codons 136, 154 and 171 which are clearly linked to Scrapie susceptibility in sheep. The polymorphisms mentioned above can generate five different alleles (ARQ, VRQ, AHQ, ARR and ARH) which are the only alleles with significant distribution worldwide. The combination of these alleles leads to 15 different genotypes, (Goldmann 2008). The highest risk to develop Scrapie occurs in VRQ/VRQ animals while the highest genetic resistance is associated to ARR/ARR sheep (Hunter 1997). Mode of transmissions of Scrapie were broadly discussed in the past decades (Schneider et al. 2008) but even up to now the exact transmission routes are not entirely clear. It is known that Scrapie can transmit laterally between sheep, under natural

conditions, via direct contact or through contamination of the environment. Oral route is the most efficient (Jeffrey et al. 2007; Van Keulen et al. 2008) and the main source of infection is the infectious placenta. Infectivity and PrP^{Sc} have been detected in the foetal parts, depending on the genotype of the offspring (Pattison et al. 1972; Onodera et al. 1993; Race et al. 1998; Andreoletti et al. 2002; Lacroux et al. 2007). The placenta and the amniotic fluid are shed into the environment during lambing and their ingestion by other sheep (and goats) is still assumed to be the most important infection mode within the flock (Pattison et al. 1972; Hoinville 1996). Moreover, it has been shown that Scrapie agent can remain infectious even after years in the environment (Brown and Gajdusek 1991; Seidel et al. 2007). Additional results indicate that released PrP^{Sc} may be sequestered near the soil surface and bound on soil minerals, which may then be ingested during grazing of farm animals (Johnson C.J. et al. 2006). Besides the placenta, amniotic fluid (Hoinville 1996), faeces (Terry et al. 2011) and milk (Konold et al. 2008; Lacroux et al. 2008; Maddison et al. 2009) have been shown to contain PrP^{Sc} and/or infectivity. Recent results revealed PrP^{Sc} also in the oral cavity of Scrapie infected sheep (Maddison et al. 2010; Gough et al. 2012). More artificial routes demonstrated in several experimental infections include transmissions via subcutaneous inoculation (Stamp et al. 1959; Kratzel et al. 2007), conjunctival exposure (Haralambiev et al. 1973), skin scarification (Taylor et al. 1996) and blood transfusions (Houston et al. 2008).

The incubation time of Scrapie depends on the infection route, age at infection, sheep genotype, the involved agent strain and the infectious dose. Sheep with VRQ homozygosity have the shortest incubation periods (Detwiler and Baylis 2003; Ersdal et al. 2005; Ryder et al. 2004). Iatrogenic infections lead to slightly shorter incubation periods (Caramelli et al. 2001). In classical Scrapie, sheep show clinical disease usually between 2 and 5 years of age (average age 3.5 years). Although both sexes appear to be equally affected, disease manifestations in rams occur often at slightly younger age (Wineland et al. 1998; Lühken et al. 2007; McIntyre et al. 2008). However, also shorter and longer incubation periods ranging between 1 and up to 11 years were reported (Parry 1983). Scrapie-diseased animals younger than 18 months are fairly rare (Dickinson and Stamp 1969) although it is usually not possible to establish the time of infection in older Scrapie-diseased sheep (Detwiler and Baylis 2003). Isolation of animals from the flock is often the first clinical sign, more specific symptoms at the early stage are central nervous system deficits and loss of wool caused by pruritus. Affected animals may appear normal but if stimulated by stress (i.e. sudden noise, excessive movement and handling) tremor becomes evident. At later stages, the animal may even fall down in a convulsive state (Hörnlimann et al. 2007; Ulvund 2007). Not all symptoms are always present but usually more than one is noticeable (Hörnlimann et al. 2007).

Membrane lipid environment and protein misfolding

It appears that cholesterol is not uniformly distributed within membranes, but into regions named cholesterol-rich and cholesterol poor domains. Among them, those containing saturated sphingolipids are the cholesterol-rich domains, also referred to as lipid rafts (London 2002), which float freely in plasma membranes carrying a few passenger proteins. When these proteins are activated by a ligand, the lipid rafts coalesce to form larger platforms where many different proteins converge in order to perform specific functions, such as signalling, processing or transport (Kurzchalia et al. 1999; Simons and Ehehalt al. 2002). Examples of raft proteins are receptors for growth factors, signal transducing proteins (P21), chemochine receptors, proteins of the MHC classes, antigen receptors, and various proteins with yet obscure functions, including cellular prion protein (PrP^{C}). Lipid-rafts are detergent-insoluble regions characterized by the presence of free cholesterol (FC). In normal tissue, with the exception of liver and adrenal gland, approximately 90% of the total cellular cholesterol resides in membrane raft domains as FC, while only a minor amount (approximately 1-10%) is found as cholesterol esters (CE) in shape of lipid droplets, a cytoplasmic storage system (Dessì and Batetta 2004a). Since FC levels are critical to the maintenance of proper membrane fluidity, as well as to the function and/or activation of raft-resident proteins, cells have developed a highly integrated set of homeostatic mechanisms acting in concert to finely control intracellular cholesterol levels. The FC found in cell membranes derives either from *de novo* synthesis in the endoplasmic reticulum, or from lysosomes following receptor-mediated uptake of low-density lipoproteins (LDLs) (Dessì and Batetta 2004b). Membrane FC, however, is in a dynamic state, moving back to the ER in response to changing homeostatic conditions in the cell. In fact, if cholesterol in the rafts exceeds threshold levels, its excess is promptly transferred to the ER, where it might elicit high-order responses from the control proteins embedded. FC in the ER blocks the function of its cellular sensor, the SREBP-cleavage-activating-protein (SCAP), which is needed for the proteolytic activation of the sterol-regulatory-element-binding-proteins-2 (SREBP-2), a transcriptional factor that promotes the expression of the genes involved in cholesterol synthesis (i.e. hydroxyl-methyl-glutaryl-coenzime A-reductase (HMGCoA-R)) and uptake (i.e. LDL receptor). Free cholesterol in the ER can be either used in the assembly of newly formed membrane rafts, and returned to the plasma membrane through vesicular transport, or, if in excess, converted to CE by the Acyl-cholesterol-acyl-transferase (ACAT) and stored in the cytoplasm as neutral lipid droplets (Maxfield and Tabas 2005). Viceversa, when cell membranes need FC, or when CE droplets exceed a critical threshold value, CE can be reconverted to FC by the neutral-cholesterol-ester-hydrolase (nCEH). FC can then be recycled to the membranes by cholesterol binding protein, such as caveolin-1 (Cav-1), where it can be used to replenish raft domains, or if in excess be delivered to extracellular acceptors, namely high-density lipoproteins (HDL), via the ATP-binding-cassette-sub-family A-member 1 (ABCA-1) transporter (Albrecht and Viturro 2007).

The amount of cholesterol associated with lipid rafts domains exerts profound effects on the functions of the raft-resident proteins. For instance, constant low levels of cholesterol within these domains lead to a continuous stimulus of cell growth promotion (Wang et al. 2005), or induce PrP^{C} to undergo pathologic processes leading to the generation of its corresponding pathogenic form: the PrP^{Sc} (Diomede et al. 2002). Other studies highlighted that the amyloid fibrils formation process is enhanced by anionic phospholipids (i.e. phosphatidic acid, phosphatidylserine, phosphatidylinositol) followed by neutral lipids (i.e. cholesterol, cerebrosides, diacylglycerol), zwitterionic phospholipids (i.e. phosphatidylcholine, phosphatidylethanolamine, sphingomyelin) and, at last, by anionic lipids without phosphate group (Gorbenko and Kinnunen 2006). The formation of fibrils *in vitro* system was obtained with artificial membranes containing phosphatidylcholine, phosphatidylethanolamine, gangliosides, sphingomyelin and cholesterol, typical components of the lipid rafts. Given that the lipid clustering to constitute raft domains is influenced by the interaction of lipids themselves with cholesterol, membrane formation/trafficking and protein distribution in the cellular membrane would be regulated by the cholesterol content (Simons and Ehehalt 2002).

Background and Rationale

Since lipid environment of the cellular membrane and misfolding process seem to influence each other, and the lack of studies specifically addressing lipid changes during natural Scrapie, we deemed useful a multidisciplinary study in this direction. The research project, supported by a grant from Regione Sardegna (Legge Regionale 7 Agosto 2007, N. 7), involved a collaboration with the Zooprophylactic Institute of Sassari (IZS) and a group of chemical-physicist and pathologists of the University of Cagliari. The study was performed on 18 sheep brains coming from the same Sardinian farm (15 from sheep carrying ARQ/ARQ and 3 AHQ/ARQ genotype). Seven of the brains were healthy, 8 were PrP^{Sc} positive from sheep with clinical Scrapie and 3 were PrP^{Sc} positive from sheep without recognizable clinical symptoms (asymptomatic).

IZS group provided the samples and performed the immunohistochemical and western blot analyses to highlight and quantify cerebral PrP^{Sc}, as well as the quantification of PrP gene expression and other proteins involved in cholesterol homeostasis by Real Time PCR such as ACAT1 and CAV1 (data not shown, work in progress).

The following article, published by *Chemistry and Physics of Lipids*, will show and discuss results on brain lipid profile variations during natural Scrapie.

Chemistry and Physics of Lipids 175–176 (2013) 33–40

Contents lists available at ScienceDirect

Chemistry and Physics of Lipids

journal homepage: www.elsevier.com/locate/chemphyslip

Lipid profiles in brains from sheep with natural scrapie

Antonella Rosa[a,*], Paola Scano[b], Alessandra Incani[a], Federica Pilla[a], Caterina Maestrale[c], Matteo Manca[a], Ciriaco Ligios[c], Alessandra Pani[a]

[a] Department of Biomedical Sciences, University of Cagliari, Monserrato 09042, Italy
[b] Department of Chemical and Geological Sciences, University of Cagliari, Monserrato 09042, Italy
[c] Istituto Zooprofilattico Sperimentale della Sardegna, Sassari 07100, Italy

ARTICLE INFO

Article history:
Received 3 July 2013
Accepted 1 August 2013
Available online xxx

Keywords:
Scrapie
Prion disease
Brain lipid composition
Fatty acid profile

ABSTRACT

Prion diseases are fatal neurodegenerative disorders affecting many mammals, ovine scrapie being the archetypal prion disease. Several independent studies in murine and cell-based models of scrapie have highlighted the presence of a link between prion generation and lipid alterations; yet, no data on natural disease are available. In this study we investigated levels of total lipids and cholesterol as well as profiles of fatty acids in brain homogenates from symptomatic and asymptomatic scrapie-infected sheep vs. healthy sheep, all belonging to the same flock. Lipid extracts were analyzed by means of gas chromatography and high performance liquid chromatography. Data of fatty acids were submitted to multivariate statistical analysis to give a picture of the brain lipid profiles of sheep. Interestingly, results revealed abnormalities in the brain fatty acid unsaturation of infected/symptomatic animals. Significant reduction of monoene 18:1 n-9 was detected in brain lipids from infected/symptomatic sheep, as compared to healthy and infected/asymptomatic animals, and this alteration occurred in combination with a significant increase in 18:0 level. The unsupervised Principal Component Analysis showed that infected/symptomatic and healthy sheep samples lie in two different regions of the plot, infected/asymptomatic lie mostly next to healthy. The increase of cerebral saturated fatty acids provides a rough indication of presumed alterations in lipid raft domains of nervous cells during scrapie, suggesting that they may exist in a notable viscous liquid-ordered state. Such physicochemical alteration would have a profound impact on the raft thermodynamic properties, its spatial organization, and signal transduction, all potentially relevant for prion generation.

1. Introduction

Prion diseases or Transmissible Spongiform Encephalopathy (TSE) diseases are fatal neurodegenerative disorders affecting man and many mammals (Prusiner, 1998; Aguzzi and Calella, 2009; Schneider et al., 2008). Human prion disorders are Creutzfeldt–Jakob disease, fatal familial insomnia, Gerstmann–Sträussler–Scheinker syndrome, and Kuru (Prusiner, 1998; Aguzzi and Calella, 2009), while animal diseases include scrapie of sheep and goats, transmissible mink encephalopathy in mink, chronic wasting disease in elk, and bovine spongiform encephalopathy in cattle and exotic ungulates (Prusiner, 1998; Schneider et al., 2008; Aguzzi and Calella, 2009).

Prions, commonly considered to be the causative agents of TSEs, are infectious proteins consisting of abnormally folded, partially protease resistant isoforms of the normal cellular prion protein (PrP^{C}), generally denoted as prion protein-scrapie (PrP^{Sc}) (Aguzzi and Calella, 2009; Smith et al., 2012; Pinheiro, 2006). The key molecular event is the structural conversion of PrP^{C} into PrP^{Sc}, a self-propagating process in which PrP^{Sc} acts as a conformational template recruiting PrP^{C} for further conversion (Verity and Mallucci, 2011). The misfolding process takes place in particular cell membrane domains named rafts (Pinheiro, 2006; Simons and Ehehalt, 2002; Michel and Bakovic, 2007; Fantini et al., 2002). Lipid rafts are specialized membrane microdomains characterized by high content of sphingolipids, cholesterol, and saturated fatty acids, that serve as organizing centers for different cellular processes, including trafficking of membrane and membrane-proteins (Fabelo et al., 2011; Korade and Kenworthy, 2008). Interestingly, the misfolding of the prion protein has been reported to affect the raft structure and to alter the lipid–protein and protein–protein interactions (Bate et al., 2008).

Studies in scrapie-infected mice and cells revealed the presence of major molecular and biochemical modifications in the cellular cholesterol network (Bach et al., 2009; Bate et al., 2008; Pani et al., 2007; Vascellari et al., 2011). On the other hand, no major differences were reported in the content/composition of fatty acids, polar lipids, neutral lipids, phospholipids, and plasmalogens in the brain

* Corresponding author. Tel.: +39 070 6754124; fax: +39 070 6754032.
E-mail address: anrosa@unica.it (A. Rosa).

0009-3084/$ – see front matter © 2013 Elsevier Ireland Ltd. All rights reserved.
http://dx.doi.org/10.1016/j.chemphyslip.2013.08.001

of scrapie-infected mice and hamsters (Pamplona et al., 2008; Guan et al., 1996; Dees et al., 1985; Heitzman and Skipworth, 1969).

To date, however, although ovine scrapie is the most studied prion disease (Schneider et al., 2008; Fitzmaurice et al., 2008), very few papers have been focused on the lipid alterations occurring during natural scrapie (Pani et al., 2007).

In an attempt to identify a lipid profile linked to prion ailments, we analyzed and compared the lipid composition of brains from uninfected (healthy) and scrapie-infected symptomatic (I/sympt) and asymptomatic (I/asympt) Sarda breed sheep coming from the same farm where a number of clinical scrapie cases have been diagnosed. We determined and compared levels of total lipids, total cholesterol, and fatty acids by means of gas chromatography (GC) and high performance liquid chromatography (HPLC) methods. Furthermore, GC fatty acid data were studied by means of multivariate statistical analysis. The unsupervised Principal Component Analysis (PCA) was applied to picture the fatty acid profiles of healthy and infected sheep. Malondialdehyde (MDA) levels were also measured in sheep brain homogenates as biochemical marker of lipid oxidative modification.

2. Materials and methods

2.1. Materials

Cholesterol, triolein, trilinolein, standards of fatty acids and fatty acid methyl esters, and Desferal (deferoxamine mesylate salt), were purchased from Sigma–Aldrich (Milan, Italy). All solvents used, of the highest available purity, were also from Sigma–Aldrich. The methanolic HCl (3 N) was purchased from Supelco (Bellefonte, PA). All of the other chemicals used in this study were of analytical grade.

2.2. Sheep selection and scrapie diagnosis

The study was carried out on 1 scrapie-affected Sarda sheep flocks located in Sardinia (Italy). The flock was randomly selected in Sardinia among those with a history of high clinical incidence of clinical cases of scrapie. Presence of the disease scrapie in the flock was confirmed after the notification of clinically suspected cases throughout the active surveillance for scrapie. In this flock, inside the framework of appropriate actions for eradicating scrapie, as is stipulated in EC regulations, all sheep carrying susceptible ARQ/ARQ genotypes must be sacrificed.

Thus, a number of the above susceptible animals, with or without neurological signs, were euthanized. At necroscopy, from each sheep the brains were collected and then divided into two hemispheres before being immediately frozen at −80 °C. One half was submitted to Western Blotting (WB) examination in order to define the scrapie status, as described elsewhere (Ligios et al., 2006). In the light of the WB results we selected 18 brains, 15 from ARQ/ARQ and 3 from AHQ/ARQ sheep. More in detail 7 of the brains were healthy (identified from 1H to 7H), 8 were PrP^{Sc} positive from sheep with clinical scrapie (I/sympt) (from 8IS to 15IS), 3 were PrP^{Sc} positive from sheep without clinical scrapie (I/asympt) (from 16IA to 18IA). For biochemical examination, the remaining half brain of these sheep was weighed and homogenized in ice for 2 min in saline solution, 1:1 weight:volume, using an Ultra Turrax blender. Aliquots of homogenates (500 mg of wet brain/mL of saline solution) were stored at −80 °C until lipid extraction. For further information see Table 1.

2.3. Lipid extraction from brain homogenates

Total lipids were extracted from brain homogenates using the method described by Folch et al. (1957) by addition of 12 mL of $CHCl_3$/MeOH (2/1, v/v) solution. After addition of 3 mL H_2O and centrifugation at 900 × *g* for 1 h, the $CHCl_3$ fraction was separated from the MeOH/H_2O mixture. Total lipids in $CHCl_3$ fraction were quantified by the method of Chiang et al. (1957). Separation of cholesterol and fatty acids (FA) was obtained by mild saponification (Rosa et al., 2011) as follows: 1 mL of the $CHCl_3$ fraction, containing the lipids, from each brain sample, was dried down and dissolved in 5 mL of EtOH and 100 μL of Desferal solution (25 mg/mL of H_2O), 1 mL of a water solution of ascorbic acid (25% w/v), and 0.5 mL of 10 N KOH were added. The mixtures were left in the dark at room temperature for 14 h. After the addition of 10 mL of *n*-hexane and 7 mL of H_2O, samples were centrifuged for 1 h at 900 × *g*. The hexane phase containing the unsaponifiable fraction (cholesterol) was collected and the solvent was evaporated. A portion of the dried residue was dissolved in 1 mL of MeOH and injected into the high-performance liquid chromatography (HPLC) system. After the addition of a further 10 mL of *n*-hexane to the mixtures, samples were acidified with 37% HCl to pH 3–4 and then centrifuged for 1 h at 900 × *g*. The hexane phase (saponifiable fraction) with FA was collected, and the solvent was evaporated. A portion of the dried residue was dissolved in 1 mL of CH_3CN with 0.14% CH_3COOH (v/v), and aliquots of the samples were injected into the HPLC system. An aliquot of dried FA was methylated with 1 mL of methanolic HCl (3 N) (Rosa et al., 2011; Christie, 1993) for 30 min at room temperature. After the addition of 4 mL of *n*-hexane and 2 mL of H_2O, samples were centrifuged for 20 min at 900 × *g*. The hexane phase with FA methyl esters was collected, and the solvent was evaporated. The residue was dissolved in 100 μL of *n*-hexane, and aliquots of the samples were injected into the GC system. The recovery of FA and cholesterol during the saponification was calculated using an external standard mixture prepared by dissolving 1 mg of triolein, trilinolein, and cholesterol in 5 mL of EtOH and processed as samples. All solvent evaporation was performed under vacuum.

2.4. HPLC analysis

Analyses of cholesterol and unsaturated FA were carried out with an Agilent Technologies 1100 liquid chromatograph (Agilent Technologies, Palo Alto, CA) equipped with a diode array detector (HPLC-DAD). Cholesterol, detected at 203 nm, was measured with the use of a Chrompack column (Chrompack, Middelburg, The Netherlands), Inertsil 5 ODS-3, 150 mm × 3 mm, and MeOH as the mobile phase, at a flow rate of 0.4 mL/min (Rosa et al., 2011). Analyses of unsaturated FA, detected at 200 nm, was carried out with a XDB-C_{18} Eclipse (150 mm × 4.6 mm, 3.5 μm particle size) (Agilent Technologies) equipped with a Zorbax XDB-C_{18} Eclipse (12.5 mm × 4.6 mm, 5 μm particle size) guard column (Agilent Technologies), with a mobile phase of $CH_3CN/H_2O/CH_3COOH$ (75/25/0.12, v/v/v), at a flow rate of 2.3 mL/min (Rosa et al., 2011). The temperature of the column was maintained at 37 °C.

The identification of cholesterol and FA was made using standard compounds and conventional UV spectra, generated with the Agilent Chemstation A.10.02 software. Calibration curves of all of the compounds were constructed using standards and were found to be linear, with correlation coefficients >0.995.

2.5. GC analysis of FA methyl esters

FA methyl esters were measured on a gas chromatograph Hewlett–Packard HP-6890 (Hewlett–Packard, Palo Alto, CA) with a flame ionization detector and equipped with a cyanopropyl methylpolysiloxane HP-23 FAME column (30 m × 0.32 mm × 0.25 μm) (Hewlett–Packard). Nitrogen was used as a carrier gas at a flow rate of 2 mL/min. The oven temperature was set at 175 °C; the injector temperature was set at 250 °C; and the detector temperature was set at 300 °C. The FA methyl

Table 1
Summary of cases.

Sample	PrPSc	Genotype	Sex	Age (months)	Brain weight (g)	Group
1	–	ARQ/ARQ	F	30	60.7	Healthy
2	–	ARQ/ARQ	F	30	53.2	
3	–	ARQ/ARQ	F	54	50.2	
4	–	ARQ/ARQ	F	54	54.0	
5	–	ARQ/ARQ	F	30	47.7	
6	–	AHQ/ARQ	F	30	54.5	
7	–	ARQ/ARQ	F	30	57.2	
8	+	ARQ/ARQ	F	24	45.1	Infected symptomatic (I/sympt)
9	+	ARQ/ARQ	F	24	49.0	
10	+	ARQ/ARQ	F	24	45.0	
11	+	ARQ/ARQ	F	36	50.0	
12	+	ARQ/ARQ	F	24	58.2	
13	+	ARQ/ARQ	F	54	63.9	
14	+	AHQ/ARQ	F	18	46.1	
15	+	AHQ/ARQ	F	18	53.0	
16	+	ARQ/ARQ	F	54	57.3	Infected asymptomatic (I/asympt)
17	+	ARQ/ARQ	F	54	60.6	
18	+	ARQ/ARQ	F	30	53.0	

esters were identified by comparing the retention times to those of standard compounds. The composition of individual FA was calculated as a percentage of the total amount of FA (g %), using the Hewlett–Packard A.05.02 software.

The following FA indices were also calculated: saturated FA (SFA); unsaturated FA (UFA); monounsaturated FA (MUFA); polyunsaturated FA from n-3 and n-6 series (PUFA n-3 and PUFA n-6); average chain length (ACL) = $[(\Sigma\%Total_{14} \times 14) + (\Sigma\%Total_{16} \times 16) + (\Sigma\%Total_{18} \times 18) + (\Sigma\%Total_{20} \times 20) + (\Sigma\%Total_{22} \times 22)]/100$; double bond index (DBI) = $[(1 \times \Sigma\%$ monoenoic$) + (2 \times \Sigma\%$ dienoic$) + (3 \times \Sigma\%$ trienoic$) + (4 \times \Sigma\%$ tetraenoic$) + (5 \times \Sigma\%$ pentaenoic$) + (6 \times \Sigma\%$ hexaenoic$)]$, and peroxidizability index (PI) = $[(0.025 \times \Sigma\%$ monoenoic$) + (1 \times \Sigma\%$ dienoic$) + (2 \times \Sigma\%$ trienoic$) + (4 \times \Sigma\%$ tetraenoic$) + (6 \times \Sigma\%$ pentaenoic$) + (8 \times \Sigma\%$ hexaenoic$)]$ (Pamplona et al., 2008).

2.6. Analyses of free unsaturated FA in the brain

Aliquots (1 mL) of $CHCl_3$ fractions obtained from brain homogenates by the Folch et al. procedure, were dried down and dissolved in CH_3CN with 0.14% CH_3COOH (v/v). Aliquots of these solutions were injected into the HPLC system. Quali-quantitative composition of free unsaturated FA (FFA) was performed as previously reported in the Section 2.4.

2.7. Measurement of the oxidation product MDA

MDA levels were measured in brain homogenates in saline solution (1 mL) by TBARS test as described by Rosa et al. (2012). MDA–TBA adduct quantification was conducted by HPLC-DAD analysis using a reverse phase column Varian Inertsil ODS-2 (150 mm × 4.6 mm) and the mixture of KH_2PO_4 50 mM pH 7/MeOH (65%/35% v/v) as mobile phase at a flow rate of 1 mL/min. The adduct MDA–TBA was revealed at 532 nm.

2.8. Statistical analysis

Evaluation of statistical significance of differences was performed using Graph Pad INSTAT software (GraphPad software, San Diego, CA, USA). Comparison between groups was assessed by one-way analysis of variance (One-way ANOVA) followed by the Bonferroni Multiple Comparisons Test. The data used to calculate the means and standard deviations for each group/parameter represent the average of at least two separate experiments, involving triplicate or duplicate analyses for each brain sample.

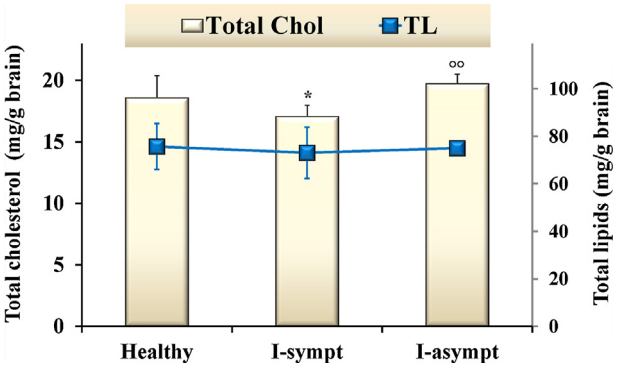

Fig. 1. Values of total lipids (TL) and total cholesterol (Total Chol) (expressed as mg/g brain) measured in the healthy (Healthy) and the scrapie-positive groups, infected/symptomatic (I/sympt) and infected/asymptomatic (I/asympt). *$P < 0.05$ versus Healthy group; °°$P < 0.01$ versus I-sympt group.

2.9. Multivariate data analysis

A PCA was applied to the fatty acid composition as obtained by GC. The data set consisted of a 18 × 17 matrix, in which rows represented samples and columns the mean fatty acid content. The generated file was imported into SIMCA-P+ program (Version 13.0, Umetrics, Umeå, Sweden), when necessary variables were log corrected, data were submitted to mean-centering and UV (unit variance) scaling before PCA.

3. Results

3.1. Lipid components of brain homogenates

Lipid fractions were extracted from brains of healthy ($n = 7$), I/sympt ($n = 8$), and I/asympt ($n = 3$) sheep. Average values (expressed as mg/g of wet brain homogenate) of total lipids (TL), obtained by Chiang procedure, and total cholesterol (Total Chol), measured by HPLC analysis after mild saponification, are shown in Fig. 1. TL lipid and Total Chol values of 75.7 ± 9.7 and 18.6 ± 1.8 mg/g of brain, respectively, were measured for healthy animals. The content of Total Chol in the brains of I/sympt group was significantly

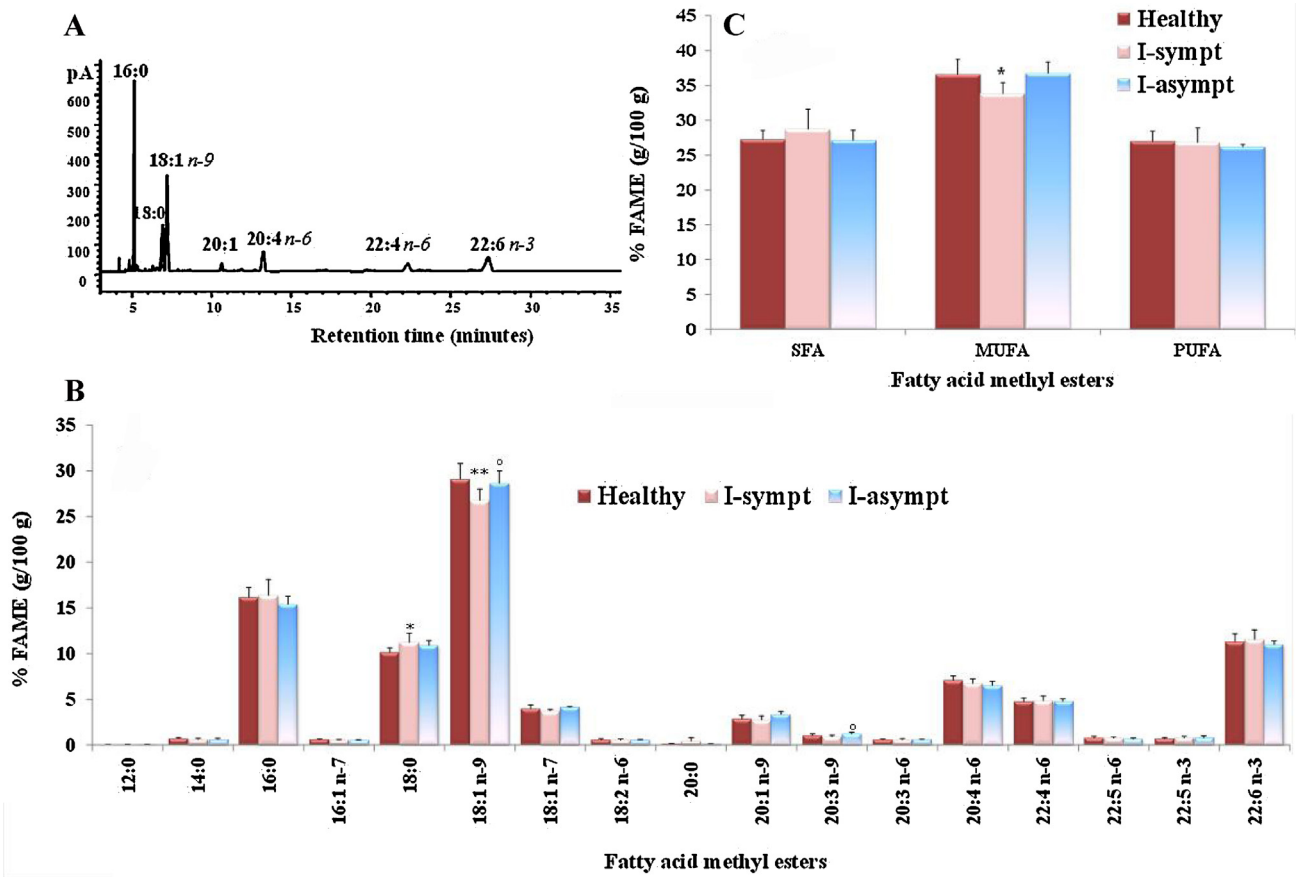

Fig. 2. GC chromatographic profile (A), composition (expressed as percentage of total fatty acids, % FAME) (B), and total values (%) of saturated (SFA) monounsaturated (MUFA), and polyunsaturated (PUFA) (C) of fatty acids from brains of the healthy group (Healthy) and the scrapie-positive groups, infected/symptomatic (I/sympt) and infected/asymptomatic (I/asympt). $^{**}P < 0.01$, $^{*}P < 0.05$ versus Healthy group; $^{\circ}P < 0.05$ versus I-sympt group.

lower than in the other groups. The same trend, although not statistically significant, was observed for TL.

Quali-quantitative information on the individual FA that compose cerebral lipids was obtained by GC (expressed as % of total FA) and HPLC (expressed as mg/g wet brain homogenate) analyses. Fig. 2 reports the brain FA profiles as measured by GC. In particular, Fig. 2A shows, as an example, the total FA chromatographic profile of a healthy animal brain. Fig. 2B and 2C report the measured values of FA for all samples.

The lipids of healthy sheep brains were characterized by a concentration of approximately 27.2% of saturated FA (SFA, mainly 16:0 and 18:0, with percentages of 16.2% and 10.2%, respectively), 36.6% of monounsaturated (MUFA, mainly oleic acid 18:1 n-9, 18:1 n-7, and 16:1 n-7; 29.1, 4.0, and 0.6%, respectively), and 27.0% of polyunsaturated (PUFA, mainly 22:6 n-3 DHA, 20:4 n-6 AA, and 22:4 n-6; 11.3, 7.1, and 4.8%, respectively) (Fig. 2B and C). Individual fatty acid levels of lipid brains from healthy subjects revealed the presence of significant contents of monoene fatty acids, with 18:1 n-9 representing the most abundant FA in the sheep brain, as reported by other studies (Rajion et al., 1985), followed by 16:0, DHA, and 18:0. PUFA of the n-6 and n-3 series accounted for 13.9% and 12.1% of total brain FA, respectively.

Very little differences between I/asympt and healthy animals could be detected in brain total FA profile, nevertheless differences were detected between these two groups and I/sympt group (Fig. 2B and C). Total value of MUFA in I/sympt animals was significantly lower than in healthy and I/sympt animals, coupled to an evident, but not statistically significant, increase in total SFA level. Specifically, significant lower level of 18:1 n-9 and higher amount of the SFA 18:0 (also 16:0 and 20:0, though to a minor extent) were measured in I/sympt group with respect to healthy animals. Fig. 3 shows the distribution of the values (as % of total FA) of SFA, MUFA (Fig. 3A), 18:0, and 18:1 n-9 (Fig. 3B), measured for each individual brain sample of the healthy (1H–7H samples), I/sympt (8IS–15IS), and I/asympt (16IA–18IA) animal groups. Each value is the mean and standard deviation of at least two independent experiments involving duplicate/triplicate analyses for each brain sample.

The fatty acid indices: PUFA n-3, PUFA n-6, PI, DBI, ACL, were also determined and results are summarized in Fig. 4. No significant differences were observed in these global indices, among groups.

Furthermore, the content of the main unsaturated FA in brains of healthy animal group was detected by HPLC as follows: 6.40 mg/g of wet brain homogenate of 18:1 n-9, 2.41, 1.32, and 1.07 mg/g of DHA, AA, and 22:4 n-6, respectively, as reported in Fig. 5A. A lower (but not significant) level of 18:1 was measured by HPLC quantification in brains of I/sympt group with respect to healthy and I/asympt animals, however no changes were seen for other PUFA. The oxidative product MDA was also measured by HPLC in brain homogenates, and results reported in Fig. 5B. A slight, but not statistically significant, increase of this compound was observed in I/sympt animals with respect to healthy and I/asympt groups.

Quali-quantitative information on brain levels of unsaturated free FA (FFA) were obtained by direct HPLC analysis of the chloroform fraction obtained from Folch extraction. Fig. 6 shows the values of the main brain unsaturated FFA (18:1, AA, 22:4 n-6, and DHA), expressed as μg/mg lipid/g of wet brain (Fig. 6A) and as % of the sum of the four individual FFA (Fig. 6B), measured in brains of the healthy and the prion-positive groups, I/sympt and

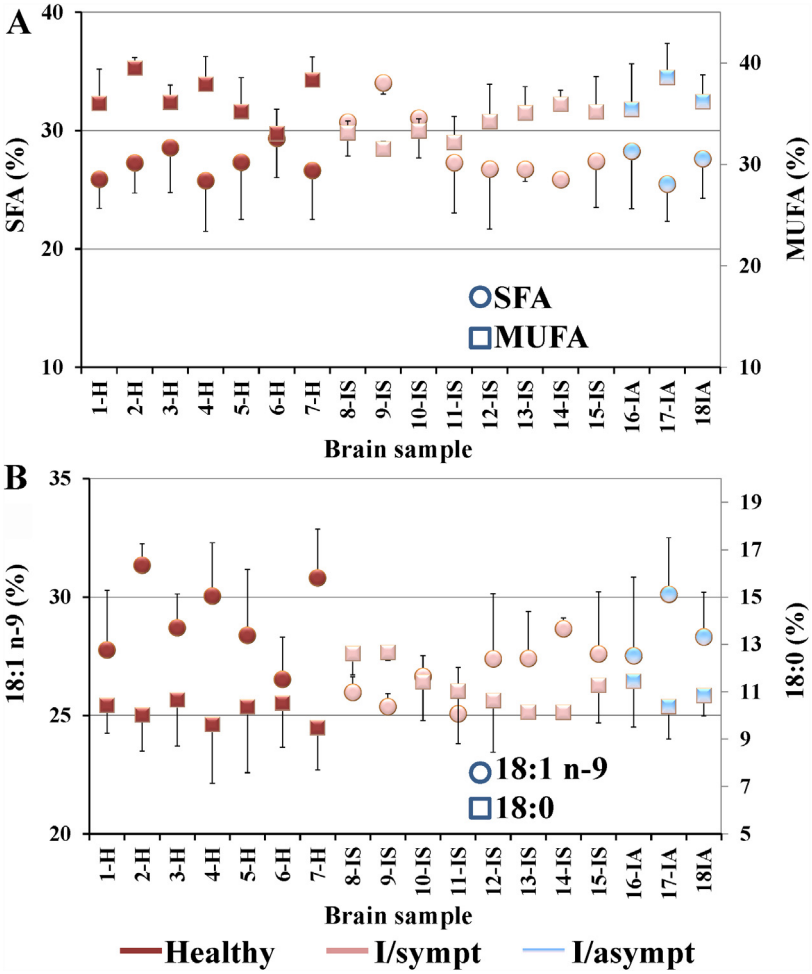

Fig. 3. Values (expressed as percentage of total fatty acids) of saturated (SFA), monounsaturated (MUFA) fatty acids (A), 18:0, and 18:1 n-9 (B), from brains of the healthy samples (1H–7H) and the scrapie-positive samples, infected/symptomatic (I/sympt, 8IS–15IS) and infected/asymptomatic (I/asympt, 16IA–18IA).

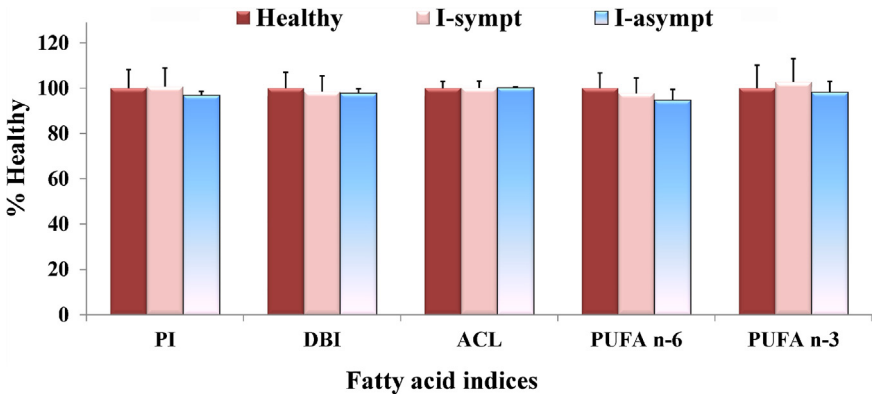

Fig. 4. Values (expressed of % Healthy) of the fatty acid indices: peroxidability index (PI), double bond index (DBI), average chain length (ACL), and n-6 and n-3 polyunsaturated fatty acids (PUFA n-6 and PUFA n-3), measured in the healthy group (Healthy) and the scrapie-positive groups, infected/symptomatic (I/sympt) and infected/asymptomatic (I/asympt).

I/asympt. The profile of unsaturated FFA in the brains of healthy group (Fig. 6A) was quite different from that of total unsaturated FA (Fig. 5A), and it was characterized by higher levels of AA and 18:1 n-9 (0.60 and 0.53 μg/mg lipids/g brain, respectively) followed by minor level of DHA and 22:4 n-6. No significant differences in the absolute amounts of FFA were observed among different groups. Interestingly, the analysis of the % values (Fig. 6B) revealed significant higher % of DHA, coupled to a lower proportion of AA, in brains of I/sympt group with respect to healthy and I/asympt groups.

3.2. Multivariate data analysis (MVA)

The FA content of lipid extracts of brain samples measured by means of GC, and reported as area %, was submitted to PCA. PCA is an unsupervised analysis and, as such, it requires no information about the class membership of samples. The first two principal components explained the 52% of total variance. Results are shown in the loading bi-plot (Fig. 7A). The loading bi-plot reports the complementary information usually shown in terms of score (samples)

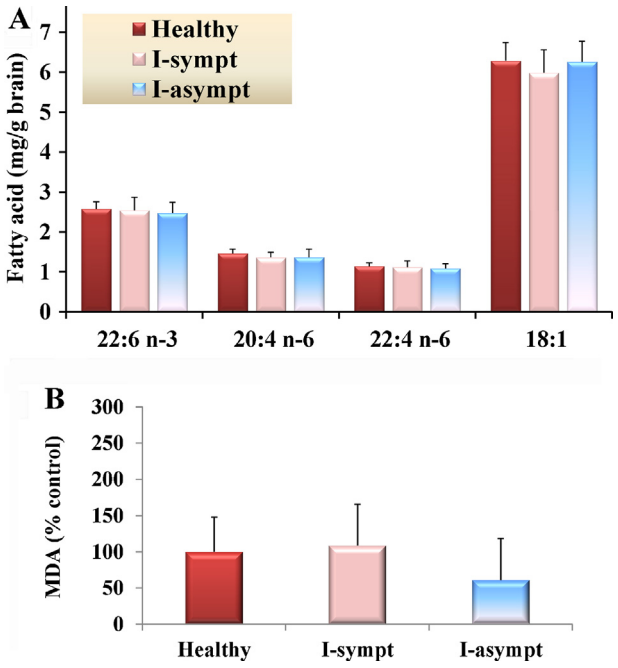

Fig. 5. Values of the main unsaturated fatty acids (18:1, 20:4 n-6, 22:4 n-6, and 22:6 n-3) (expressed as mg/g of wet brain) (A) and malondialdeyde (MDA) (expressed as % control) (B) measured by HPLC, in the brains of the healthy group (Healthy) and the scrapie-positive groups, infected/symptomatic (I/sympt) and infected/asymptomatic (I/asympt).

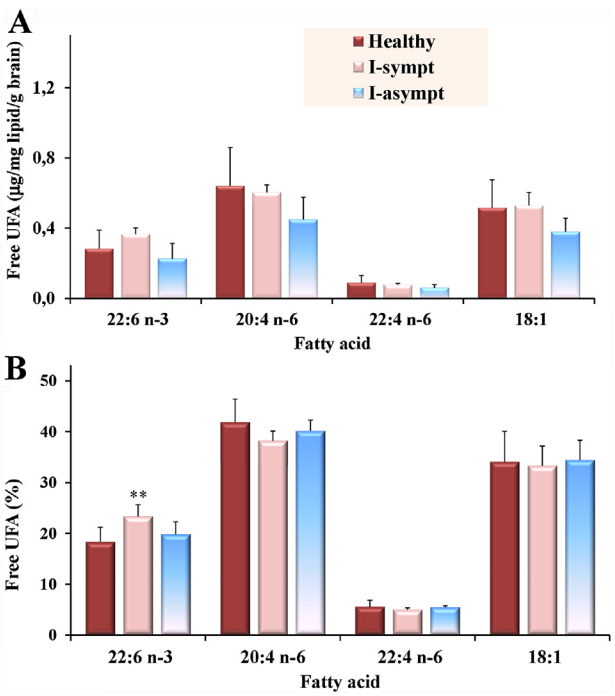

Fig. 6. Values, expressed as µg/mg lipid/g of wet brain (A) and % (B), of the main free unsaturated fatty acids (18:1, 20:4 n-6, 22:4 n-6, and 22:6 n-3) measured, by HPLC, in the brains of the healthy group (Healthy) and the scrapie-positive groups, infected/symptomatic (I/sympt) and infected/asymptomatic (I/asympt). $^{**}P < 0.01$ versus Healthy group.

plot and loading (variable) plot. Hence, this plot allows to visualize the fatty acid profile that characterizes samples and/or sample clusters; results can be interpreted following the rule: samples situated near the variables are high in these variables and are low in variables situated opposite in the plot area, variables that are found in the same area of the plot are positively correlated among themselves and negatively correlated with variables lying in the opposite side of the plot (Eriksson et al., 2006). The bi-plot shows that I/sympt and healthy sheep samples lie in two different regions of the plot, I/asympt lie mostly next to healthy. SFA characterize the positive part of PC1 together with 18:2 n-6; in the opposite side it is possible to see the highly unsaturated FA (both n-3 and n-6) and the 18:1 isomers next to 20:3 n-9 FA.

These results indicate that the overall FA profiles differ among healthy and I/asympt vs. I/sympt sheep brains. Given that such FA

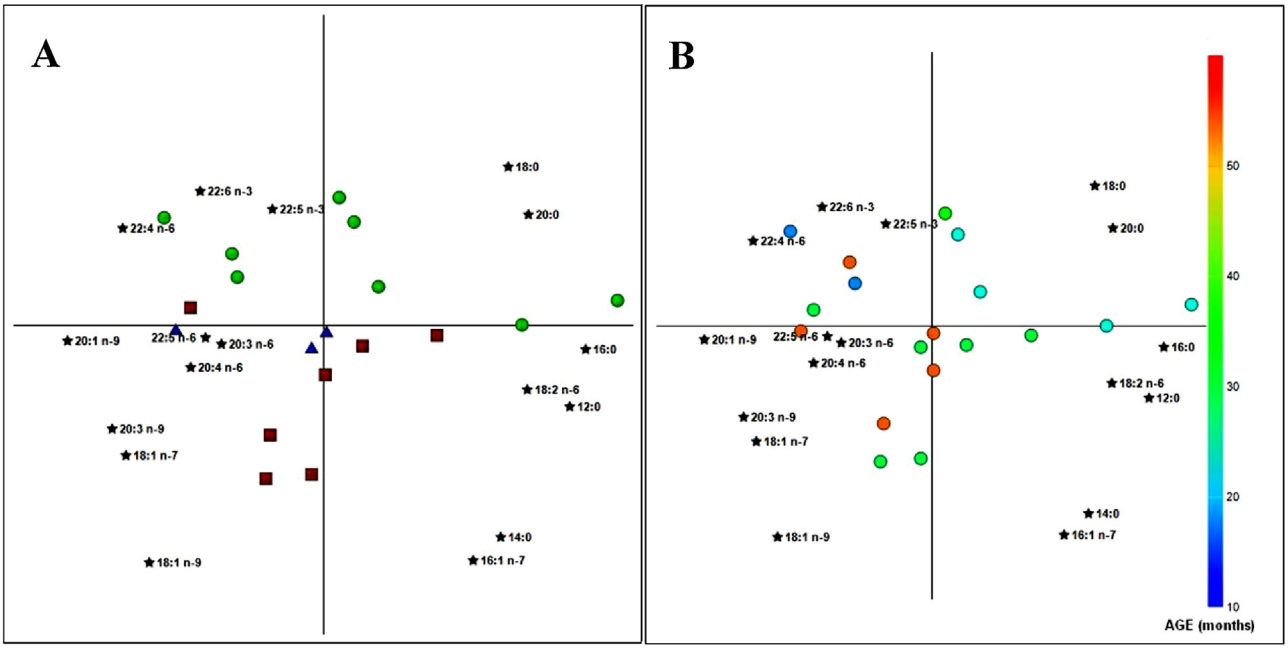

Fig. 7. Bi-plot of a Principal Component Analysis (PCA) of GC data. Variables: 5 points stars = * fatty acids. Samples: (A) red box healthy samples (Healthy), green circle = infected/symptomatic (I/sympt) and blue triangle = infected/asymptomatic (I/asympt); (B) samples colored by age of sheep as reported in the plot legend. (For interpretation of the references to color in this figure legend, the reader is referred to the web version of this article.)

distribution could be, even partially, driven by the different ages of animals, samples in the bi-plot have been colored depending on sheep age as reported in Table 1; results (Fig. 7B), however, indicate that this was not the case.

4. Discussion

Ovine scrapie represents the archetypal prion disorder, with a long history of investigation (Schneider et al., 2008; Jeffrey et al., 2009; Fast and Groschup, 2013). To date, however, studies mainly addressed genetic and pathological features (Fast and Groschup, 2013; Ligios et al., 2002; Hunter, 1997,2003), cytotoxicity and neuropathology of PrP^{Sc} isoforms (Jeffrey et al., 2009; Filali et al., 2012), and transmission routes (Ligios et al., 2011; Fast and Groschup, 2013; Hunter, 2003), while only few studies have investigated lipid modifications during natural infection and, also in that case, it focused only on the cholesterol alterations (Pani et al., 2007).

In the present study, we analyzed and compared the brain levels of TL, Total Chol, and FA of healthy, I/sympt, and I/asympt Sarda breed sheep coming from a farm affected by natural scrapie. Our data failed to reveal severe alterations in lipid composition among different groups. Nevertheless, some interesting differences were in general observed in I/sympt animals with respect to healthy and I/asympt; these latter two showing similar lipid characteristics. Brains from I/sympt group showed the lowest levels (expressed as mg/g weight brain) of TL and Total Chol, probably due to the severe brain degeneration (spongiosis, neuronal vacuolation, gliosis) existing in the clinical stage of scrapie (Kimberlin, 1969; Fast and Groschup, 2013). No significant differences were previously observed (Pani et al., 2007) in brain total cholesterol level between unaffected and affected ARQ/ARQ scrapie-susceptible animals, while a noteworthy difference was evinced in brain samples from the scrapie-resistant ARR/ARR sheep as compared to the unaffected or affected scrapie-susceptible ARQ/ARQ sheep.

Interestingly, our data revealed abnormalities in the brain FA unsaturation of I/sympt animals. Generally, the degree of FA unsaturation in membrane phospholipids determines the biophysical properties of the membrane, which in turn influences many crucial membrane-associated functions. The alteration of the degree of FA unsaturation in cell membrane has also been implicated in a variety of pathological states, including neurological diseases (Ariyama et al., 2010). We found that brain lipids from ill subjects were enriched in SFA, as compared to healthy and I/asympt animals. Significant reduction of monoene 18:1 n-9 was detected in brain lipids from I/sympt samples, and this alteration occurred in combination with a significant increase in 18:0 level. The ratio 18:1 n-9/18:0 resulted 2.97 ± 0.31, 2.40 ± 0.30, 2.69 ± 0.25 in brain lipids from healthy, I/sympt, I/asympt animals, respectively. Nevertheless, no significant differences were observed in fatty acid indices: PUFA n-3, PUFA n-6, PI, DBI, ACL, among groups. Furthermore, the multivariate statistical analysis of FA composition confirmed that the overall FA profiles differ among healthy and I/asympt vs. I/sympt sheep brains, and FA distribution was not affected at all by age.

Previous reports showed no differences in brain FA composition in normal and scrapie-affected mice (Guan et al., 1996; Heitzman and Skipworth, 1969), or lower intensity changes in FA profile (a significant decrease in MUFA level) in Syrian hamsters affected by prion disease with respect to control brain (Pamplona et al., 2008). On the other hand, significant alterations in the brain lipid composition was detected in the brain of patients with Creutzfeldt–Jakob disease (such as decrease of PUFA and increase of 16:0) (Pamplona et al., 2008).

Several lines of evidence implicate the role of lipid rafts in the conformational transition of prion proteins (Pinheiro, 2006; Simons and Ehehalt, 2002; Michel and Bakovic, 2007; Fantini et al., 2002) and the formation of PrP^{Sc} has been proposed to alter conventional lipid raft structure and the PrP^{C}-protein interactions that occur within lipid rafts (Bate et al., 2008). Lipid rafts comprise a highly dynamic clustering of proteins and lipids that play a central role in signal transduction and intercellular communication (Fabelo et al., 2011). Lipid raft domains are mainly characterized by a high content of sphingolipids containing saturated acyl chains and cholesterol; furthermore, phosphatidylcholine, mainly with saturated acyl chains, is present, as well as small amounts of phosphatidylethanolamine and phosphatidylserine (Michel and Bakovic, 2007). The specialized lipid composition of lipid rafts may influence protein function directly by modulating the properties of the membrane bilayer (Korade and Kenworthy, 2008).

Interestingly, our data showed that there was a trend for increase in the SFA content of brain lipids in I/sympt animals. The relationship 18:1 n-9/18:0 observed is physicochemically relevant since the ratio between these two fatty acids represents an evolutionary conserved mechanism to preserve the homeoviscous state of cell membranes in response to different forms of physical and/or chemical stress (Fabelo et al., 2011). The increase of brain SFA furnishes a rough indication of presumed lipid alterations in lipid membranes/rafts, indicating that in scrapie-affected sheep lipid rafts may exist in a notable viscous liquid-ordered state. Such physicochemical alteration would have a profound impact in the lipid raft thermodynamic properties, spatial organization, and signal transduction.

In general, the fatty acid composition of membrane phospholipids is likely to be affected by the exogenous FA from the diet or by altered activities of lipid-metabolizing enzymes such as fatty acid desaturases (Ariyama et al., 2010). Taking into consideration that all the sheep came from the same farm, it can be supposed that the significant increase in saturated 18:0 and the reduction in 18:1 n-9 in brains of I/sympt animals may be indicative of a down-regulation of Δ9-desaturase, the enzyme responsible for the synthesis of n-9 monounsaturated fatty acids from their saturated precursors (Fabelo et al., 2011). This would result in a concomitant loss of the ability to adjust lipid raft physical order (Fabelo et al., 2011). Overload of saturated long chain fatty acids within cells is also known to cause lipotoxicity, which contributes to various pathological conditions (Ariyama et al., 2010).

Oxidative stress is considered to be one of the key factors in the pathogenesis of prion disease (Yun et al., 2006; Pamplona et al., 2008; Filali et al., 2012). For example, the brain undergoes oxidative stress in the early stages of prion invasion into the brain and may predispose the brain to neurodegenerative mechanisms (Filali et al., 2012). Our data showed an increase, but not statistically significant, of the oxidative product MDA in I/sympt animals with respect to healthy and I/asympt groups, without significant changes in PUFA levels and peroxidability indexes.

Several observations strongly implicate phospholipases A2 (PLA2) in the pathogenesis of prion diseases (Farooqui et al., 2006; Bate et al., 2008). Our data did not reveal significant differences in the absolute amounts of brain free unsaturated FA (18:1, AA, 22:4 n-6, and DHA) among different animal groups. Nevertheless, different unsaturated FFA ratios were observed in brains of I/sympt group with respect to healthy and I/asympt groups. The phospholipase A2 family includes secretory phospholipase A2(sPLA2), cytosolic phospholipase A2 (cPLA2), plasmalogen-selective phospholipase A2(PlsEtn-PLA2), and calcium-independent phospholipase A2 (iPLA2); various isoforms of PLA2 probably act on different cellular pools of phospholipids located in different types of neural cells (Farooqui et al., 2006). Brain sPLA2 shows no selectivity for particular fatty acyl chains in the phospholipids; cPLA2 prefers AA over other fatty acids, while PlsEtn-PLA2 hydrolyzes AA and DHA from the sn-2 position of plasmalogens (Farooqui et al., 2006). The

activation of cPLA2 has been previously demonstrated in different prion models (Bate et al., 2008), and increased cPLA2 and PlsEtn-PLA2 activities have been measured in brain of patients with neurodegenerative disease (Farooqui et al., 2006). The different unsaturated FFA ratios observed among animal groups maybe due to an implication of different phospholipases that specifically cleave the acyl ester bond at the sn-2 position of membrane phospholipids to produce a mixture of free fatty acids (Farooqui et al., 2006).

In conclusion, data herein reported, although suggestive of a modified cerebral lipid environment during prion infection, do not allow to establish the relevance of lipid modifications in the progression of scrapie, nor the presence of a mechanistic link between specific lipid changes and generation of the prion protein. To specifically address these issues, time course experiments in lambs experimentally infected with scrapie are in progress.

Role of the funding source

This study was supported by grants from the Regione Autonoma della Sardegna (L.R. n° 7/2007, call 2008) and from the Fondazione Banco di Sardegna (call 2009).

References

Aguzzi, A., Calella, A.M., 2009. Prions: protein aggregation and infectious diseases. Physiol. Rev. 89, 1105–1152.
Ariyama, H., Kono, N., Matsuda, S., Inoue, T., Arai, H., 2010. Decrease in membrane phospholipid unsaturation induces unfolded protein response. J. Biol. Chem. 285, 22027–22035.
Bach, C., Gilch, S., Rost, R., Greenwood, A.D., Horsch, M., Hajj, G.N., Brodesser, S., Facius, A., Schädler, S., Sandhoff, K., Beckers, J., Leib-Mösch, C., Schätzl, H.M., Vorberg, I., 2009. Prion-induced activation of cholesterogenic gene expression by SREBP2 in neuronal cells. J. Biol. Chem. 284, 31260–31269.
Bate, C., Tayebi, M., Williams, A., 2008. Sequestration of free cholesterol in cell membranes by prions correlates with cytoplasmic phospholipase A2 activation. BMC Biol. 2008, 6–8.
Chiang, S.D., Gessert, C.F., Lowry, O.H., 1957. Colorimetric determination of extracted lipids. An adaptation for microgram amounts of lipids obtained from cerumen. Curr. List Med. Lit. Res. Rep. 33, 56–113.
Christie, W.W., 1993. Preparation of ester derivatives of fatty acids for chromatographic analysis. In: Christie, W.W. (Ed.), Advantage in Lipid Methodology – Two. The Oily Press, Dundee, Scotland, pp. 69–111.
Dees, C., German, T.L., Wade, W.F., Marsh, R.F., 1985. Characterization of lipids in membrane vesicles from scrapie-infected hamster brain. J. Gen. Virol. 66, 861–870.
Eriksson, L., Johansson, E., Kettaneh-Wold, N., Trygg, J., Wikström, C., Wold, S., 2006. Multi- and Megavariate Data Analysis Part I: Basic Principles and Applications. Umetrics, Umeå, Sweden.
Fabelo, N., Martín, V., Santpere, G., Marín, R., Torrent, L., Ferrer, I., Díaz, M., 2011. Severe alterations in lipid composition of frontal cortex lipid rafts from Parkinson's disease and incidental Parkinson's disease. Mol. Med. 17, 1107–1118.
Fantini, J., Garmy, N., Mahfoud, R., Yahi, N., 2002. Lipid rafts: structure, function and role in HIV, Alzheimer's and prion diseases. Expert Rev. Mol. Med. 4, 1–22.
Farooqui, A.A., Ong, W.Y., Horrocks, L.A., 2006. Inhibitors of brain phospholipase A_2 activity: their neuropharmacological effects and therapeutic importance for the treatment of neurologic disorders. Pharmacol. Rev. 58, 591–620.
Fast, C., Groschup, M.H., 2013. Classical and atypical Scrapie in sheep and goats. In: Zou, W.-Q., Gambetti, P. (Eds.), Prions and Diseases: Volume 2, Animals, Humans and the Environment. Springer Science, New York, USA, pp. 15–44.
Filali, H., Martin-Burriel, I., Harders, F., Varona, L., Serrano, C., Acín, C., Badiola, J.J., Bossers, A., Bolea, R., 2012. Medulla oblongata transcriptome changes during presymptomatic natural scrapie and their association with prion-related lesions. BMC Genom. 13, 399.
Fitzmaurice, T.J., Burke, D.F., Hopkins, L., Yang, S., Yu, S., Sy, M.S., Thackray, A.M., Bujdoso, R., 2008. The stability and aggregation of ovine prion protein associated with classical and atypical scrapie correlates with the ease of unwinding of helix-2. Biochem. J. 409 (2), 367–375.
Folch, J., Lees, M., Sloane-Stanley, G.H., 1957. A simple method for the isolation and purification of total lipid from animals tissues. J. Biol. Chem. 226, 497–509.
Guan, Z., Söderberg, M., Sindelar, P., Prusiner, S.B., Kristensson, K., Dallner, G., 1996. Lipid composition in scrapie-infected mouse brain: prion infection increases the levels of dolichyl phosphate and ubiquinone. J. Neurochem. 66, 277–285.
Heitzman, R.J., Skipworth, S.S., 1969. The fatty composition of brain and myelin of normal and scrapie-affected mice. J. Neurochem. 16, 121–122.
Hunter, N., 1997. Molecular biology and genetics of scrapie in sheep. In: Piper, L., Ruvinsky, A. (Eds.), The Genetics of Sheep. CAB International, Wallingford, Oxon, UK, pp. 225–240.
Hunter, N., 2003. Scrapie and experimental BSE in sheep. Br. Med. Bull. 66, 171–183.
Jeffrey, M., McGovern, G., Goodsir, C.M., Sís, S., González, L., 2009. Strain-associated variations in abnormal PrP trafficking of sheep scrapie. Brain Pathol. 19, 1–11.
Kimberlin, R.H., 1969. Biochemical changes in scrapie affected brain. Biochem. J. 114, 20P–22P.
Korade, Z., Kenworthy, A.K., 2008. Lipid rafts, cholesterol, and the brain. Neuropharmacology 55, 1265–1273.
Ligios, C., Jeffrey, M., Ryder, S.J., Bellworthy, S.J., Simmons, M.M., 2002. Distinction of scrapie phenotypes in sheep by lesion profiling. J. Comp. Pathol. 127, 45–57.
Ligios, C., Cancedda, M.G., Madau, L., Santucciu, C., Maestrale, C., Agrimi, U., Ru, G., Di Guardo, G., 2006. PrP(Sc) deposition in nervous tissues without lymphoid tissue involvement is frequently found in ARQ/ARQ Sarda breed sheep preclinically affected with natural scrapie. Arch. Virol. 151, 2007–2020.
Ligios, C., Cancedda, M.G., Carta, A., Santucciu, C., Maestrale, C., Demontis, F., Saba, M., Patta, C., DeMartini, J.C., Aguzzi, A., Sigurdson, C.J., 2011. Infectious prions through the milk. J. Virol. 85, 1136–1139.
Michel, V., Bakovic, M., 2007. Lipid rafts in health and disease. Biol. Cell. 99, 129–140.
Pamplona, R., Naudí, A., Gavín, R., Pastrana, M.A., Sajnani, G., Ilieva, E.V., del Río, J.A., Portero-Otín, M., Ferrer, I., Requena, J.R., 2008. Increased oxidation, glycoxidation, and lipoxidation of brain proteins in prion disease. Free Radic. Biol. Med. 45, 1159–1166.
Pani, A., Abete, C., Norfo, C., Mulas, C., Putzolu, M., Laconi, S., Cannas, M.D., Orru', C.D., La Colla, P., Dessì, S., 2007. Cholesterol metabolism in brain and skin fibroblasts from Sarda breed sheep with scrapie resistant or susceptible genotype. Am. J. Infect. Dis. 3, 142–150.
Pinheiro, T.J., 2006. The role of rafts in the fibrillization and aggregation of prions. Chem. Phys. Lipids 141, 66–71.
Prusiner, S.B., 1998. The prion diseases. Brain Pathol. 8, 499–513.
Rajion, M.A., McLean, J.G., Cahill, R.N., 1985. Essential fatty acids in the fetal and newborn lamb. Aust. J. Biol. Sci. 38, 33–40.
Rosa, A., Atzeri, A., Deiana, M., Melis, M.P., Loru, D., Incani, A., Cabboi, B., Dessì, M.A., 2011. Effect of aqueous and lipophilic mullet (*Mugil cephalus*) bottarga extracts on the growth and lipid profile of intestinal Caco-2 cells. J. Agric. Food Chem. 59, 1658–1666.
Rosa, A., Scano, P., Atzeri, A., Deiana, M., Mereu, S., Dessì, M.A., 2012. Effect of storage conditions on lipid components and color of *Mugil cephalus* processed roes. J. Food Sci. 77, 107–114.
Schneider, K., Fangerau, H., Michaelsen, B., Raaba, W.H.-M., 2008. The early history of the transmissible spongiform encephalopathies exemplified by scrapie. Brain Res. Bull. 77, 343–355.
SIMCA-P+ (Version 13.0, Umetrics, Umeå, Sweden).
Simons, K., Ehehalt, R., 2002. Cholesterol, lipid rafts, and disease. J. Clin. Invest. 110, 597–603.
Smith, J.D., Greenlee, J.J., Foster, G.H., Nicholson, E.M., 2012. Acetone precipitation of the scrapie agent results in successful recovery of PrP(Sc) but decreased infectivity. J. Agric. Food Chem. 60, 4758–4762.
Vascellari, S., Banni, S., Vacca, C., Vetrugno, V., Cardone, F., Di Bari, M.A., La Colla, P., Pani, A., 2011. Accumulation and aberrant composition of cholesteryl esters in scrapie-infected N2a cells and C57BL/6 mouse brains. Lipids Health Dis. 10, 132.
Verity, N.C., Mallucci, G.R., 2011. Rescuing neurons in prion disease. Biochem. J. 433, 19–29.
Yun, S.W., Gerlach, M., Riederer, P., Klein, M.A., 2006. Oxidative stress in the brain at early preclinical stages of mouse scrapie. Exp. Neurol. 201, 90–98.

Chapter 2, part 2
Rapid *antemortem* detection of CWD prions in deer saliva by RT-QuIC

Chronic wasting disease

Chronic wasting disease (CWD) is a prion disease that affects cervids such as mule deer (*Odocoileus hemionus*), white-tailed deer (*Odocoileus virginianus*), Rocky Mountain elk (*Cervus elaphus nelsoni*), and Shira's moose (*Alces alces shirasi*) (Williams and Young 1980; Williams and Young 1982; Baeten et al. 2007). It was officially identified as a new Transmissible Spongiform Encephalopathy (TSE) in 1978 by pathologists Williams and Young (Williams and Young 1980). Since then, it is only known to occur in North America, Canada and in South Korea (Dubè et al. 2006; Kahn et al. 2004; Kim et al. 2005; Williams et al. 2005).

Only few amino acid residues differ in the prion protein gene among cervids (Aguzzi and Polymenidou. 2004; Jewell et al. 2005; O'Rourke et al. 1999). As for other prion diseases, species-specific polymorphisms affect susceptibility to CWD infection. In naturally infected mule deer, serine homozygosity at codon 225 seems to increase risk for CWD infection while in Elk risk along with a faster progression of the disease is associated with polymorphism at codon 132 (M/L) (Hamir et al. 2006; O'Rourke et al. 2007). White-tailed deer also have a polymorphism at *Prnp* codon 96 (S/G) (Johnson et al. 2006). In naturally infected white-tailed deer, deer that expressed 96SS PrP had a lower risk for CWD infection, but were not resistant (Johnson et al. 2006; O'Rourke et al. 2004). Other studies suggest that the 96S allele delays CWD disease progression (Wolfe et al. 2007). Perhaps these two allelic genotypes select for different CWD strains.

CWD is characterized by very efficient horizontal transmission among cervids (Miller and Williams 2003) but not towards other species human included (Mawhinney et al. 2006). Mechanism of spreading range from direct contact among animals to environmental exposure; blood, urine, saliva and feces from infected animals have been shown to contain infectivity (Haley et al. 2009; Mathiason et al. 2006; Tamguney et al. 2009) and prion infectivity has been recovered from soil more than 2 years after exposure; therefore, other than cervids, also tainted soil represent a reservoir for CWD prions (Seidel et al. 2007).

Clinical signs of CWD in deer and elk are unspecific and subtle in early disease and commonly include weight loss and behavioral changes such as isolation from the herd and depression. Other signs may include hypersalivation, polydipsia/polyuria, ataxia, and occasionally increased regurgitation and/or esophageal distension.

Background and Rationale

The social behavior of some susceptible cervids drives them to congregate in herds that can seasonally migrate through wide areas. This behavior combined to the ease in horizontal transmission makes keeping track of the new cases fundamental. At the moment, the detection tools used to detect CWD are laborious, impractical, especially for a wildlife screening approach, and time-consuming. The examinations usually include immunohistochemistry, western blotting and PMCA of tonsil and rectal (RAMALT) biopsies or retropharyngeal lymph nodes (Sigurdson 2008).

From the end of May 2012 until November 2013 I had the chance to spend part of my Ph.D. program at the Rocky Mountain Laboratories, a NIH facility located in Hamilton (Montana, USA). I worked under Dr. Byron Caughey supervision.

In 2008, Dr. Caughey's group developed a new *in vitro* amplification assay for prions called "QuIC" (Quaking-Induced Conversion) (Atarashi et al. 2008); I worked with the evolution of the QuIC assay, called RT-QuIC (Atarashi et al. 2011).

RT-QuIC assay is a very promising and powerful tool in the detection of abnormal form of prion protein. So far, it has been successfully applied to several prion diseases like sporadic Creutzfeldt-Jakob disease (sCJD) (Atarashi et al. 2011), variant CJD (vCJD) (Orrù et al. 2011), genetic human prion diseases (Sano et al. 2013) and CWD (Henderson et al. 2013).

In the RT-QuIC assay, soluble recombinant PrP (rPrP-sen) expressed in E. coli is used as a substrate to amplify the minute amounts of abnormal PrP. We know that when the aberrant form of the prion protein gets in contact with the normal one it can induce the misfolding. The conversion is normally very slow, in the RT-QuIC it is enhanced by vigorous intermittent shaking which induces the misfolding of rPrP-sen and therefore the aggregations and formation of fibrils. The formation of the amyloid fibrils is then monitored/detected using thioflavin T (ThT) that specifically binds amyloid becoming fluorescent. It is called Real Time because it is possible to check the reaction step by step, reading the fluorescence at specific time points. (Fig. 1).

RT-QuIC assay is opening the road for new peripheral samples otherwise difficult or unsuitable to test with other methods. This assay appears to be more convenient than others nowadays in use from several points of view; high sensitivity and specificity, user-friendly (extremely easy to set up and repeat) and high-throughput.

During the last months I worked on the setting up of the RT-QuIC assay to detect salivary prions in CWD positive white tail deer (WTD) which could be a sensitive, specific, and rapid ante-mortem test for accurate diagnosis of CWD.

This work was recently published by *Plos One* (see following article).

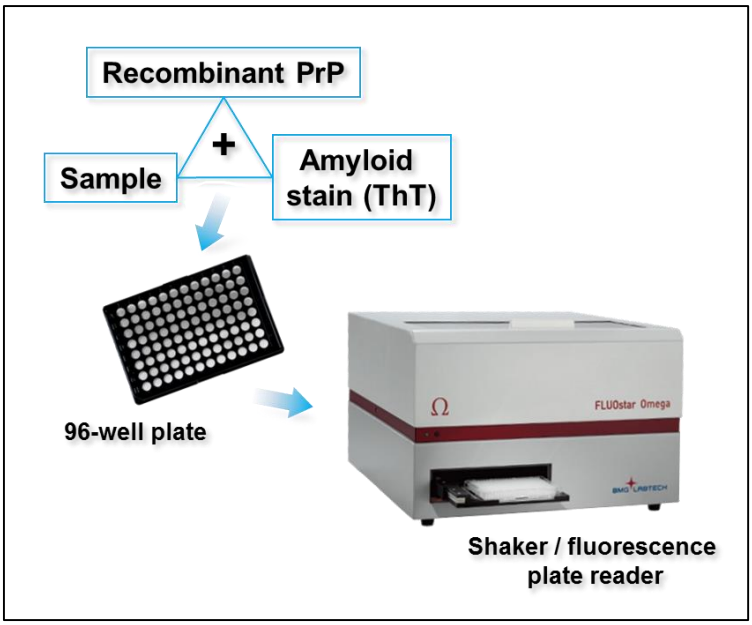

Figure 1. RT-QuIC assay main features.

OPEN ACCESS Freely available online

PLOS ONE

Rapid Antemortem Detection of CWD Prions in Deer Saliva

Davin M. Henderson[1☯], Matteo Manca[2,3☯], Nicholas J. Haley[1], Nathaniel D. Denkers[1], Amy V. Nalls[1], Candace K. Mathiason[1], Byron Caughey[2], Edward A. Hoover[1*]

1 Department of Microbiology, Immunology and Pathology, College of Veterinary Medicine and Biomedical Sciences, Colorado State University (CSU), Fort Collins, Colorado, United States of America, **2** Laboratory of Persistent Viral Diseases, Rocky Mountain Laboratories (RML), National Institute of Allergy and Infectious Disease, Hamilton, Montana, United States of America, **3** Department of Biomedical Sciences, University of Cagliari, Monserrato, Italy

Abstract

Chronic wasting disease (CWD) is an efficiently transmitted prion disease of cervids, now identified in 22 United States, 2 Canadian provinces and Korea. One hallmark of CWD is the shedding of infectious prions in saliva, as demonstrated by bioassay in deer. It is also clear that the concentration of prions in saliva, blood, urine and feces is much lower than in the nervous system or lymphoid tissues. Rapid *in vitro* detection of CWD (and other) prions in body fluids and excreta has been problematic due to the sensitivity limits of direct assays (western blotting, ELISA) and the presence of inhibitors in these complex biological materials that hamper detection. Here we use real-time quaking induced conversion (RT-QuIC) to demonstrate CWD prions in both diluted and prion-enriched saliva samples from asymptomatic and symptomatic white-tailed deer. CWD prions were detected in 14 of 24 (58.3%) diluted saliva samples from CWD-exposed white-tailed deer, including 9 of 14 asymptomatic animals (64.2%). In addition, a phosphotungstic acid enrichment enhanced the RT-QuIC assay sensitivity, enabling detection in 19 of 24 (79.1%) of the above saliva samples. Bioassay in Tg[CerPrP] mice confirmed the presence of infectious prions in 2 of 2 RT-QuIC-positive saliva samples so examined. The modified RT-QuIC analysis described represents a non-invasive, rapid ante-mortem detection of prions in complex biologic fluids, excreta, or environmental samples as well as a tool for exploring prion trafficking, peripheralization, and dissemination.

Citation: Henderson DM, Manca M, Haley NJ, Denkers ND, Nalls AV, et al. (2013) Rapid Antemortem Detection of CWD Prions in Deer Saliva. PLoS ONE 8(9): e74377. doi:10.1371/journal.pone.0074377

Editor: Ilia V Baskakov, University of Maryland School of Medicine, United States of America

Received June 11, 2013; **Accepted** July 31, 2013; **Published** September 11, 2013

Funding: Supported by NIH NINDS grant R01 NS-061902 and by grant D12ZO-045 from the Morris Animal Foundation. This work was also supported in part by the Intramural Research Program of the NIAID. We gratefully acknowledge the Sardinia Regional Government for the financial support of Matteo Manca through his Ph.D. scholarship (P.O.R. Sardegna F.S.E. Operational Programme of the Autonomous Region of Sardinia, European Social Fund 2007-2013). The funders had no role in study design, data collection and analysis, decision to publish, or preparation of the manuscript.

Competing interests: The authors have declared that no competing interests exist.

* E-mail: Edward.Hoover@colostate.edu

☯ These authors contributed equally to this work.

Introduction

Chronic Wasting Disease (CWD) is a transmissible spongiform encephalopathy (TSE), or prion disease, that affects free-ranging and captive cervids [1,2]. CWD appears to be the most transmissible of the prion diseases, and is now recognized in twenty-two U.S. states, as well as two Canadian provinces and the Republic of Korea (http://www.nwhc.usgs.gov/). Experimental studies have demonstrated that CWD prions can also infect several outbred non-cervid species [3–9]. Thus the emerging prevalence of CWD poses a challenge to wildlife management agencies, free-ranging and captive cervid populations, the hunting and food producing animal economies, and may pose a zoonotic risk. Ideally, monitoring for CWD prions would be carried out on minimally invasive biologic samples (such as saliva, blood, urine or feces) harvested from live animals in the field. However, rapid, sensitive and specific ante-mortem detection of CWD and other prion diseases remains a challenge due to the low concentrations of prions and the presence of inhibitors in body fluids and excreta [10–13].

The salient feature of prion disease is the conversion of the normal cellular prion protein (PrP^{C}) to a misfolded, pathogenic and transmissible form, often designated as PrP^{Res}, PrP^{Sc}, or PrP^{D} [14–16]. The normal prion protein (PrP^{C}), expressed at highest level in the central nervous system [17,18], is composed of ~250 amino acids with a predominantly unfolded N-terminal region and a C-terminal domain that is folded, globular, and contains three α-helices and two short β-sheet stretches [19,20]. The formation of the misfolded pathogenic

prion is thought to occur through PrP^{Res}-templated conversion of the predominantly α-helical C-terminal region of PrP^{C} to a high β-sheet oligomeric conformer, thereby conferring partial protease resistance [21–23]. The degree of protease-resistance of PrP^{Res} varies markedly from oligomers to large amyloid fibrils, with the smaller particles tending to be more infectious per unit protein [24]. Bioassay studies in deer have demonstrated infectious prions in the saliva, urine, blood and feces of infected deer [25–27]. However, due to the low concentration of PrP^{Res} detectable in biological fluids or excreta and the potential that the infectious prions may be relatively protease-sensitive, the timing, source and biochemical nature of peripheralized/excreted prions remain poorly understood. Thus, detection of the low levels of prion protein in body fluids will likely require *in vitro* amplification such as that provided by serial protein misfolding cyclic amplification (PMCA) [28–31]. PMCA has been very successfully applied to tissue samples, however, detection of prions in some body fluids has been hampered by the presence of inhibitors in biological fluids and excreta. Nevertheless, the detection of scrapie prions by multiple rounds of PMCA performed on oral swab eluates from scrapie-infected sheep [32] and blood of hamsters [29] has demonstrated the potential for detection of very low levels of prions in body fluids through in vitro amplification methods.

Real-time quaking conversion (RT-QuIC) [33,34] relies on the seeded conversion of recombinant PrP^{C} to a thioflavin T (ThT)-binding amyloid-like PrP form and offers the potential for sensitive ante-mortem detection of prions in a single round assay [35,36]. Here we report adaptations of RT-QuIC to detect CWD prions in the saliva of CWD-exposed pre-symptomatic and symptomatic deer. These data support the promise of RT-QuIC methodology both for sensitive prion detection in live animals and as a means to help elucidate the mechanisms of prion conversion, peripheralization and transmission.

Materials and Methods

Expression and purification of rPrP

RT-QuIC assays were performed with recombinant Syrian hamster PrP (SHrPrP) encoding residues 90-231 in Pet 41 and expressed and purified as previously described [34]. In brief, 1 liter cultures of LB containing Auto Induction™ supplements (EMD Biosciences) were inoculated with SHrPrP expressing Rosetta strain *E. coli*, grown overnight, and harvested when OD (600 nm) of ~3 was reached. Cells were lysed with Bug Buster™ reagent with supplemented Lysonase™ (EMD Biosciences) and inclusion bodies (IB) were harvested by centrifugation of the lysate at 15,000 x g. IB pellets were washed twice and stored at -80 °C until purification (typically 24 hours or less). IB pellets were solubilized in 8 M guanidine hydrochloride (GuHCl) in 100 mM $NaPO_4$ and 10 mM Tris pH 8.0, clarified by centrifugation at 15,000 x g for 15 min and added to Super Flow Ni-NTA resin (Qiagen) pre-equilibrated with denature buffer (6.0 M GuHCl, 100 mM $NaPO_4$, 10 mM Tris pH 8.0). Denatured SHrPrP and Ni-NTA resin was incubated by rotating at room temperature for 45 min and then added to an XK FPLC column (GE Healthcare). Refolding was achieved on column using a linear refolding gradient of denature buffer to refold buffer (100 mM $NaPO_4$, 10 mM Tris pH 8.0) over 340 ml at 0.75 ml/min. SHrPrP was eluted with a linear gradient of refold buffer to elution buffer (100 mM NaPO4, 10 mM Tris pH 8.0 500 mM imidazole pH 5.5) over 100 ml at 2.0 ml/min. Fractions were pooled and dialyzed against two changes of 4.0 l dialysis buffer [20 mM $NaPO_4$ pH 5.5 (CSU); 10 mM $NaPO_4$ pH 5.8 (RML)]. SHrPrP was adjusted to ~0.5 mg/ml, aliquoted, snap frozen in liquid nitrogen, and then stored at -80 °C.

Animals and samples

All animals were handled in strict accordance with guidelines for animal care and use provided by the United States Department of Agriculture (USDA), National Institutes of Health (NIH) and the Association for Assessment and Accreditation of Laboratory Animal Care International (AAALAC), and all animal work was approved by Colorado State University Institutional Animal Care and Use Committee (IACUC approval numbers 02-151A, 08-175A, 09-1463A, 10-1766A, 10-2189A, 11-2622A and 12-3773A).

The CWD-naïve, hand-raised, human- and indoor-adapted white-tailed deer fawns were sourced from the Warnell School of Forestry, University of Georgia as part of longstanding collaborations with David Osborn, Sallie Dahmes, Carl Miller and Robert Warren. The deer were housed in indoor barrier-maintained pens at the Colorado State University CWD Research Facility at the Foothills Campus. As part of CWD transmission, pathogenesis, and vaccination studies, they were exposed to CWD prions contained in various inoculation materials delivered by various routes (Table 1). Saliva samples were collected via syringe aspiration or direct tube collection predominantly from anesthetized deer and stored at -80 °C until thawing and dilution for the assays described. The majority of samples forming the basis of this report were analyzed independently using the same QuIC protocols in the CSU and NIAID/Rocky Mountain laboratories by the first two authors of this report (Table S1). Deer were classified clinically (Table 1) as: (a) pre-clinical—either no symptoms of CWD or behavioral changes sufficiently subtle as to be detectable only by observers experienced with each animal and its demeanor; (b) clinical—varying levels of clinical CWD signs were present, including: weight loss of >10% peak weight, behavioral changes (e.g. postural changes, fixed staring, repetitive motions, aggression or withdrawal), increased frequency of food or water consumption, incoordination, salivation.

Diluted saliva RT-QuIC assay

The substrate for seeded RT-QuIC reactions was prepared by adding SHrPrP to RT-QuIC reaction buffer composed of 50 mM $NaPO_4$, 320 mM NaCl, 1.0 mM ethylenediaminetetraacetic acid tetrasodium salt (EDTA), 10 μM Thioflavin T (ThT, Sigma) to a final concentration of 0.1 mg/ml. The substrate was added to optical bottom black 96-well plates (Nunc) with either 98 μl for brain homogenate samples or 95 μl for 1:10 dilution (Dilution buffer: 0.1% SDS in PBS pH 7.4) saliva samples. 2 μl of CWD positive or negative control brain samples diluted from 10^{-4} to 10^{-8} were added to substrate on each plate. Five μl of 1:10 diluted saliva was added in quadruplicate to substrate

Table 1. Summary of white-tailed deer sample status and RT-QuIC results.

Animal Number	Diluted Saliva	PTA Saliva	Animal Inoculum	Route	PrP^{Res} IHC#	Disease State
108	0/8	0/8	CWD(+) Blood	IP/IV	+	Terminal
112	1/8	8/8	CWD(+) Brain	PO	+	Clinical
121	2/8	8/8	CWD(+) Brain	IC	+	Terminal
132	0/8	8/8	CWD(+)Saliva	PO	+	Terminal
133	5/8	8/8	CWD(+) Blood	IV	+	Clinical
136	0/8	6/8	CWD(+) Brain	PO	+	Terminal
137	0/8	4/8	CWD(+) Blood	IV	+	Clinical
138	3/8	10/12	CWD(+) Brain	PO	+	Clinical
143	0/8	1/8	CWD(+) Brain	PO	+	Terminal
144	3/8	8/8	CWD(+)Saliva	PO	+	Terminal
773	0/8	3/8	CWD(+) Brain	PO	+	Pre-Clinical
775	1/8	0/8	CWD(+) Brain	PO	+	Pre-Clinical
776	0/8	8/8	CWD(+) Brain	PO	+	Pre-Clinical
777	1/8	2/12	CWD(+) Brain	PO	+	Pre-Clinical
778	1/8	12/12	CWD(+) Brain	PO	+	Pre-Clinical
780	0/8	1/8	Ovine Scrapie (+) Brain	IV	+	Pre-Clinical
781	0/8	0/8	CWD(+) Brain	PO	+	Pre-Clinical
785	1/8	12/12	CWD(+) Brain	PO	+	Pre-Clinical
812	1/8	0/8	CWD(+) Brain	Aerosol	+	Pre-Clinical
813	0/8	16/16	CWD(+) Brain	Aerosol	+	Pre-Clinical
815	1/8	8/8	CWD(+) Brain	Aerosol	+	Pre-Clinical
816	3/8	0/8	CWD(+) Brain	Aerosol	+	Pre-Clinical
817	1/8	6/8	CWD(+) Brain	Aerosol	+	Pre-Clinical
818	1/8	2/8	CWD(+) Brain	Aerosol	+	Pre-Clinical
810	0/8	0/8	(-) Brain	Aerosol	-	N.A.
814	0/8	0/8	(-) Brain	Aerosol	-	N.A.
819	0/8	0/16	(-) Brain	Aerosol	-	N.A.
103	0/8	0/8	(-) Multiple*	Var. Routes	-	N.A.
123	0/8	0/8	(-) Multiple*	Var. Routes	-	N.A.
502	0/8	0/12	(-) Urine & Feces	PO	-	N.A.
504	1/8	1/8	(-) Urine & Feces	PO	-	N.A.

Summary of animals, inocula and route of infection, sample collection relative to clinical status, and RT-QuIC results. The number of replicates positive from up to 3 experiments is reported for both 1:10 diluted saliva and PTA treated saliva. Definitions: Pre-clinical—either no symptoms of CWD or behavioral changes sufficiently subtle as to be detectable only by observers experienced with each animal and its demeanor; Clinical—varying levels of clinical CWD signs were present, including: weight loss of >10% peak weight, behavioral changes (e.g. postural changes, fixed staring, repetitive motions, aggression or withdrawal), increased frequency of food or water consumption, incoordination, salivation. Inocula abbreviations: intraperitoneal (IP), orally (PO), intravenously (IV), Intracranially (IC). (*) Animals received multiple (-) inocula. Each received CWD (-) blood IP, CWD (-) urine, feces and saliva PO and CWD (-) white-tailed deer brain IC.

doi: 10.1371/journal.pone.0074377.t001

wells for each assayed saliva sample. Each saliva sample was assayed in quadruplicate wells at least twice using independently set up substrate reaction mixes. Prepared plates were placed in a BMG Labtech Polarstar™ fluorometer and subjected to 700 rpm double-orbital shaking for one minute every other minute for 15 minutes. After each shaking cycle ThT fluorescence was read at an excitation of 450 nm and emission of 480 nm. Gain was set at 1700 for 1:10 dilution saliva samples and read using orbital averaging with 20 flashes per well with the 4 mm setting. The substrate was replaced after 24 hours by removing 100 µl from each well. A residual amount of liquid remained in each well and a high percentage of the ThT fluorescence. Fluorescent readings were recorded for all sample reactions for a total time of 48 hours at a temperature of 42 °C.

PTA saliva RT-QuIC assay

In order to concentrate CWD prions and avoid the assay inhibition factors in saliva, 100 µl of each sample was shaken for 1 hour at 1500 rpm and 37 °C (Eppendorf Thermomixer R) in the presence of 0.28% (w/v) phosphotungstic acid (PTA, Sigma) at pH 7.4. After a 30-min spin at 16100 x g at 23 °C, the pellet was resuspended in 10 µl of 0.1% (w/v) SDS/PBS and used as seed for the RT-QuIC reaction.

RT-QuIC reaction substrate composition was as follows: 10 mM phosphate buffer (pH 7.4), 300 mM NaCl, 0.1 mg/ml SHrPrP, 10 µM ThT, and 1 mM EDTA. Ninety-eight µl of substrate was loaded into wells of a black 96-well plate with a clear bottom (Nunc) and seeded with a 2 µl seed sample for a final reaction volume of 100 µl. All reactions contained equivalent final concentrations of SDS (0.002%). The plates were sealed with a plate sealer film (Nalgene Nunc International), and then incubated in BMG Labtech FLUOstar™ plate reader at 46 °C for 65 hours with cycles of 1 min shaking (700 rpm double orbital) and 1 min rest throughout the incubation. ThT fluorescence measurements (450 +/-10 nm excitation and 480 +/-10 nm emission; bottom read, 20 flashes per well, manual gain of 2300, and 20 ms integration time) were taken every 45 min.

Mouse inoculation studies

Four milliliters of saliva was collected from two experimentally exposed white-tailed deer (deer #133, 12mos post-inoculation, and 144, 27mos post-inoculation) and one sham exposed white-tailed deer (123). Saliva samples were lyophilized using a LabConco lyophilizer, resuspended in 0.4 ml of PBS and dialyzed against PBS to return the samples to isotonicity. Four milliliters of saliva from a negative control deer (deer 123) was prepared concurrently in a similar fashion. Three groups of Tg[CerPrP] 5037 mice [37] (n=9 mice/group) were sedated using an intraperitoneal (IP) injection of 500 µl of ketamine (10 mg/ml) and xylazine (1 mg/ml), and inoculated intracranially (IC) with 30 µl of the concentrated saliva preparation. Each group was inoculated with concentrated saliva from a single source animal (#133, 144, or 123). Following inoculation, mice were monitored daily over the course of disease for evidence of prion infection (incoordination, weight loss, etc.) and humanely euthanized

when necessary. Following euthanasia, the left hemisphere of the brain was removed and analyzed for the presence of PrP^{Res} by western blotting.

Western blotting

The left hemisphere of each cervid brain was divided into 8 rostral to caudal sections for analysis by western blotting. The most rostral region of all 8 slices was prepared as a 10% homogenate suitable for western blotting. Each sample was processed with and without proteinase K (PK; 30 μg/ml) addition for 30 min at 37 °C shaking at 850 rpm. After PK treatment samples were electrophoresed in 12% SDS-PAGE gel (Biorad), transferred to PVDF with the Trans-Blot Turbo semi-dry transfer apparatus (Biorad). Membranes were processed with the Snap-ID™ western blot instrument (Millipore), blocked with Snap-ID blocking reagent (Millipore), and probed with BAR-224-HRP conjugated antibody at a concentration of 1:5000. HRP blots were developed with Pierce ECL-plus™ reagent (Thermo Scientific) and imaged on an Image-Quant LAS-4000™ imager (GE Scientific).

End-point dilution analysis

End-point dilution analysis was performed as follows. Two microliters of 10^{-7}, 10^{-8} and 10^{-9} CWD-positive and 10^{-7} normal deer brain homogenate in dilution buffer were loaded into the RT-QuIC reaction. For each dilution, 12 replicates wells were seeded. Three aliquots (100 μl) of each CWD negative and positive brain homogenate dilutions were PTA precipitated and PTA pellets resuspended in 10 μl of 0.1% (wt/vol) SDS/PBS; 4 wells were seeded with 2 μl of each PTA pellet. RT-QuIC and PTA precipitation were performed as described in PTA saliva RT-QuIC paragraph, Materials and Methods section.

Results

RT-QuIC can detect CWD prion seeds in a 1:10 dilution of saliva

Our first goal was to employ the RT-QuIC method for detection of CWD prions in diluted saliva from CWD-inoculated deer. We initially assayed saliva samples diluted from 10^{-1} to 10^{-3}. No sample diluted past 10^{-1} yielded a positive result in the RT-QuIC assay, inferring, consistent with previous bioassay studies, a relatively low concentration of prions relative to tissue sources. Nevertheless, we identified a number of saliva samples which at 1:10 dilution in dilution buffer were routinely positive with RT-QuIC. In each of two experiments multiple replicates of these saliva samples were positive with magnitudes and kinetics equivalent to 10^{-6} to 10^{-8} dilutions of CWD positive brain homogenate (Figures 1 and 2). Saliva samples were deemed positive if the average end-point ThT fluorescence of four replicate wells was 3 standard deviations greater than the average fluorescence of the negative control saliva samples. The threshold for positivity with 1:10 diluted saliva, and for PTA-precipitated saliva (see below), was calculated based on the negative controls performed for each method. However, diluted saliva samples from 5 of 10 animals that were known to have clinical CWD symptoms and tonsil or rectal lymphoid tissues positive for CWD PrP^{Res} by immunohistochemistry or western blot were not positive by RT-QuIC (Figure 1 and Table 1). While this could represent the heterogeneity inherent in single time point saliva collections, we nevertheless sought to enhance the salivary RT-QuIC sensitivity without introducing complex concentration methods.

PTA/RT-QuIC enhances detection of CWD prion seeds in saliva

With the goal of enhancing the sensitivity of CWD prion detection in saliva (~50% in known infected deer, Table 1) without compromising specificity or introducing cumbersome methodologies, we added pre-assay phosphotungstic acid (PTA) precipitation of saliva samples to the RT-QuIC protocol. PTA precipitation of CWD positive brain spiked into deer saliva samples decreased the lag phase of RT-QuIC reactions (Figure 3A) and increased sensitivity by approximately one order of magnitude (Figure 3B). None of the wells seeded with normal deer brain homogenate or their 3 independently PTA precipitated counterparts gave ThT positivity, showing that the unseeded SHrPrP was stably non-amyloidogenic within the RT-QuIC conditions we used (NaCl 300-320 mM, 42-46 °C, 65 hrs) and that the PTA precipitation protocol per se did not lead to false positive results (Figure 3 A and B). PTA precipitation also reduced spontaneous conversion seen with some undiluted negative control saliva samples, potentially by eliminating or reducing reaction competitors or inhibitors found in saliva, blood and urine. With the addition of PTA precipitation, the same saliva samples from the above group of clinically ill animals retained the same specificity and increased sensitivity from 50 to 90% (5/10 to 9/10) (Figure 1 and Table 1). Both RT-QuIC assay methods showed only a single apparent false positive replicate out of 56 for 1:10 diluted samples and 1 of 68 for PTA precipitation. Each method detected the false positive in the same saliva sample, which likely reflects a predisposition of that sample to cause spontaneous conversion due to contaminants such as rumen or fomites.

RT-QuIC-positive saliva samples contain infectious prions

To establish that saliva samples positive for CWD prion seeds by RT-QuIC assay contained authentic infectious CWD prions, transgenic mice expressing normal cervid PrP^{C} (Tg[CerPrP] 5037 mice) [37] were inoculated intracranially with the same saliva samples tested by RT-QuIC from two of the above deer (#133 and 144 from Figure 1). Mice inoculated with each positive saliva sample developed clinical symptoms of TSE as early as ~300 days post-inoculation (dpi) and 50% of the mice were euthanized due to signs attributed to prion infection by 500 dpi, as confirmed by western blotting for PrP^{Res} (Figures 4 and S1). Mice inoculated in the same manner with saliva from an uninfected animal did not develop clinical TSE symptoms nor was PrP^{Res} detectable by western blot (Figures 4 and S1).

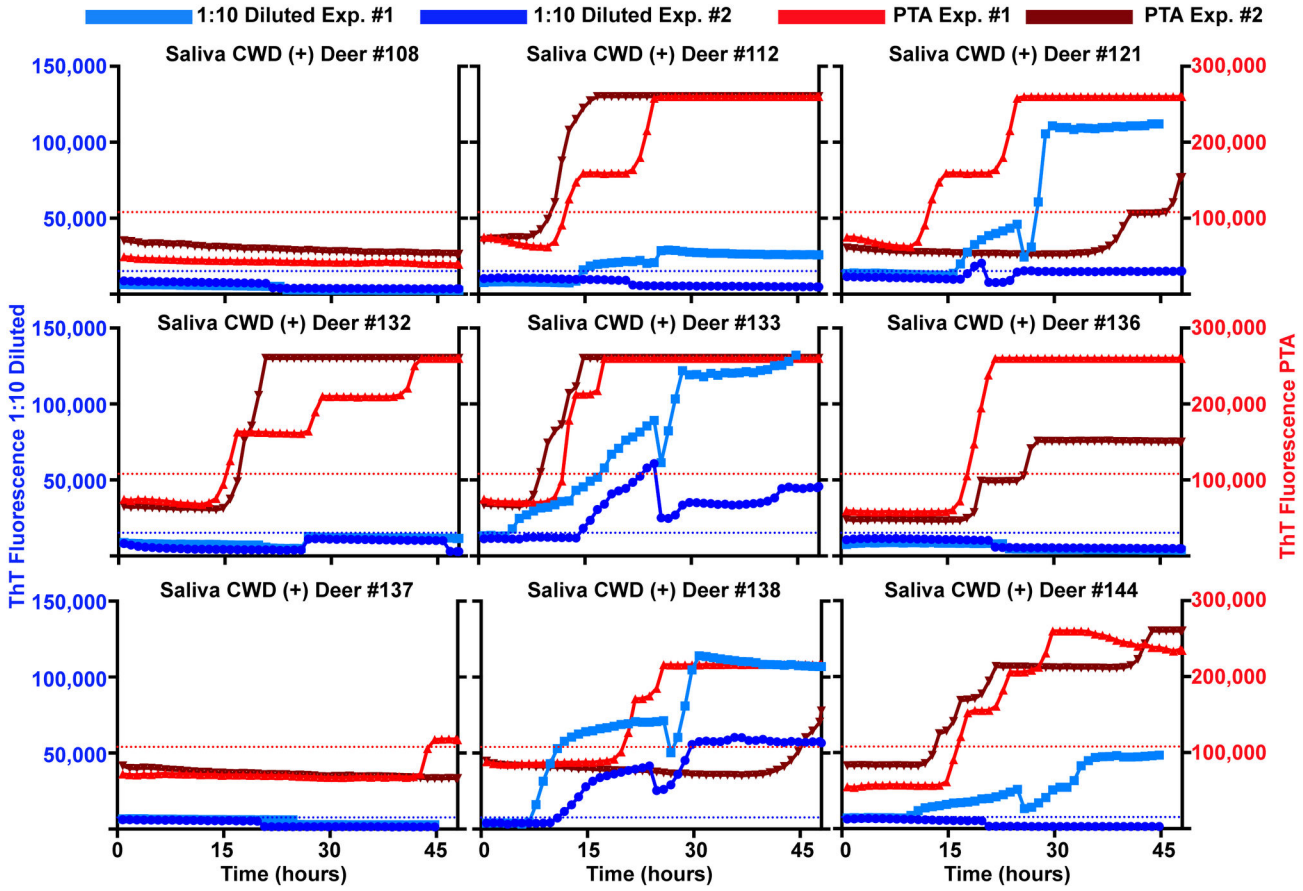

Figure 1. RT-QuIC analysis of CWD-positive clinically ill white-tailed deer. Both 1:10 diluted and PTA precipitated saliva show positive results by RT-QuIC. Each line represents an individual experiment with the average of four replicates. Blue and light blue lines represent 1:10 diluted saliva experiments and red and dark red lines represent PTA precipitated counterpart of the same saliva samples. The left axis (blue) denotes ThT fluorescence for 1:10 diluted saliva samples and the right axis (red) denotes ThT fluorescence for PTA saliva samples. Dashed lines represent threshold for a positive sample. Blue for 1:10 diluted saliva experiments and red for PTA saliva experiments. Positive RT-QuIC results were observed for saliva from clinically ill white-tailed deer in 5 of 9 1:10 diluted saliva samples and 8 of 9 PTA precipitated saliva samples. Each saliva sample was from an individual deer.

doi: 10.1371/journal.pone.0074377.g001

RT-QuIC-based detection of prion shedding in pre-clinical deer

One of our research goals was to establish/develop a non-invasive means to monitor the peripheralization and excretion of prions throughout the CWD disease course. Using parallel analysis of the same saliva samples tested by both 1:10 dilution and PTA-precipitation from pre-clinical CWD-inoculated white-tailed deer in two laboratories, we detected CWD prion shedding in 64.2% of 1:10 diluted samples and 71.4% of PTA precipitated samples (Figure 5 and Table 1). PTA increased the number of positive well replicates from 9.8% with 1:10 dilution to 53.0% and decreased the time for ThT fluorescence to cross the threshold. However, three samples (deer# 775, 812 and 816) that were not positive by PTA RT-QuIC showed a positive signal in the dilution tested samples (Figure 5 and Table 1). These differences may reflect degradation of protease sensitive material during the PTA protocol since no protease inhibitors are used but more work will be necessary to understand the mechanism.

Correlation of salivary shedding with magnitude of prion dissemination in brain

In the course of analyzing both pre-clinical and terminal saliva samples from white-tailed deer, we observed that saliva from some animals produced more robust and consistent positive results by both the PTA and 1:10 diluted RT-QuIC protocols. Because terminal brain was available from most animals, we compared prion dissemination and burden, estimated by western blotting of 8 rostral to caudal brain slices from deer after they had developed terminal disease to RT-QuIC results from the preclinical stage of disease (Figure 6A, B and S2). Widespread distribution and increased magnitude of

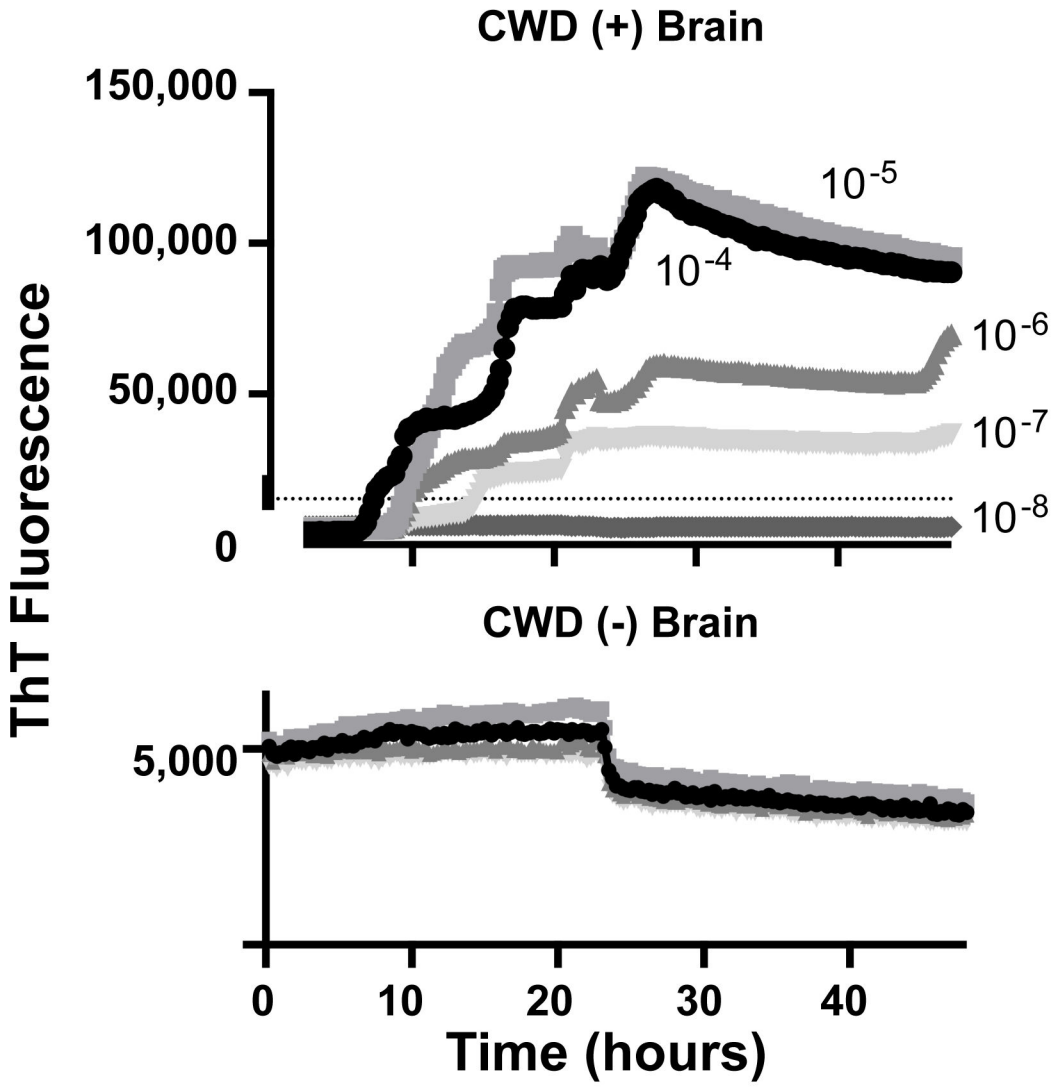

Figure 2. SHrPrP substrate can detect CWD-positive brain over a range of dilutions from 10^{-4} to 10^{-7}. CWD positive and negative brain was serially diluted and analyzed by RT-QuIC assay. Each line for positive CWD samples represents the average of 4 individual wells from 4 independent experiments.

doi: 10.1371/journal.pone.0074377.g002

PrP^{Res} at terminal disease state was often observed for animals with the most RT-QuIC positive saliva replicates during the preclinical stage of disease suggesting a potential correlation between shedding and central nervous system prion load (Figure 6B and S2). Since the western blot data are not quantitative, a strong conclusion regarding direct correlation is not possible, although it would not be surprising that a higher prion load in the brain would lead to higher prion levels shed in saliva.

Discussion

We demonstrate that RT-QuIC can reproducibly detect prions in saliva, a complex biological fluid containing a wide range of complex glycoproteins including proteases [38–40]. Two of two RT-QuIC-positive saliva samples contained infectious prions by Tg[CerPrP] mouse bioassay and PrP^{Res} distribution in the brain seemed to correlate with RT-QuIC positivity. PTA enrichment of CWD prions in saliva increased the percentage of positive replicates from 17.5% in clinical animals tested by dilution of untreated saliva to 72.6% and from 9.8% in diluted saliva from pre-clinical animals to 53.0%. Previous studies by Colby et al. [41] demonstrated that PTA inhibited amyloid amplification in the amyloid seeding assay. Our results suggest that under the present assay conditions PTA precipitation is not inhibitory but rather increases the sensitivity (Figure 3A and B), perhaps by both concentrating the prions from more saliva equivalents and decreasing saliva-associated inhibitory activities (Figure 3A).

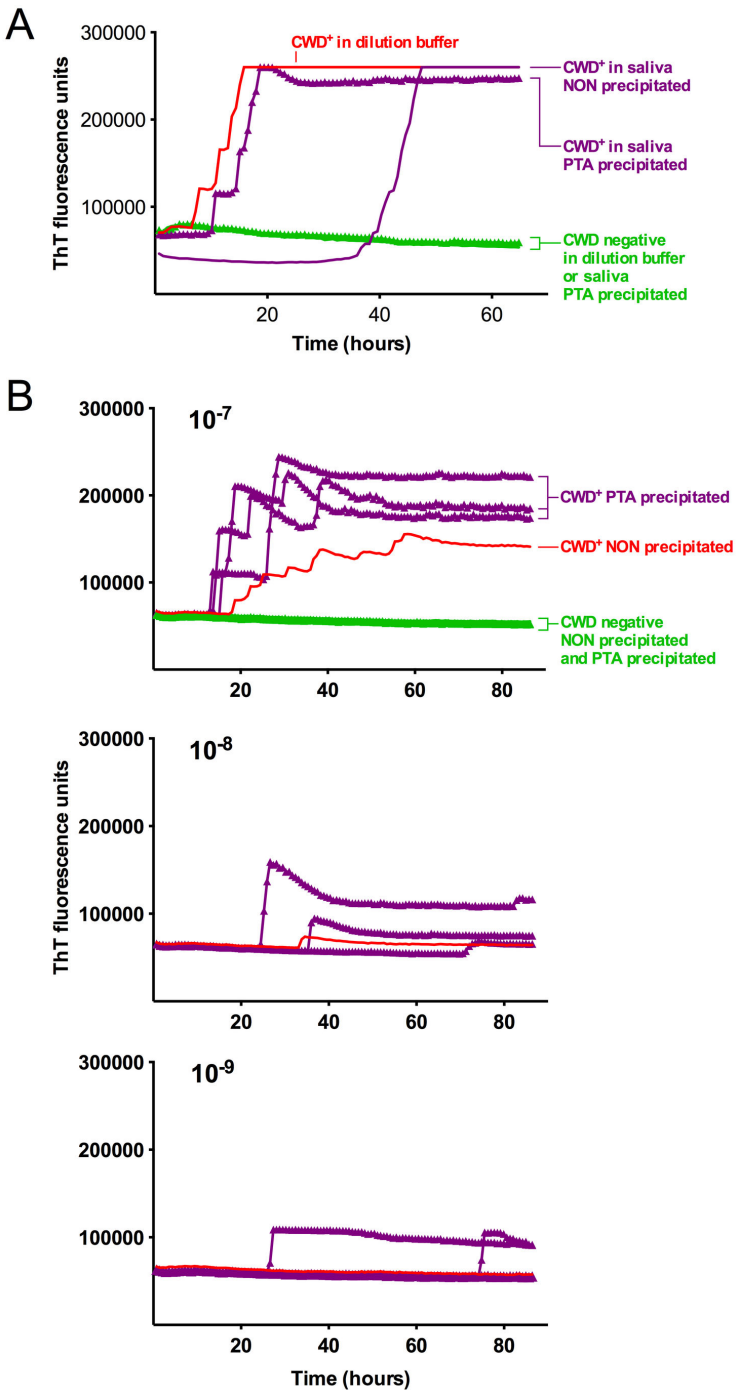

Figure 3. PTA precipitation increases sensitivity of the RT-QuIC assay. A. Each data point shows the ThT fluorescence average of 4 replicate wells loaded with either 2 µl of brain homogenate dilution or PTA pellets from the same brain homogenate equivalents. Lines with triangles represent PTA precipitated samples while smooth lines are non-precipitated counterparts or controls (in the latter case, invisible under the green triangles). The data for spiked PTA precipitated deer saliva (purple triangles) comes from a separate experiment performed under the same experimental conditions. B. End-point dilution analysis of a CWD (+) brain homogenate including 10^{-7} to 10^{-9} dilutions with or without PTA precipitation. PTA precipitated samples were done in triplicate (purple) and represent the ThT fluorescence average of 4 replicate wells each. Non-precipitated samples (red) represent the ThT fluorescence average of all 12 replicate wells. Normal deer brain homogenates (green) are shown for PTA precipitated (3 overlapping curves of data points representing the average of 4 replicate wells) and non-precipitated (average of 12 replicate wells) samples.

doi: 10.1371/journal.pone.0074377.g003

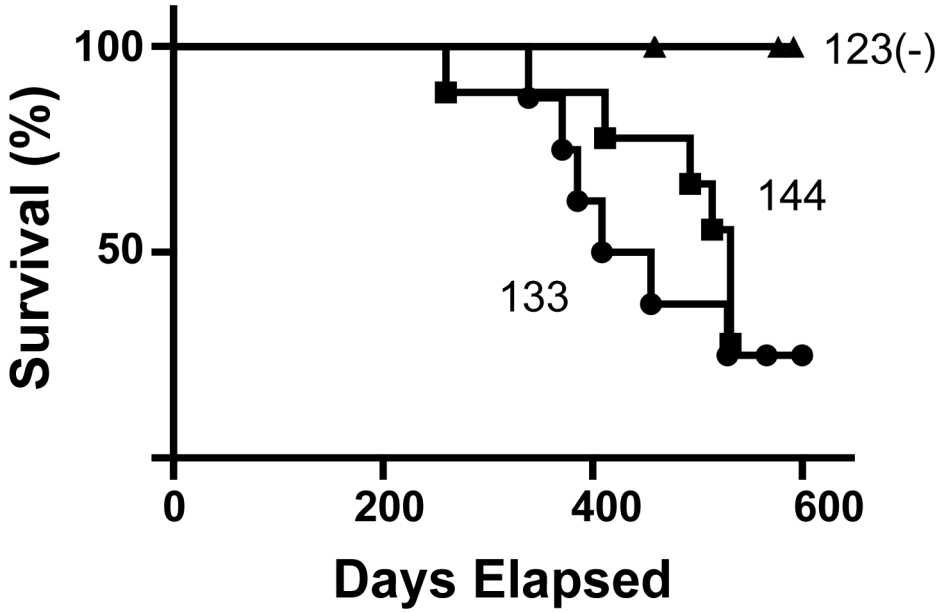

Figure 4. Kaplan-Meier survival curve for mice inoculated with CWD+ saliva. The same saliva samples from deer assayed in Fig. 1 (#133 and 144) were inoculated into cervidized mice (Tg[CerPrP] 5037) as well as saliva from a sham inoculated deer. 50% of mice were euthanized due to clinical disease after ~500 days.
doi: 10.1371/journal.pone.0074377.g004

Horizontal transmission of CWD is exceptionally efficient, which may be why it is the only known prion disease found in a free-ranging animal species [42,43]. Enhanced horizontal transmission may reflect abundant excretion and/or unique yet elusive biochemical features of prions shed by CWD infected deer. Multiple studies have demonstrated that relatively protease sensitive and/or oligomeric conformers of PrP^C are both infectious and perhaps the more pathogenic species in prion disease [44–48]. Elucidating biochemical differences of prions from saliva or excretory products (e.g. nasal secretions) with the help of the RT-QuIC may reveal possible structural or stability differences between prions in the central nervous system and those shed into the environment.

Several studies indicate that the concentration of prions in excreta is very low, thus requiring multiple rounds of amplification in PMCA as well as sample dilution to escape inhibitors [10,29,49,50]. Because RT-QuIC methodology offers the advantages of single cycle amplification, it offers potential for high through-put and reduced contamination risk-advantages for both detection and surveillance in the natural setting and in controlled longitudinal studies of prion pathogenesis and excretion. As estimated by the kinetics and magnitude of RT-QuIC responses, it appears that the concentration range of prions in saliva is approximately equivalent to 10^{-6} to 10^{-8} dilutions of CWD-positive brain. These results reinforce previous studies indicating that RT-QuIC can estimate the relative concentrations of infectious prions in a given sample [34].

Bioassay experiments also indicate that the levels of infectious prions in deer and sheep saliva are similar to near end-point dilutions of prion-infected brain [13,26]. Although complicated by the presence of inhibitors, blood-borne prions have been demonstrated through substantial dilution prior to assay or use antibody capture from plasma to both concentrate seeding activity and escape inhibitors [12,29,30,50]. Conversely, cerebrospinal fluid has been shown to have relatively high levels of prion seeding activity [11,51]. Overall, therefore, the results we report here for saliva using RT-QuIC are consistent with studies thus far employing *in vitro* amplification methods.

However, much as with PMCA, comparing the relative amplification of saliva samples to brain samples or any other sample from tissue or body fluid has a number of caveats. For example, each sample source potentially contains distinct amplification inhibitors, enhancers, as well as other factors that likely influence reaction rate, magnitude, or lag phase. Nevertheless, the comparisons between *in vitro* seeding assays and in vivo infectivity assays increasingly support careful extrapolations.

In summary, RT-QuIC offers sensitivity with relatively rapid single cycle amplification, versatility in application to tissues, biologic fluids, and environmental samples, and potential to define co-factors and inhibitors of prion conversion.

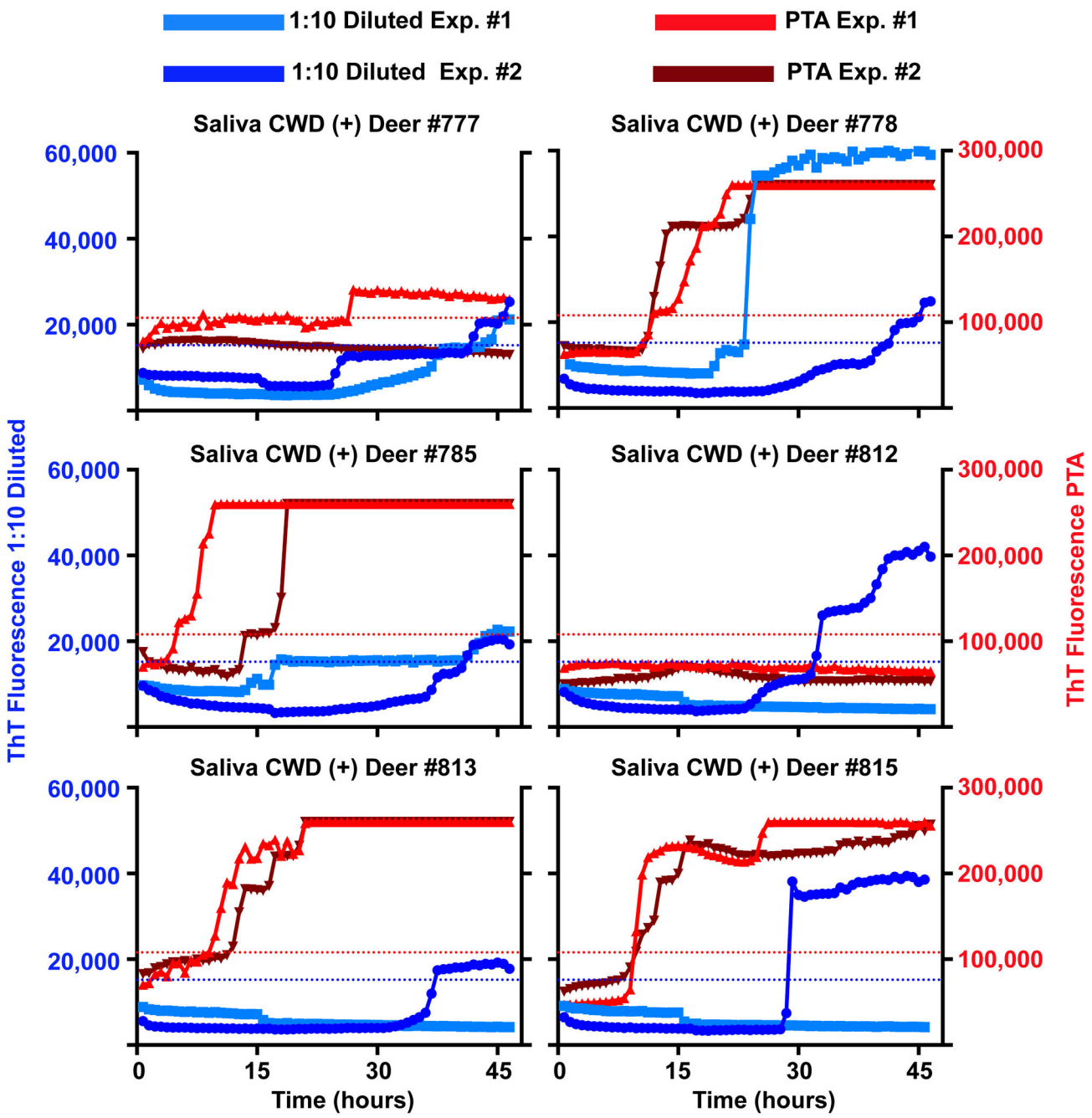

Figure 5. RT-QuIC comparison of diluted saliva vs. PTA precipitated saliva harvested from pre-clinical* white-tailed deer. PTA precipitation of saliva samples increased sensitivity and consistency of RT-QuIC prion detection of pre-clinical white-tailed deer. All colors and axis are the same as in Figure 1. (*) refers to either no signs of CWD or subtle behavioral symptoms detectable only by observers very familiar with individual deer and the very early signs of CWD.

doi: 10.1371/journal.pone.0074377.g005

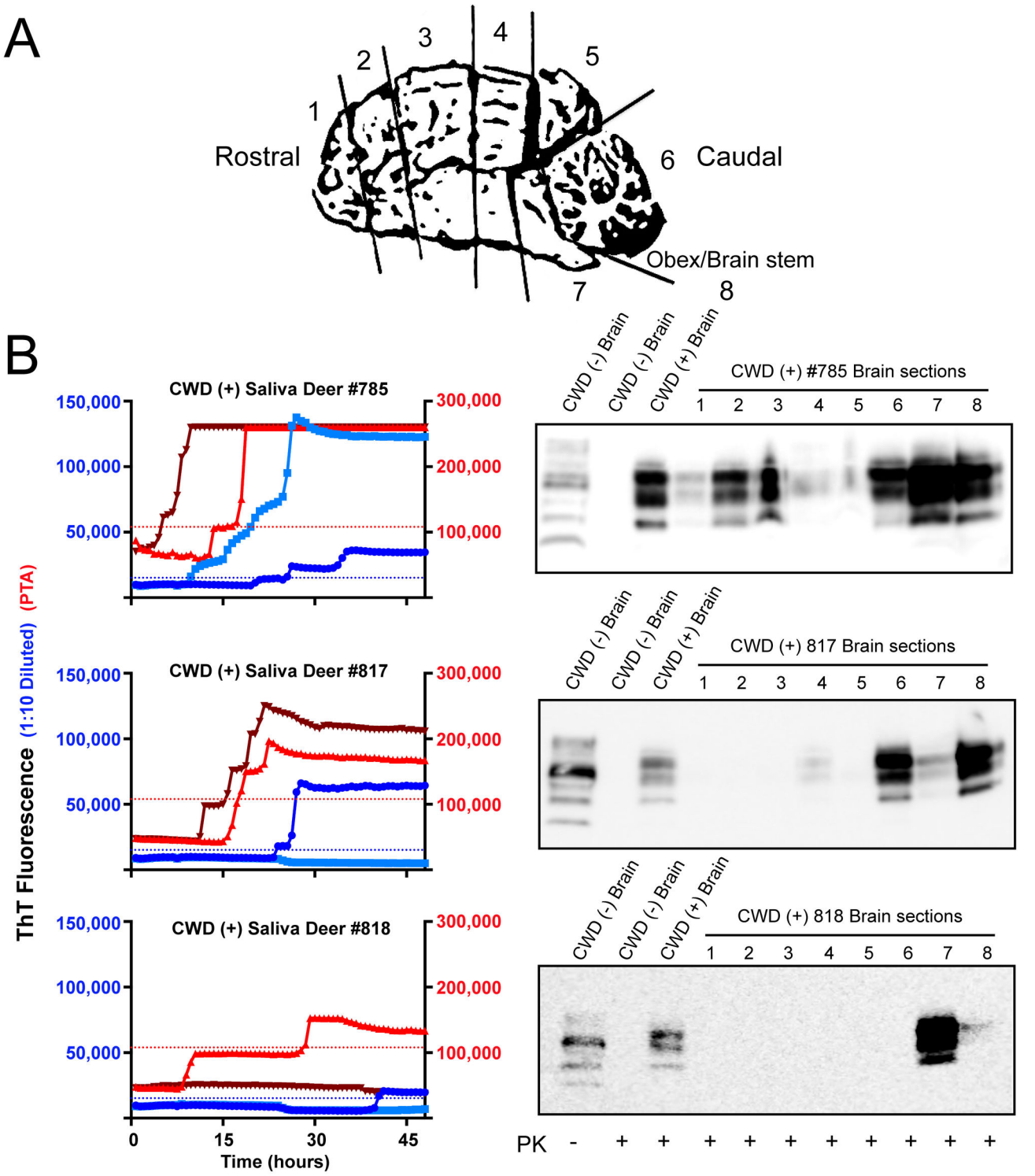

Figure 6. Correlation of RT-QuIC analysis of terminal saliva samples with western blot PrP^{Res} signal in brains. A. Cartoon representation of sections analyzed for PrP^{Res} by western blotting. Seven rostral to caudal sections were analyzed plus the obex/brainstem region. B. (left) RT-QuIC analysis of saliva samples from white-tailed deer. Colors and axis are the same as in Figure 1 (right). Western blot analysis of 8 brain sections including CWD (+) and (-) control samples. PK was added to all samples except one CWD (-) brain sample. Antibody BAR-224-HRP used for detection.

doi: 10.1371/journal.pone.0074377.g006

Supporting Information

Figure S1. Western blot analysis of CWD(+) saliva inoculated Tg[CerPrP] 5037 mice. Lanes 1 and 18 show PrP^C form 10% mouse brain homogenates without PK digestion. Big arrowhead marks location of undigested PrP^C. Lanes 2-17 are PK digested brain homogenates from IC inoculated mice. Lanes 2-5 are brain homogenates from mice IC inoculated with obex from deer #133. Lanes 6-9 are brain homogenates from mice IC inoculated with saliva from deer #133. Lanes 10-13 are brain homogenates from mice IC inoculated with saliva from deer #144. Lanes 14-17 are brain homogenates from mice IC inoculated with saliva from deer #123 a mock infected CWD(-) deer.
(TIF)

Figure S2. Brain section western blot analysis of deer tested preclinically for prions in saliva. A. PrP^{Res} western blot analysis of deer with 100% of PTA RT-QuIC positive replicates. B. Western blot PrP^{Res} analysis of deer with less than 100% of PTA RT-QuIC positive replicates. PK was added to all samples except one CWD(-) brain sample. Antibody BAR-224 was used for detection. Layout of western blots is the same as in figure 6.
(TIF)

Table S1. Summary of RT-QuIC results. Comparison of RT-QuIC results from dilution or PTA experiments performed in laboratories at CSU and RML.
(DOCX)

Acknowledgements

We thank Jeanette Hayes-Klug and Kelly Anderson for their excellent observation, care, and sample collection from deer.

Author Contributions

Conceived and designed the experiments: DMH MM EAH BC NJH. Performed the experiments: DMH MM NJH ND AVN. Analyzed the data: DMH MM NJH ND AVN. Contributed reagents/materials/analysis tools: CKM EAH BC. Wrote the manuscript: DMH EAH.

References

1. Williams ES, Young S (1980) Chronic wasting disease of captive mule deer: a spongiform encephalopathy. J Wildl Dis 16: 89-98. PubMed: 7373730.
2. Williams ES, Young S (1982) Spongiform encephalopathy of Rocky Mountain elk. J Wildl Dis 18: 465-471. PubMed: 7154220.
3. Mathiason CK, Nalls AV, Seelig DM, Kraft SL, Carnes K et al. (2013) Susceptibility of domestic cats to chronic wasting disease. J Virol, 87: 1947–56. PubMed: 23236066.
4. Heisey DM, Mickelsen NA, Schneider JR, Johnson CJ, Johnson CJ et al. (2010) Chronic wasting disease (CWD) susceptibility of several North American rodents that are sympatric with cervid CWD epidemics. J Virol 84: 210-215. doi:10.1128/JVI.00560-09. PubMed: 19828611.
5. Sigurdson CJ, Mathiason CK, Perrott MR, Eliason GA, Spraker TR et al. (2008) Experimental chronic wasting disease (CWD) in the ferret. J Comp Pathol 138: 189-196. doi:10.1016/j.jcpa.2008.01.004. PubMed: 18387626.
6. Raymond GJ, Raymond LD, Meade-White KD, Hughson AG, Favara C et al. (2007) Transmission and adaptation of chronic wasting disease to hamsters and transgenic mice: evidence for strains. J Virol 81: 4305-4314. doi:10.1128/JVI.02474-06. PubMed: 17287284.
7. Kurt TD, Seelig DM, Schneider JR, Johnson CJ, Telling GC et al. (2011) Alteration of the chronic wasting disease species barrier by in vitro prion amplification. J Virol 85: 8528-8537. doi:10.1128/JVI.00809-11. PubMed: 21697475.
8. Marsh RF, Kincaid AE, Bessen RA, Bartz JC (2005) Interspecies transmission of chronic wasting disease prions to squirrel monkeys (Saimiri sciureus). J Virol 79: 13794-13796. doi:10.1128/JVI.79.21.13794-13796.2005. PubMed: 16227298.
9. Perrott MR, Sigurdson CJ, Mason GL, Hoover EA (2012) Evidence for distinct chronic wasting disease (CWD) strains in experimental CWD in ferrets. J Gen Virol 93: 212-221. doi:10.1099/vir.0.035006-0. PubMed: 21918005.
10. Okada H, Murayama Y, Shimozaki N, Yoshioka M, Masujin K et al. (2012) Prion in saliva of bovine spongiform encephalopathy-infected cattle. Emerg Infect Dis 18: 2091-2092. doi:10.3201/1812.120528. PubMed: 23171518.
11. Orrù CD, Hughson AG, Race B, Raymond GJ, Caughey B (2012) Time course of prion seeding activity in cerebrospinal fluid of scrapie-infected hamsters after intratongue and intracerebral inoculations. J Clin Microbiol, 50: 1464-1466. PubMed: 22203750.
12. Orrú CD, Wilham JM, Raymond LD, Kuhn F, Schroeder B et al. (2011) Prion disease blood test using immunoprecipitation and improved quaking-induced conversion. mBio 2: e00078-00011. PubMed: 21558432.
13. Tamgüney G, Richt JA, Hamir AN, Greenlee JJ, Miller MW et al. (2012) Salivary prions in sheep and deer. Prion 6: 52-61. doi:10.4161/pri.6.1.16984. PubMed: 22453179.
14. Prusiner SB, Groth DF, Bolton DC, Kent SB, Hood LE (1984) Purification and structural studies of a major scrapie prion protein. Cell 38: 127-134. doi:10.1016/0092-8674(84)90533-6. PubMed: 6432339.
15. Gabizon R, Telling G, Meiner Z, Halimi M, Kahana I et al. (1996) Insoluble wild-type and protease-resistant mutant prion protein in brains of patients with inherited prion disease. Nat Med 2: 59-64. doi:10.1038/nm0196-59. PubMed: 8564843.
16. Telling GC, Parchi P, DeArmond SJ, Cortelli P, Montagna P et al. (1996) Evidence for the conformation of the pathologic isoform of the prion protein enciphering and propagating prion diversity. Science 274: 2079-2082. doi:10.1126/science.274.5295.2079. PubMed: 8953038.
17. Liao YC, Lebo RV, Clawson GA, Smuckler EA (1986) Human prion protein cDNA: molecular cloning, chromosomal mapping, and biological implications. Science 233: 364-367. doi:10.1126/science.3014653. PubMed: 3014653.
18. Bendheim PE, Brown HR, Rudelli RD, Scala LJ, Goller NL et al. (1992) Nearly ubiquitous tissue distribution of the scrapie agent precursor protein. Neurology 42: 149-156. doi:10.1212/WNL.42.1.149. PubMed: 1346470.
19. Riek R, Hornemann S, Wider G, Billeter M (1996) NMR Structure of the Mouse prion protein domain PrP (121-231). Nature 382: 180-182. doi:10.1038/382180a0. PubMed: 8700211.
20. Bamborough P, Wille H, Telling GC, Yehiely F, Prusiner SB et al. (1996) Prion protein structure and scrapie replication: theoretical, spectroscopic, and genetic investigations. Cold Spring Harb Symp Quant Biol 61: 495-509. doi:10.1101/SQB.1996.061.01.050. PubMed: 9246476.
21. Harper JD, Lansbury PT Jr. (1997) Models of amyloid seeding in Alzheimer's disease and scrapie: mechanistic truths and physiological consequences of the time-dependent solubility of amyloid proteins. Annu Rev Biochem 66: 385-407. doi:10.1146/annurev.biochem.66.1.385. PubMed: 9242912.
22. Collinge J, Clarke AR (2007) A general model of prion strains and their pathogenicity. Science 318: 930-936. doi:10.1126/science.1138718. PubMed: 17991853.
23. Caughey BW, Dong A, Bhat KS, Ernst D, Hayes SF et al. (1991) Secondary structure analysis of the scrapie-associated protein PrP 27-30 in water by infrared spectroscopy. Biochemistry 30: 7672-7680.
24. Thackray AM, Hopkins L, Bujdoso R (2007) Proteinase K-sensitive disease-associated ovine prion protein revealed by conformation-dependent immunoassay. Biochem J 401: 475-483. doi:10.1042/BJ20061264. PubMed: 17018021.

25. Mathiason CK, Powers JG, Dahmes SJ, Osborn DA, Miller KV et al. (2006) Infectious prions in the saliva and blood of deer with chronic wasting disease. Science 314: 133-136. doi:10.1126/science.1132661. PubMed: 17023660.
26. Haley NJ, Seelig DM, Zabel MD, Telling GC, Hoover EA (2009) Detection of CWD prions in urine and saliva of deer by transgenic mouse bioassay. PLOS ONE 4: e4848. doi:10.1371/journal.pone.0004848. PubMed: 19293928.
27. Mathiason CK, Hays SA, Powers J, Hayes-Klug J, Langenberg J et al. (2009) Infectious prions in pre-clinical deer and transmission of chronic wasting disease solely by environmental exposure. PLOS ONE 4: e5916. doi:10.1371/journal.pone.0005916. PubMed: 19529769.
28. Castilla J, Saá P, Hetz C, Soto C (2005) In vitro generation of infectious scrapie prions. Cell 121: 195-206. doi:10.1016/j.cell.2005.02.011. PubMed: 15851027.
29. Castilla J, Saá P, Soto C (2005) Detection of prions in blood. Nat Med 11: 982-985. PubMed: 16127436.
30. Saá P, Castilla J, Soto C (2006) Ultra-efficient replication of infectious prions by automated protein misfolding cyclic amplification. J Biol Chem 281: 35245-35252. doi:10.1074/jbc.M603964200. PubMed: 16982620.
31. Saborio GP, Permanne B, Soto C (2001) Sensitive detection of pathological prion protein by cyclic amplification of protein misfolding. Nature 411: 810-813. doi:10.1038/35081095. PubMed: 11459061.
32. Maddison BC, Rees HC, Baker CA, Taema M, Bellworthy SJ et al. (2010) Prions are secreted into the oral cavity in sheep with preclinical scrapie. J Infect Dis 201: 1672-1676. doi:10.1086/652457. PubMed: 20402590.
33. Atarashi R, Sano K, Satoh K, Nishida N (2011) Real-time quaking-induced conversion: a highly sensitive assay for prion detection. Prion 5: 150-153. doi:10.4161/pri.5.3.16893. PubMed: 21778820.
34. Wilham JM, Orrú CD, Bessen RA, Atarashi R, Sano K et al. (2010) Rapid end-point quantitation of prion seeding activity with sensitivity comparable to bioassays. PLOS Pathog 6: e1001217. PubMed: 21152012.
35. McGuire LI, Peden AH, Orrú CD, Wilham JM, Appleford NE et al. (2012) Real time quaking-induced conversion analysis of cerebrospinal fluid in sporadic Creutzfeldt-Jakob disease. Ann Neurol 72: 278-285. doi:10.1002/ana.23589. PubMed: 22926858.
36. Peden AH, McGuire LI, Appleford NEJ, Mallinson G, Wilham JM et al. (2011) Sensitive and specific detection of sporadic Creutzfeldt–Jakob disease brain prion protein using real-time quaking induced conversion. J Gen Virol 93: 438-449.
37. Browning SR, Mason GL, Seward T, Green M, Eliason GA et al. (2004) Transmission of prions from mule deer and elk with chronic wasting disease to transgenic mice expressing cervid PrP. J Virol 78: 13345-13350. doi:10.1128/JVI.78.23.13345-13350.2004. PubMed: 15542685.
38. Siqueira WL, Salih E, Wan DL, Helmerhorst EJ, Oppenheim FG (2008) Proteome of human minor salivary gland secretion. J Dent Res 87: 445-450. doi:10.1177/154405910808700508. PubMed: 18434574.
39. Sun X, Salih E, Oppenheim FG, Helmerhorst EJ (2009) Kinetics of histatin proteolysis in whole saliva and the effect on bioactive domains with metal-binding, antifungal, and wound-healing properties. FASEB J 23: 2691-2701. doi:10.1096/fj.09-131045. PubMed: 19339663.
40. Helmerhorst EJ, Traboulsi G, Salih E, Oppenheim FG (2010) Mass spectrometric identification of key proteolytic cleavage sites in statherin affecting mineral homeostasis and bacterial binding domains. J Proteome Res 9: 5413-5421. doi:10.1021/pr100653r. PubMed: 20731414.
41. Colby DW, Zhang Q, Wang S, Groth D, Legname G et al. (2007) Prion detection by an amyloid seeding assay. Proc Natl Acad Sci U S A 104: 20914-20919. doi:10.1073/pnas.0710152105. PubMed: 18096717.
42. Tamgüney G, Miller MW, Wolfe LL, Sirochman TM, Glidden DV et al. (2009) Asymptomatic deer excrete infectious prions in faeces. Nature 461: 529-532. doi:10.1038/nature08289. PubMed: 19741608.
43. Spraker TR, Miller MW, Williams ES, Getzy DM, Adrian WJ et al. (1997) Spongiform encephalopathy in free-ranging mule deer (Odocoileus hemionus), white-tailed deer (Odocoileus virginianus) and Rocky Mountain elk (Cervus elaphus nelsoni) in northcentral Colorado. J Wildl Dis 33: 1-6. PubMed: 9027685.
44. Silveira JR, Raymond GJ, Hughson AG, Race RE, Sim VL et al. (2005) The most infectious prion protein particles. Nature 437: 257-261. PubMed: 16148934.
45. Pastrana MA, Sajnani G, Onisko B, Castilla J, Morales R et al. (2006) Isolation and characterization of a proteinase K-sensitive PrPSc fraction. Biochemistry 45: 15710-15717. doi:10.1021/bi0615442. PubMed: 17176093.
46. McKinley MP, Bolton DC, Prusiner SB (1983) A protease-resistant protein is a structural component of the scrapie prion. Cell 35: 57-62. doi:10.1016/0092-8674(83)90207-6. PubMed: 6414721.
47. D'Castro L, Wenborn A, Gros N, Joiner S, Cronier S et al. (2010) Isolation of proteinase K-sensitive prions using pronase E and phosphotungstic acid. PLOS ONE 5: e15679. doi:10.1371/journal.pone.0015679. PubMed: 21187933.
48. Colby DW, Wain R, Baskakov IV, Legname G, Palmer CG et al. (2010) Protease-sensitive synthetic prions. PLOS Pathog 6: e1000736. PubMed: 20107515.
49. Gough KC, Baker CA, Rees HC, Terry LA, Spiropoulos J et al. (2012) The oral secretion of infectious scrapie prions occurs in preclinical sheep with a range of PRNP genotypes. J Virol 86: 566-571. doi:10.1128/JVI.05579-11. PubMed: 22013047.
50. Gonzalez-Romero D, Barria MA, Leon P, Morales R, Soto C (2008) Detection of infectious prions in urine. FEBS Lett 582: 3161-3166. doi:10.1016/j.febslet.2008.08.003. PubMed: 18706416.
51. Atarashi R, Satoh K, Sano K, Fuse T, Yamaguchi N et al. (2011) Ultrasensitive human prion detection in cerebrospinal fluid by real-time quaking-induced conversion. Nat Med 17: 175-178. doi:10.1038/nm.2294. PubMed: 21278748.

Animal Number	CSU Diluted Saliva	CSU PTA Saliva	RML Diluted Saliva	RML PTA Saliva
108	0/8	0/8	0/4	0/8
112	1/8	4/8	0/4	8/8
121	2/8	0/8	N.T.	8/8
132	0/8	1/8	N.T.	8/8
133	5/8	8/8	N.T.	8/8
136	0/8	2/8	1/4	6/8
137	0/8	N.T.	N.T.	4/8
138	3/8	5/8	4/4	10/12
143	0/8	N.T.	0/4	1/8
144	3/8	8/8	N.T.	8/8
773	0/8	0/8	0/4	3/8
775	1/8	1/8	0/4	0/8
776	0/8	7/8	0/4	8/8
777	1/8	0/8	0/4	2/12
778	1/8	5/8	0/4	12/12
780	0/8	3/8	0/4	1/8
781	0/8	0/8	0/4	0/8
785	1/8	3/8	0/4	12/12
812	1/8	1/8	0/4	0/8
813	0/8	1/8	0/4	16/16
815	1/8	3/8	0/4	8/8
816	3/8	N.T.	N.T.	0/8
817	1/8	N.T.	N.T.	6/8
818	1/8	N.T.	N.T.	2/8
810	0/8	0/8	N.T.	0/8
814	0/8	0/8	N.T.	0/8
819	0/8	0/8	N.T.	0/16
103	0/8	N.T.	N.T.	0/8
123	0/8	N.T.	N.T.	0/8
502	0/8	0/8	0/4	0/12
504	1/8	1/8	0/4	1/8

Table S1. Summary of RT-QuIC results. Comparison between dilution and PTA experiments performed in laboratories at CSU and RML, expressed in number of positive wells/total wells tested. N.T. is not tested.

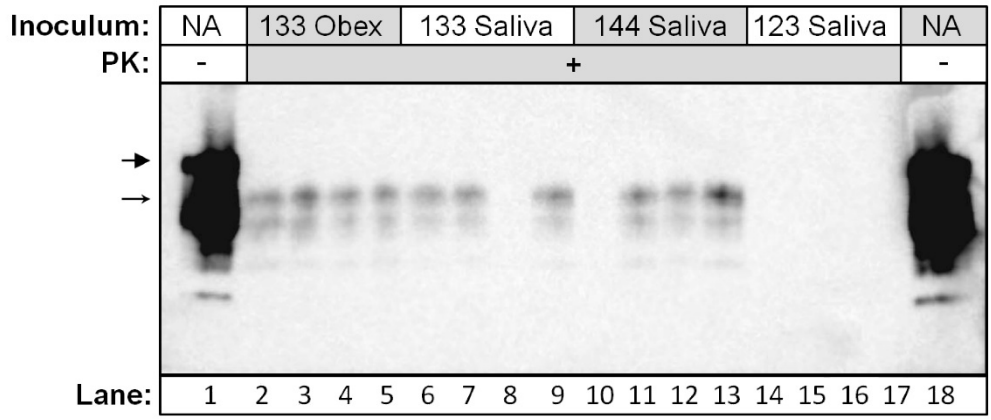

Figure S1. Western blot analysis of CWD(+) saliva inoculated Tg[CerPrP] 5037 mice. Lanes 1 and 18 show PrP^C form 10% mouse brain homogenates without PK digestion. Big arrowhead marks location of undigested PrP^C. Lanes 2-17 are PK digested brain homogenates from IC inoculated mice. Lanes 2-5 are brain homogenates from mice IC inoculated with obex from deer #133. Lanes 6-9 are brain homogenates from mice IC inoculated with saliva from deer #133. Lanes 10-13 are brain homogenates from mice IC inoculated with saliva from deer #144. Lanes 14-17 are brain homogenates from mice IC inoculated with saliva from deer #123 a mock infected CWD(-) deer.

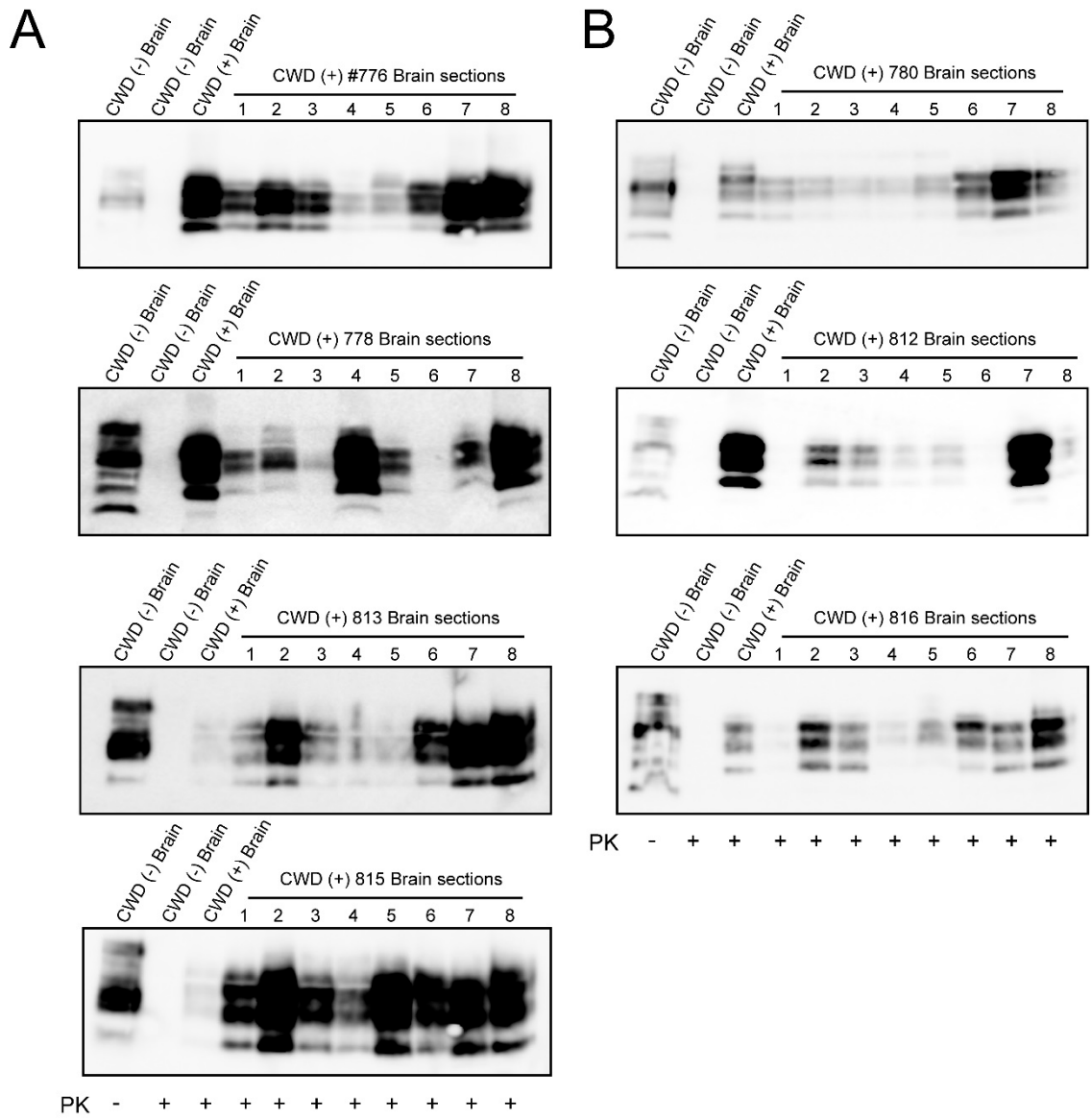

Figure S2. Brain section western blot analysis of deer tested preclinically for prions in saliva. A. PrP^{Res} western blot analysis of deer with 100% of PTA RT-QuIC positive replicates. B. Western blot PrP^{Res} analysis of deer with less than 100% of PTA RT-QuIC positive replicates. PK was added to all samples except one CWD(-) brain sample. Antibody BAR-224 was used for detection. Layout of western blots is the same as in figure 6.

References

(Alphabetical order)

Andreoletti O. et al. PrP^{Sc} accumulation in placentas of ewes exposed to natural Scrapie: influence of foetal PrP genotype and effect on ewe-to-lamb transmission. J Gen Virol (2002); 83:2607-2616.

Aguzzi A. and Polymenidou M. Mammalian prion biology: one century of evolving concepts. Cell (2004); 116:313-327.

Albrecht C. and Viturro E.P. The ABCA subfamily-gene and protein structures, functions and associated hereditary diseases. Pflugers Arch (2007); 453: 581-589.

Anonymous (2011) World Livestock Disease Atlas-A quantitative analysis of global animal health data (2006–2009). Co-publication by the World Bank and the TAFS forum (http://www.tafsforum.org/livestock-disease-atlas.html)

Atarashi R. et al. Ultrasensitive detection of Scrapie prion protein using seeded conversion of recombinant prion protein. Nat Methods (2007); 4:645-50.

Atarashi R. et al. Simplified ultrasensitive prion detection by recombinant PrP conversion with shaking. Nat Methods (2008); 5:211-2.

Atarashi R. et al. Ultrasensitive human prion detection in cerebrospinal fluid by real-time quaking-induced conversion. Nat Med (2011); 17:175-8.

Baeten L.A. et al. A natural case of chronic wasting disease in a free-ranging moose (Alces alces shirasi). J. Wildl. Dis. (2007); 43:309-314.

Brown P, Gajdusek C.D. Survival of Scrapie virus after three years interment. Lancet (1991); 337:269-270.

Caramelli M. et al. Evidence for the transmission of Scrapie to sheep and goats from a vaccine against Mycoplasma agalactiae. Vet Rec (2001); 28:531-536.

Chou T.C. et al. Generalized equations for the analysis of inhibitions of Michaelis-Menten and higher-order kinetic systems with two or more mutually exclusive and nonexclusive inhibitors. Eur. J. Biochem. (1981); 115:207-216.

Colby D.W. et al. Prion detection by an amyloid seeding assay. Proc Natl Acad Sci USA (2007); 104: 20914-20919.

Dessì S. and Batetta B. In: Cell growth and cholesterol esters; Pani and Dessì Eds. New York, NY, USA: Kluwer Academic/Plenum Publisher (2004a); pp 1-10.

Dessi S, Batetta B. In: Cell growth and cholesterol esters; Pani and Dessì Eds. New York, NY, USA: Kluwer Academic/Plenum Publisher (2004b); pp 25-33.

Detwiler L.A. and Baylis M. The epidemiology of Scrapie. Revue Scientifique et Technique Office International des Epizooties (2003); 22:121-143.

Di Ma et al. Searching for reliable premortem protein biomarkers for prion diseases: progress and challenges to date. Expert Rev. Proteomics (2012); 9(3), 267–280.

Dickinson A.G., Stamp J.T. Experimental Scrapie in Cheviot and Suffolk sheep. J Comp Pathol (1969); 79:23-26.

Diomede L. et al. The prion protein and cellular cholesterol homeostasis. Neurobiol Lipids (2002); 1:8-14.

Dubé C. et al. Retrospective investigation of chronic wasting disease of cervids at the Toronto Zoo, 1973-2003. Can. Vet. J. (2006); 47:1185-1193.

Ersdal C. et al. Mapping PrP^{Sc} propagation in experimental and natural Scrapie in sheep with different PrP genotypes. Vet Pathol (2005); 42:258-274.

Fink A.L. Chaperone-mediated protein folding. Physiol. Rev (1999); 79: 425-449.

Goldmann W. PrP genetics in ruminant transmissible spongiform encephalopathies. Vet Res (2008) 39:30.

Gorbenko G.P. and Kinnunen P.K.J. The role of lipid–protein interactions in amyloid-type protein fibril formation. Chemistry and Physics of Lipids (2006); 141(1-2):72-82.

Gough K.C. et al. The oral secretion of infectious Scrapie prions occurs in pre-clinical sheep with a range of PRNP genotypes. J Virol (2012); 86(1):566-71.

Haley N. J. et al. Detection of sub-clinical CWD infection in conventional test-negative deer long after oral exposure to urine and feces from CWD^{+} deer. PLoS ONE (2009); 4:e7990.

Hamir A.N. et al. Preliminary observations of genetic susceptibility of elk (Cervus elaphus nelsoni) to chronic wasting disease by experimental oral inoculation. J. Vet. Diagn. Invest. (2006); 18:110-114.

Haralambiev H. et al. An attempt to induce Scrapie in local sheep in Bulgaria. Zbl Vet Med B (1973); 20:701-709.

Henderson D. M. et al. Rapid antemortem detection of CWD prions in deer saliva. Plos One (2013); 8(9): e74377.

Hill A.F. et al. Diagnosis of new variant Creutzfeldt-Jakob disease by tonsil biopsy. Lancet (1997); 349: 99-100.

Hörnlimann B. et al. Portrait of Scrapie in sheep and goats (2007). In: Hörnlimann B, Riesner D, Kretzschmar H (eds) Prions in human and animals. Walter de Gruyter GmbH & CO KG, Berlin.

Hoinville L.J. A review of the epidemiology of Scrapie in sheep. Revue Scientifique et Technique Office International des Epizooties (1996); 15:827-852.

Houston F. et al. Prion diseases are efficiently transmitted by blood transfusion in sheep. Blood (2008) 112:4739-4745.

Hunter N. PrP genetics in sheep and the implications for Scrapie and BSE. Trends Microbiol (1997); 5:331-334.

Jeffrey M. et al. Classical sheep transmissible spongiform encephalopathies: pathogenesis, pathological phenotypes and clinical disease. Neuropath Appl Neurobiol (2007); 33:373-394.

Jewell J.E. et al. Low frequency of PrP genotype 225SF among free-ranging mule deer (Odocoileus hemionus) with chronic wasting disease. J. Gen. Virol. (2005); 86:2127-2134.

Johnson C. et al. Prion protein polymorphisms in white-tailed deer influence susceptibility to chronic wasting disease. J. Gen. Virol. (2006); 87:2109-2114.

Johnson C.J. et al. Prions adhere to soil minerals and remain infectious. PLoS Pathog (2006); 2:e32.

Kahn S. et al. Chronic wasting disease in Canada: Part 1. Can. Vet. J. (2004); 45:397-404.

Kim T.Y. et al. Additional cases of chronic wasting disease in imported deer in Korea. J. Vet. Med. Sci. (2005); 67:753-759.

Konold T. et al. Evidence of Scrapie transmission via milk. BMC Vet Res (2008); 4:14.

Kratzel C. et al. Propagation of Scrapie in peripheral nerves after footpad infection in normal and neurotoxin exposed hamsters. Vet Res (2007); 38:127-139.

Kurzchalia T.V. at al. Membrane microdomains and caveolae. Curr. Op. Cell Biol. (1999); 11:424-431

Lacroux C. et al. Dynamics and genetics of PrP^{Sc} placental accumulation in sheep. J Gen Virol (2007); 88:1056-1061.

Lacroux C. et al. Prions in milk from ewes incubating natural Scrapie. PLoS Pathog (2008); 4:e1000238.

Legname, G. et al. Synthetic mammalian prions. Science (2004); 305:673-676.

Leopoldt J.G. Nützliche und auf die Erfahrung gegründete Einleitung zu der Land-Wirthschafft. (1750) Volume 5, Johann Gottlieb Rothen, Sorau.

London E. Insights into lipid raft structure and formation from experiments in model membranes. Curr Opin Struc Biol (2002); 12:480-486.

Lühken G. et al. Epidemiological and genetical differences between classical and atypical Scrapie cases. Vet Res (2007)38:65-80.

Matthews D. et al. Bovine spongiform encephalopathy. In: OIE International Committee (ed) Manual of Diagnostic Tests and Vaccines for Terrestrial Animals (mammals, birds and bees), vol 2. World Organisation for Animal Health, OIE (2008); 671-682; 1048-1057.

Maxfield FR, Tabas I. Role of cholesterol and lipid organization in disease. Nature (2005); 438:36-45.

McIntyre K.M. et al. Epidemiological characteristics of classical Scrapie outbreaks in 30 sheep flocks in the United Kingdom. PLoS One (2008); 3:e3994.

Maddison B.C. et al. Prions are secreted in milk from clinically normal Scrapie-exposed sheep. J Virol (2009); 83:8293-8296.

Maddison B.C. et al. Prions are secreted into the oral cavity in sheep with preclinical Scrapie. J Infect Dis (2010); 201:1672-1676.

Mathiason C. K. et al. Infectious prions in the saliva and blood of deer with chronic wasting disease. Science (2006); 314:133-136.

Mawhinney S. et al. Human prion disease and relative risk associated with chronic wasting disease. Emerging Infect. Dis. (2006); 12:1527-1535.

Miller M.W. and Williams E.S. Prion disease: horizontal prion transmission in mule deer. Nature (2003); 425:35-36.

Nguyen J. et al. Prion protein peptides induce alpha-helix to beta-sheet conformational transitions. Biochemistry (1995); 34:4186-4192.

Novakofski J. et al. Prion biology relevant to bovine spongiform encephalopathy. J Anim Sci (2005); 83:1455-1476.

Onodera T. et al. Isolation of Scrapie agent from the placenta of sheep with natural Scrapie in Japan. Microbiol Immunol (1993); 37:311–316.

O'Rourke K.I. et al. PrP genotypes of captive and free-ranging Rocky Mountain elk (Cervus elaphus nelsoni) with chronic wasting disease. J. Gen. Virol. (1999); 80:2765-2769.

O'Rourke K.I. et al. Polymorphisms in the prion precursor functional gene but not the pseudogene are associated with susceptibility to chronic wasting disease in white-tailed deer. J. Gen. Virol. (2004); 85:1339-1346.

O'Rourke K.I. et al. Elk with a long incubation prion disease phenotype have a unique PrPd profile. Neuroreport (2007); 18:1935-1938.

Orrú C.D. et al. Prion disease blood test using immunoprecipitation and improved quaking-induced conversion. MBio (2011); 2:78-11.

Orrù et al. A test for Creutzfeldt-Jakob Disease using nasal brushings. Accepted by N Engl J Med (2014).

Pani A. et al. Accumulation of cholesterol esters in ex vivo lymphocytes from Scrapie-susceptible sheep and in Scrapie-infected mouse neuroblastoma cell lines. American J. of Inf Diseases (2007 a); 3(3): 165-168.

Pani A. et al. Antiprion activity of cholesterol esterification modulators: a comparative study using ex vivo sheep fibroblasts and lymphocytes and mouse neuroblastoma cell lines. Antimicrob Agents Chemother (2007 b); 4141-4147.

Pani A. et al. Cholesterol, Alzheimer disease, prion disorders: a ménage a trois? Curr Drug Targets (2010); 11:1018-31.

Parry H.B. Scrapie disease in sheep. Academic, London (1983).

Pattison I.H. et al. Spread of Scrapie to sheep and goats by oral dosing with foetal membranes from Scrapie-affected sheep. Vet Rec (1972); 90:465-468.

Pivetta T. et al. Synthesis, structural characterization, formation constants and in vitro cytotoxicity of phenanthroline and imidazolidine-2-thione copper(II) complexes. J. Inorg. Biochem. (2011); 105:329-338.

Prusiner S.B. Novel proteinaceous infectious particles cause Scrapie. Science (1982); 216:136-144.

Prusiner S.B. Prions. Proc. Natl. Acad. Sci. USA (1998); 95:13363-13383.

Prusiner S.B. 2004. Prion Biology and Diseases (book).

Prusiner S.B. Biology and genetics of prions causing neurodegeneration. Annu. Rev. Genet. (2013); 47:601-23.

Race R. et al. Scrapie infectivity and proteinase K-resistant prion protein in sheep placenta, brain, spleen, and lymph node: implications for transmission and antemortem diagnosis. J Infect Dis (1998); 178:949-953.

Riesner D. Biochemistry and structure of PrP^{C} and PrP^{Sc}. Br. Med. Bull (2003); 66:21-33.

Ryder S. et al. Demonstration of lateral transmission of Scrapie between sheep kept under natural conditions using lymphoid tissue biopsy. Res Vet Sci (2004); 76:211-217.

Saá P. et. al. Ultra-efficient replication of infectious prions by automated protein misfolding cyclic amplification. J Biol Chem (2006); 281:35245-52.

Sano K. et al. Early detection of abnormal prion protein in genetic human prion diseases now possible using Real-Time QuIC Assay. Plos One (2013); 8(1):e54915.

Schneider K. et al. The early history of the transmissible spongiform encephalopathies exemplified by Scrapie. Brain Res Bull (2008); 77:343-355.

Sigurdson C.J. et al. Oral transmission and early lymphoid tropism of chronic wasting disease PrP^{res} in mule deer fawns (Odocoileus hemionus). J Gen Virol (1999); 80: 2757-64.

Sigurdson C.J. A prion disease of cervids: chronic wasting disease. Vet. Res. (2008); 39:41

Seidel B. et al. Scrapie agent (Strain 263 K) can transmit disease via the oral route after persistence in soil over years. PLoS One (2007); 2(5):e435.

Simons K. et al. Cholesterol, lipid raft and disease. J. Clin. Invest. (2002); 110:597-603.

Stamp J.T. et al. Further studies on Scrapie. J Comp Pathol (1959); 69:268-280.

Tamguney G. et al. Asymptomatic deer excrete infectious prions in faeces. Nature (2009); 461:529-532.

Taylor D.M. et al. Scrapie infection can be established readily through skin scarification in immunocompetent but not immunode ficient mice. J Gen Virol (1996); 77:1595-1599.

Telling G.C. et al. Evidence for the conformation of the pathologic isoform of the prion protein enciphering and propagating prion diversity. Science (1996); 274:2079-2082.

Terry L.A. et al. Detection of prions in the faeces of sheep naturally infected with classical Scrapie. Vet Res (2011); 42:65.

Ulvund M. Clinical fi ndings in Scrapie (2007). In: Hörnlimann B, Riesner D, Kretzschmar H (eds) Prions in human and animals. Walter de Gruyter GmbH & CO KG, Berlin.

Van Keulen L. J. et al. TSE pathogenesis in cattle and sheep. Vet Res (2008); 39:24.

Wang P. et al. OSBP is a cholesterol-regulated scaffolding protein in control of ERK 1/2 activation. Science (2005); 307:1472-1476.

Williams E.S. and Young S. Chronic wasting disease of captive mule deer: a spongiform encephalopathy. J. Wildl. Dis. (1980); 16:89-98.

Williams E.S. and Young S. Spongiform encephalopathy of Rocky Mountain elk. J. Wildl. Dis. (1982); 18:465-471.

Williams E.S. Chronic wasting disease. Vet. Pathol. (2005); 42:530-549.

Wineland N.E. et al. Epidemiologic analysis of reported Scrapie in sheep in the United States: 1,117 cases (1947-1992). J Am Vet Med Assoc (1998); 212:713-718.

Wolfe L.L. et al. PrP^{CWD} in rectal lymphoid tissue of deer (Odocoileus spp.). J. Gen. Virol. (2007); 88:2078-2082.

Zanusso et al. Detection of pathologic prion protein in the olfactory epithelium in sporadic Creutzfeldt-Jakob Disease. N Engl J Med (2003); 348(8):711-9.

Acknowledgments

I would like to gratefully acknowledge Sardinia Regional Government for the financial support of my Ph.D. scholarship (P.O.R. Sardegna F.S.E. Operational Programme of the Autonomous Region of Sardinia, European Social Fund 2007-2013 – Axis IV Human Resources, Objective l.3, Line of Activity l.3.1.).

Finally, I just wanted to say thanks to anybody who taught me something and will in the future.

"Fatti non foste a viver come bruti,
ma per seguir virtute e canoscenza"